Understanding and Controlling Angular Momentum Coupled Optical Waves in Chirally-Coupled-Core (CCC) Fibers

by

Xiuquan Ma

A dissertation submitted in partial fulfillment
of the requirements for the degree of
Doctor of Philosophy
(Electrical Engineering)
in The University of Michigan
2011

Doctoral Committee:

Professor Almantas Galvanauskas, Chair
Professor Peter D. Miller
Professor Theodore B. Norris
Professor Herbert G. Winful

Dedicated to my parents.

ACKNOWLEDGEMENTS

First of all, I have to thank my parents for bringing me into this world, giving me their genes, and raising me with love and care. I'll always do my best to keep you proud of me.

I want to thank my advisor Professor Almantas Galvanauskas. It is very lucky for me to have such a brilliant, knowledgeable, and passionate professor as my advisor. In fact, Professor Galvanauskas is more than a mentor to me. He was working very closely with me during the entire time of my PhD study in the group, and it really feels great to have someone who can always lead my way when I got stuck at work. Moreover, when I got depressed with my personal life, he kindly cared and supported me, and helped me get back on the right track. I am deeply and truly grateful.

I want to thank all my committee members to review and evaluate my dissertation and thesis defense. I really appreciate the time and effort all of you have spent on my PhD study and my graduation process. In addition, I would like to thank Professor Theodore Norris for teaching me EECS-537 and EECS-546, and Professor Herbert Winful for teaching me EECS-634. These lectures I took in Michigan Optics program are the best lectures I've ever taken. I would like to thank Professor Peter Miller from Applied Mathematics Department for reviewing my work as a mathematician. I would appreciate every bit of your suggestions to my work.

I would like to thank my colleagues and former colleagues for working with me. Also, I would like to thank all the staff members working at EE Department and at Optics Program. I wouldn't have achieved anything without your help.

I would like to thank all my friends in ann arbor. It is you guys who bring me comfort and happiness during all these years. I truly enjoyed my life here.

At last, I would like to wish all of you to have a lucky and happy life.

TABLE OF CONTENTS

LIST OF FIGURES

Figure

ABSTRACT

Understanding and Controlling Angular Momentum Coupled Optical Waves in Chirally-Coupled-Core(CCC) Fibers

by

Xiuquan Ma

Chair: Almantas Galvanauskas

In this dissertation a new type of fiber structure — so called Chirally-Coupled-Core (CCC) fiber — is extensively explored. Work presented here establishes theoretical, numerical and experimental foundations of describing optical phenomena in these novel structures, and provides with methods and tools required to design them. CCC fibers have been a very interesting topic of study due to their unusual symmetry (they are helically symmetric), novel nature of wave interactions within them, and the technological importance of their applications. We have discovered that operation of CCC fibers is based on optical wave interactions that involve both orbital and spin angular momentum of the propagating modes. This is the first and so far the only known example when optical angular momentum is involved in optical interactions.

In this thesis we first show experimental evidence of multitude of optical resonances that cannot be explained within the framework of conventional phase-matched interactions. Then we show that these observations can be explained through optical-angular momentum assisted optical interactions of optical waves in these structures.

Based on this approach we demonstrate a primary application of CCC structures: large core fibers that perform as effectively single mode fibers. Furthermore, we develop a rigorous theoretical model starting from Maxwell equations in curvilinear helical coordinates to describe CCC fiber properties. We show that theoretically predicted optical-resonance positions agree very well with experimental results. We also address the ultimate core-size scaling potential of effectively -single-mode CCC fibers. Due to the unusual nature of wave interactions in CCC structures all previously known numerical beam-propagation methods appear to be unsuitable for CCC structures. In order to provide with the numerical tools necessary to design and explore these fibers we have developed a new beam-propagation approach, which appears to provide with accurate predictions of CCC fiber performance.

CHAPTER I

Introduction to Chirally-Coupled-Core (CCC) Fibers

In this chapter, we will first briefly discuss the background of optical fiber technology and the importance of Chirally-Coupled-Core(CCC) fiber technology. We also describe basic geometry of CCC fibers. This section ends with the outline of the thesis structure.

Optical Fiber Technology

Optical fibers are critically important in a wide range of applications such as telecommunications (*Kao*, 2010), biomedical imaging and surgical procedures, frequency standard metrology (Hall , 2006), and variety of optical sensors for a wide range of applications, and currently are enabling revolutionary advances in new generation of scientific and industrial lasers. Optical fiber telecommunications has become one of the most important technologies in the modern society, which was recently been recognized by a Nobel Prize in Physics (2009) awarded to the inventor of optical fibers for telecommunications. Optical fibers are widely used in biomedical imaging and surgical procedures. Special type of optical fiber is also at the core of frequency-standard metrology, significance of which also was recognized by a Nobel Prize in 2005. Optical sensors based on optical fibers are becoming ubiquitous in various structural-mechanical, aerospace, environmental and chemical applications. Furthermore, optical fiber initiated a true revolution in laser technology due to their excellent compactness, ruggedness, high efficiency and superior thermal properties. Recently fiber lasers produced remarkably high optical powers with pure, diffraction-limited beam quality, becoming highest-power lasers currently available. As such fiber lasers are becoming the next generation technology in majority of industrial and scientific applications.

The key advantage of optical fibers, as well as the main reason for being so broadly used, is due to the paraxial wave guidance, which produces practically lossless light propagation for long distances while maintaining a fixed and well-defined wavefront. Up to now, fiber modal properties have only been controlled by tailoring the confinement of such guided waves. There are two methods of achieving paraxial wave guidance: total internal reflection and photonic-crystal bandgap (*Knight et al.*, 1998), and each of them contributed to distinct stages of the evolution of fiber technology, both in scientific and industrial applications. The first stage is associated with the

initial birth of modern standard telecommunication fibers and with a fiber amplifier, which exploits paraxial wave guidance based on the total internal reflection. The second stage was initiated by the invention of photonic crystal fibers, in which wave guidance is due to photonic-crystal bandgap. Here, we introduce Chirally-Coupled-Core(CCC) fiber structures, in which guided modes can interact with each other involving their optical angular momentum (*Allen et al.*, 2003). Thus, as we discovered, CCC fibers provide with fundamentally new degrees of freedom in controlling modal properties of optical light propagating in optical fibers.

Chirally-Coupled-Core(CCC) Fibers

We discovered the optical angular momentum coupled optical waves in CCC fibers. One major conclusion of this thesis is that, the eigenmodes that are propagating in the CCC fibers are the ones carrying spin and orbital optical angular momentum. Therefore, by controlling the modal interactions in CCC fibers, we can control the spin and orbital angular momentum of the optical waves propagating in the CCC fibers. This brings an entirely new degree of freedom in the optical fiber designs and applications, and enables the potential to explore and even manipulate the angular momentum of optical light, which would make profound impact to both the academic research and engineering applications.

One interesting example of controlling this novel modal property is the possibility of designing effective single-mode large-mode-area CCC fibers, which support multiple modes in large diameter cores but only allow the Gaussian-like fundamental mode to propagate. Thus, it overcomes one of the fundamental limitations of conventional fibers, and provides the large mode area and intrinsically good beam quality at the same time. This can be achieved because the fundamental mode has different modal profile and symmetric shape comparing with all the other higher order modes. This leads to a symmetry-based modal distinction between different modes allowing

the implementation of structures where all modes except the fundamental one are radiation modes and, therefore, do not propagate.

Another example is the possibility of tailoring spectral transmission to control the nonlinear interactions of high-intensity beams propagating in such fibers, which, depending on the conditions, could either enhance or prohibit some of the nonlinear interactions. Stimulated Raman Scattering(SRS) and Stimulated Brillouin Scattering(SBS) are two detrimental nonlinear effects that are limiting the power scaling of current kilo-watt high power fiber laser development. With CCC fibers, we have proposed and are currently working on the suppression of both nonlinear effects, which would make revolutionary progress in high power fiber lasers. Four-wave-mixing is another nonlinear effect in fused-silica fibers with rather useful applications such as the wavelength conversion inside the optical fibers. With CCC fibers, we also proposed the enhancement of such effect for such applications.

More applications of CCC fiber can be found regarding its unique functionality of controlling the optical angular momentum. It has been early recognized that electromagnetic optical waves can carry spin-angular momentum (circular polarization) (*Beth*, 1936). However, only recently, attention has been paid to optical orbital angular momentum (optical vortex) (*Allen et al.*, 1992). Since then it has found a number of interesting applications including particle trapping and manipulation (*Gahagan and Swartzlander, Jr.*, 1996; *Dienerowitz et al.*, 2008), quantum communication (*Gibson et al.*, 2004) and quantum computing and information encoding in multi-dimensional quantum space (*Molina-Terriza et al.*, 2007). Therefore, the possibility of generating and maintaining beams with stable and well-defined orbital-angular (as well as spin-angular) momentum with CCC fibers is very intriguing.

Geometrical Configuration of CCC Fibers

The cross section view of a fabricated CCC fiber sample is shown in Figure 1.1, and the three-dimensional geometry (not in scale) of CCC structure is shown in Figure 1.2. It consists of two wave-guiding cores deposited within one glass cladding, and the two cores are placed in optical proximity to each other, so that they form a weakly coupled waveguide system. The fabrication process of such structure is relatively straightforward: it requires a fiber perform with both cores running straight through it, central core being on axis and side-core off-axis. Spinning such a fiber preform during fiber draw process using conventional fiber-preform spinning techniques will then produce this CCC structure.

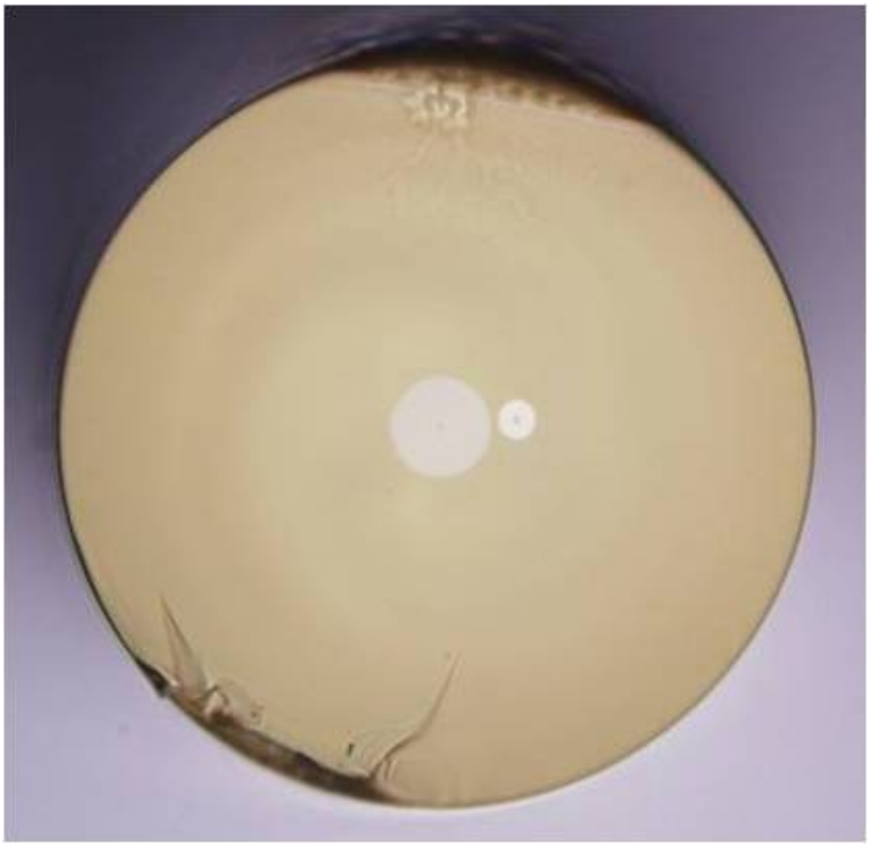

Figure 1.1: Cross-section view of CCC fiber sample with 250μm-diameter cladding, 35μm-diameter central core, 13μm-diameter side core, 0.06 central core NA, and 0.1 side core NA. The separation between central core and side core is 3μm, and the helix pitch of the side core is 6.1mm.

The core in the center of the cladding referred to as "central core" runs straight along the fiber axis, as in ordinary fibers. It is this core that serves for transmitting or amplifying the optical signal, just as in conventional fibers. The other core is referred to as "side core" and chirally winding around the central core following a helical path with a constant "helix pitch Λ" and "offset R_h". It is typically much smaller in diameter and its primary purpose is to control modal properties of the central core. This control is accomplished by engineering the desirable central-to-side core modal interactions which involve angular momentum carried by each mode, and all the interesting properties that can be obtained in a CCC fiber result from the unusual nature of this interaction.

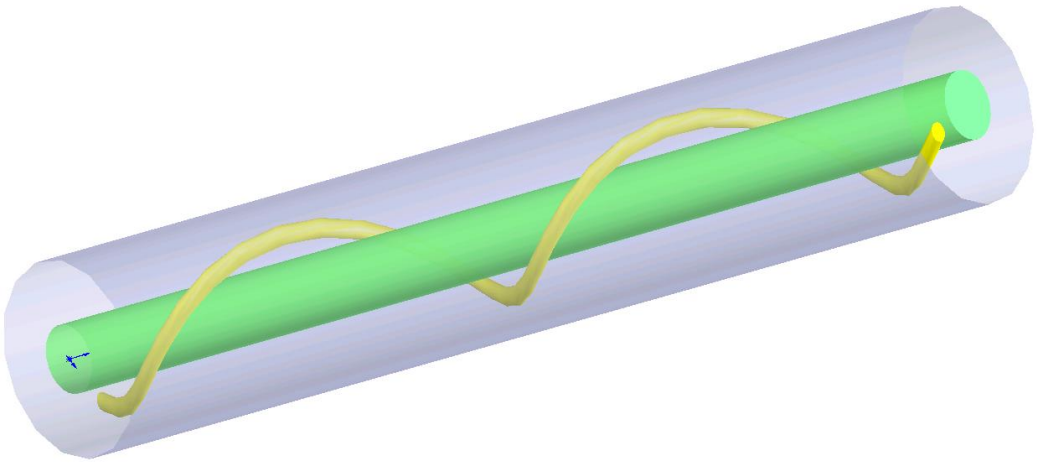

Figure 1.2: 3D geometry of CCC structure (not in scale).

Following Chapters in This Dissertation

In this dissertation, the CCC fiber is thoroughly explored on the following issues: 1. Experimental Characterization; 2. Physical Understanding; 3. Primary Application; 4. Theoretical Modeling; 5. Design Scalability; 6. Numerical Simulation; 7. Potential Application.

In Chapter II, Experimental Characterization, Physical Understanding, and Primary Application of CCC fibers are discussed in sequence. First, the experimental characterization of CCC reveals a physical observation that is beyond the explanation of current standard parallel waveguide theory. Then, we discover the angular momentum coupled optical waves in CCC fibers, which is the physical understanding of this novel phenomenon. Based on this physical understanding, we explore the current primary application: effective single-mode operation of large-mode-area CCC fibers.

In Chapter III, Theoretical Modeling is performed to provide rigorous mathematical analysis of CCC fibers. Compared with Physical Understanding discussed in Chapter II, this chapter goes through the rigorous mathematical derivation step by step. In the end, all the arguments in Physical Understanding would be verified by the mathematically derived analytical expressions.

In Chapter IV, Design Scalability is discussed to demonstrate the ability of scaling the core size for effective single-mode CCC fibers. This is one of the most important issues we needed to solve in this thesis.

In Chapter V, regarding Numerical Simulation, a new numerical model is described based on a new FD BPM algorithm that we had developed to describe optical wave propagation in CCC fibers.

In Chapter VI, Potential Application and the conclusion of the entire thesis work are presented.

CHAPTER II

Conceptual Understanding and Experimental Characterization of CCC Fibers

In the first half of this chapter, we start with showing the experimental observation of quasi-phase-matching (QPM) resonances in CCC fibers transmission spectrum. Then, we will analyze the conceptual understanding of this experimental phenomenon with physical argument and illustrations. After that, a simple analytical formula is presented to fit the experimental observations, though no mathematical proof is demonstrated here. The verification of the conceptual understanding and the simple analytical formula is also demonstrated based on an experimental measurement.

In the second half of this chapter, we will focus on the current primary application of CCC fibers: large-mode-area effective single-mode operations. First, we will present the solid evidence of effective single-mode operation with a 35μm-core-diameter large-mode-area CCC fiber sample. Then, a quantitative measurement technique which is capable of quantifying the ratio of higher order mode (HOM) over fundamental mode is demonstrated in details. The characterization with this technique shows that the HOM suppressions are more than 30dB/m, which means very good effective single-mode operation. In addition, we will also demonstrate the advantage of using large-mode-area effective single-mode CCC fibers for the high power fiber laser and laser amplifier.

2.1 Quasi-Phase-Matching (QPM) Resonances due to Angular Momentum Coupled Optical Waves

2.1.1 Experimentally Observed QPM Resonances

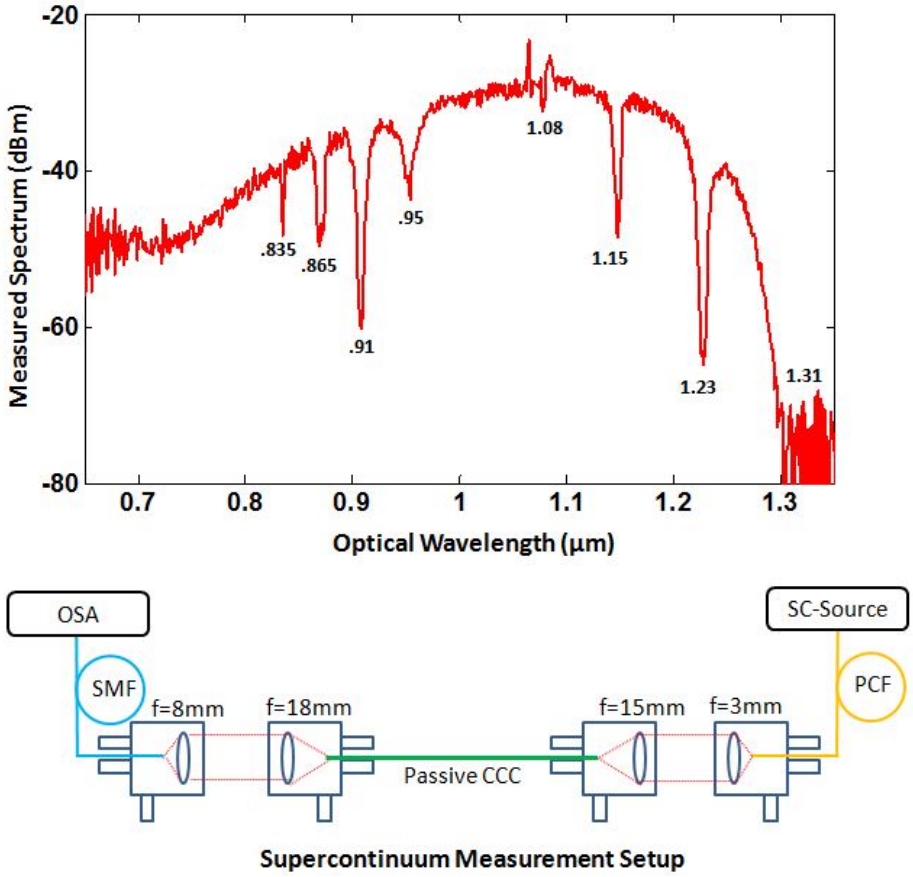

Figure 2.1: Experimentally observed transmission spectrum through CCC fiber central core. It is obtained by launching a broad-band supercontinuum broadband laser source into the 35μm-diameter central core of the 1.5meter-long CCC fiber sample.

In the experimental setup shown in Figure 2.1, the experimentally-measured transmission spectrum obtained by launching a supercontinuum broadband laser source into the central core of a CCC fiber sample. For consistency, this particular fiber sample is used throughout this entire dissertation for default. It is a 1.5meter-long passive CCC fiber with 35μm diameter and 0.06 numerical aperture (NA) central core, 13μm diameter and 0.1 NA side core, core to core separation 3μm, and helix pitch 6.1mm.

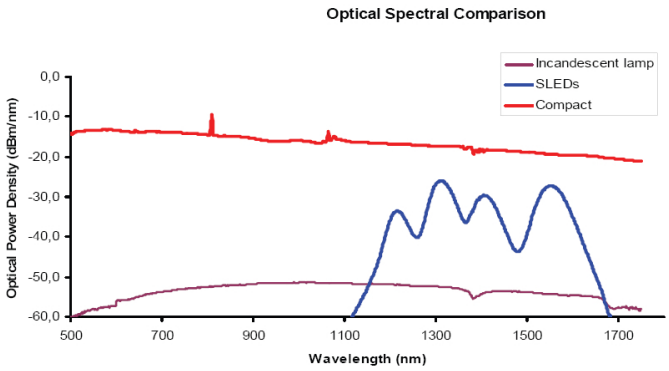

Figure 2.2: Spectrum of supercontinuum source coming out of Koheras "SuperK Compact" module. Comparing with lamp and super-luminance-LED (SLED), supercontinuum provides higher power spectrum density, and flat and stable output all across the spectrum from 500nm to 1750nm.

The cross-section view of this particular fiber sample is shown in Chapter I.

The supercontinuum source is a "SuperK Compact" model from Koheras. The supercontinuum is generated by launching a 2ns pulse duration, 24kHz reparation rate and 200-300 milli-Watts fiber amplifier amplified 1064nm pulsed diode laser signal into an index guiding photonic crystal fiber(PCF) which is nominal to be 10 meters with 4.8μm diameter and 0.2 NA (at 1064nm). The small-diameter and strongly-guiding core of this PCF fiber induces high nonlinearity and causes zero-dispersion-wavelength shifted to be shorter than and close to signal wavelength at 1064nm. Thus, we would have all kinds of nonlinearities in this fused silica medium. First, four-wave-mixing originates from both sides of 1064nm and generates spectrum in proximity to 1064nm. Second, modulation-instability(MI) rises from anomalous GVD due to the shifted zero-dispersion-wavelength, and then breaks up these nanosecond pulses into numerous shorter pulses in picosecond scale. Then, these short pulses would generate shorter wavelength spectrum through self-phase-modulation and self-steepening, and generate longer wavelength spectrum through stimulated Raman scattering and self soliton frequency shift. By controlling all kinds of fiber nonlinearity effect properly, Koheras "SuperK Compact" module has managed to generate about 100 milli-Watts

"flat and stable output spectrum from 500nm to 1750nm", according to their in-house characterization shown in Figure 2.2.

With mode-matching lens pair and nanometer-precision adjustment stage as shown in Figure 2.1, we can launch the single transverse mode of supercontinuum light into and only into the central core of this passive CCC fiber sample, and then receive the supercontinuum light coming out of the central core with a single mode fiber with cutoff wavelength around 800nm. The output of the single mode fiber is directly sent into optical spectrum analyzer.

Main observation here is the multiple transmission dips in certain wavelength positions. Since the supercontinuum spectrum is supposed to be flat across the entire spectrum range according to Figure 2.1, these transmission dips can only be interpreted as wavelength-dependent loss in the central core. Since the central core of the CCC fiber acts like a normal fiber core, there should be no significant loss other than negligible loss due to material scattering and absorption. Thus, the reason for those significant wavelength-dependent loss in the central core must come from its coupling with the lossy side core due to the curvature. Therefore, these wavelength positions imply modal coupling resonances with phase-matching conditions.

From the standard waveguide theory (*Yariv and Yeh*, 2003; *Huang*, 1994), we know that the modal coupling only happens at certain wavelength where the phase matching condition is fulfilled:

$$\Delta\beta(\lambda) = \beta_a(\lambda) - \beta_b(\lambda) = 0, \tag{2.1}$$

where $\beta_a(\lambda)$ and $\beta_b(\lambda)$ are the propagation constants for center core and side core respectively. It is important to point out that the side core propagation constant $\beta_b(\lambda)$ is the projection onto the axial direction, which have been lifted by the helical

correction factor $\sqrt{1+K^2R_h^2}$:

$$\beta_b(\lambda) \longrightarrow \beta_b(\lambda)\sqrt{1+K^2R_h^2}. \tag{2.2}$$

Thus, we have the wavelength-dependent center-core loss $\alpha_a(\lambda)$ as:

$$\alpha_a(\lambda)|_{\Delta\beta(\lambda)=0} \Longrightarrow \alpha_a[\kappa_{ab}(\lambda), \alpha_b(\lambda)] > 0. \tag{2.3}$$

This means that we need 2 necessary conditions to achieve significant central-core loss at certain wavelength λ_{ab}:

1. Phase-Matching Condition: $\Delta\beta(\lambda = \lambda_{ab}) = 0$;
2. Significant Side-Core Curvature Loss: $\alpha_b(\lambda = \lambda_{ab}) > 1$ dB/m.

In Figure 2.1, we can see that the resonance wavelength positions λ_{ab} show themselves as: 835nm, 865nm, 910nm, 950nm, 1080nm, 1150nm, 1230nm, and 1310nm.

Knowing the fiber parameters, we can calculate the side-core wavelength-dependent loss $\alpha_b(\lambda)$, and obtain the phase matching conditions by plotting the the dispersion curves $\beta_a(\lambda)$ and $\beta_a(\lambda)$, so we can examine if these wavelength positions fit the two conditions. For fibers with step-index profiles, it is quite easy to obtain $\alpha_b(\lambda)$, $\beta_a(\lambda)$ and $\beta_a(\lambda)$. To calculate the curvature loss $\alpha_b(\lambda)$ of step-index fiber, we can use the analytical formula derived by D. Marcuse (*Marcuse*, 1975). To calculate the dispersion curves $\beta_a(\lambda)$ and $\beta_a(\lambda)$, we can use the analytical formula derived by D. Gloge (*Gloge*, 1971). These analytical formula are accurate and fast for ideal step-index fibers, but the practically-made optical fibers are often non-step-index ones. The 2D and 1D index profile for this particular CCC fiber sample are shown in Figure 2.3, which shows the index profile of this fiber sample is far away step-index profile.

For the fibers with arbitrary index profiles, the analytical formula are not accurate anymore. It turns out that the numerical approach called Beam-Propagation-Method

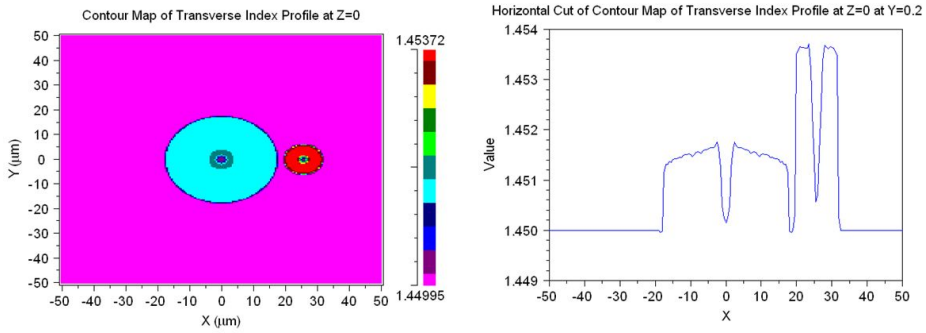

Figure 2.3: 2D and 1D arbitrary refractive index profile of the CCC fiber sample.

(BPM) algorithm can simulate the propagation of optical waves in optical fibers, and a BPM-based mode-solving technique called "correlation method" (*Feit and Fleck, Jr.*, 1980) is suitable to calculate the wavelength dependent loss $\alpha_b(\lambda)$ and dispersion curves $\beta_a(\lambda)$ and $\beta_b(\lambda)$ for any arbitrary index profiles.

The wavelength-dependent loss $\alpha_b(\lambda)$ for side-core LP_{11} mode and LP_{21} mode are shown in Figure 2.4a. The point **A**≈815nm and the point **B**≈1070nm are the wavelength positions where the significant side-core loss starts to appear for each mode. By comparing with the experimental transmission spectrum shown in Figure 2.4c, we can conclude that the lossy dips at 835nm, 865nm, 910nm, and 950nm are from side-core lossy mode LP_{21}, and the lossy dips at 1080nm, 1150nm, 1230nm, and 1310nm are from side-core lossy mode LP_{11}.

The wavelength-dependent dispersion curves for side-core LP_{11} mode and LP_{21} mode are shown in Figure 2.4b. Whereas, instead of propagation constants $\beta_a(\lambda)$ and $\beta_b(\lambda)$, we choose more convenient effective refractive index $n_{\text{eff},a}(\lambda) = \beta_a(\lambda)/k_0$ and $n_{\text{eff},b}(\lambda) = \beta_b(\lambda)/k_0$. The purple line represents the central-core LP_{01} modal dispersion, the blue and the red one represents the side-core LP_{21} and LP_{11} modal dispersion. We can see that the two crossing wavelength positions (810nm and 1230nm) are the only two phase-matching conditions in this wavelength range. Since 810nm corresponds to negligible side core loss, it is not expected to appear as a transmission dip. Therefore, we only expect to see one resonances: 1230nm.

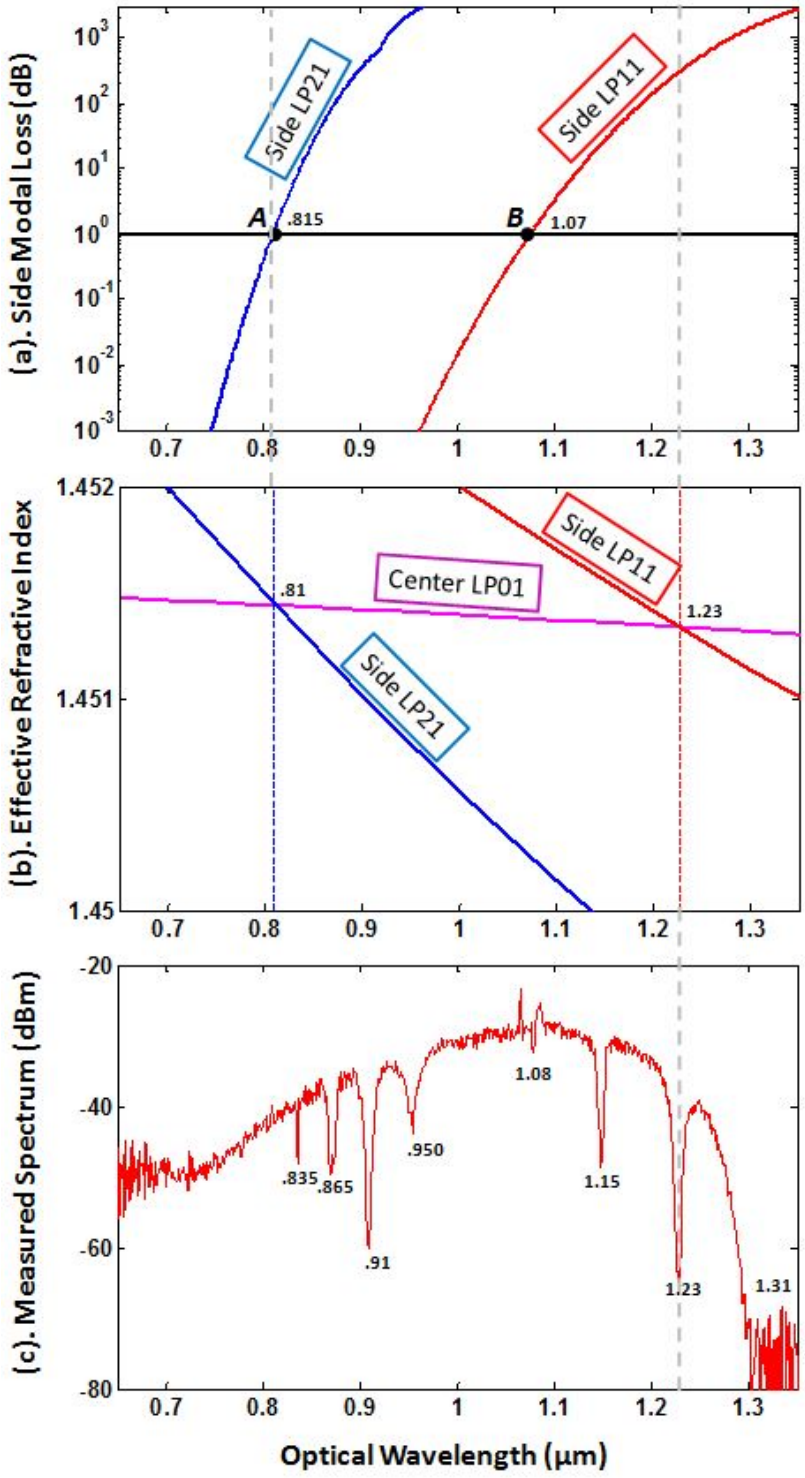

Figure 2.4: The side modal loss and phase-matching wavelength positions compared with supercontinuum transmission spectrum.

By comparing Figure 2.4b and 2.4c, we can see 1230nm is certainly there, but the experimental observation shows more phase matching conditions than we predicted based on the standard waveguide theory. It means that, regarding how to determine the phase-matching condition in CCC fibers, there must be something beyond the standard waveguide theory.

Here, the surprising fact is the phase matching condition occurs when the two modes are propagating at different phase velocities (phase velocity is equivalent to propagation constant). From the momentum conservation point of view, the linear translational momentum is not conserved. Therefore, we can call these extra resonances as "Quasi-Phase-Matching" (QPM) conditions.

By takeing a close look at the multiple resonances in transmission spectrum, we can see that the extra resonances are equally separated by a propagation constant difference $\Delta\beta = K$, which happens to be the rotation rate of the CCC helical structure. It simply means that the phase-mismatch $\Delta\beta$ is somehow compensated by the rotation of the CCC structure K. From the momentum conservation point of view, the linear translational momentum mismatch must be compensated by some other momentum associated with the rotation of the CCC structure. It turns out that the coupling between central core and side core in CCC fiber involves the angular momentum of optical waves and the eigenmodes of CCC fiber are the ones with orbital angular momentum $l\hbar$ and spin optical angular momentum $s\hbar$.

2.1.2 Conceptual Understanding of QPM Resonances

From the fact that the standard waveguide theory predicts less coupling resonances than the experimentally-observed ones in the CCC structure, we would know that something important is missing. Indeed, it is the most fundamental physical feature of the side core: the helical-translational symmetry.

The helical-translational symmetry in CCC fibers is a lower degree of symmetry

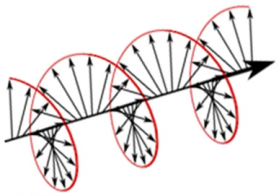

Figure 2.5: Picture of Spin Optical Angular Momentum: The vector direction of the modal field is rotating and propagating at the same time.

compared with the cylindrical symmetry in traditional cylindrically symmetric fibers. For the cylindrical symmetry of traditional fiber cores, we have independent rotational symmetry and linear translational symmetry. In other words, the left-handed helix and the right-handed helix are degenerate in cylindrical symmetry. But they are not degenerate anymore in helical symmetry, or to say the degeneracy is broken.

For the helical-translational symmetry, the rotational symmetry and linear translational symmetry are coupled: the symmetry would require the physical quantity to rotate (rotational symmetry) and propagate (linear translational symmetry) at the same time, just like a helix. Correspondingly, the eigenmodes carrying such symmetry would require its electromagnetic field (as a physical quantity) to do exactly the same: rotate and propagate at the same time. So this naturally leads to the conclusion that the eigenmodes of CCC structure with helical translational symmetry are the ones carrying spin and orbital angular momentum.

When the direction of modal field is rotating and propagating at the same time, we call it spin angular momentum (SAM), which is essentially the circular polarized light. The spin momentum that a photon could carry is $s\hbar$, and s could only be +1 or -1. It simply corresponds to right-handed and left-handed circular polarized light. It is mathematically described by an angular-dependent unit vector $\hat{\mathbf{e}}_\mathbf{s}$:

$$\hat{\mathbf{e}}_\mathbf{s} = \hat{\mathbf{e}}_\mathbf{x} + js\hat{\mathbf{e}}_\mathbf{y} = \hat{\mathbf{r}}e^{js\theta}, \tag{2.4}$$

where $\hat{\mathbf{r}}$ is the radius vector, and θ is the azimuthal angle in the transverse plane.

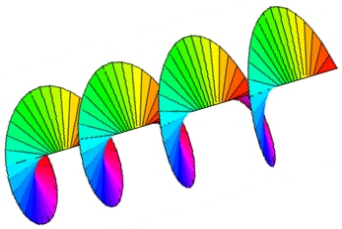

Figure 2.6: Picture of Orbital Optical Angular Momentum: The amplitude distribution of the modal field is rotating and propagating at the same time.

The demonstration of SAM is shown in Figure 2.5. It illustrates the physical picture of SAM: the direction vector of the electric field rotates and propagates at the same time. The evolution of the unit vector described in Eq.(2.4) can be simply obtained by multiplying an propagation phase term $e^{j\beta z}$, so we can have direction angle as a function of the propagation distance z:

$$\phi(z) \quad = \quad s\theta - \beta z. \tag{2.5}$$

Simply plotting this function, we can have the 3D plot in Figure 2.5.

When the scalar distribution of the modal field is rotating and propagating at the same time, we call it orbital angular momentum (OAM), which is also called as optical vortex. Unlike SAM, the quantum number OAM could be zero and any positive and negative integers, and it can be described as $e^{\pm jl\theta}$, where $l = 0, 1, 2....$

The demonstration of OAM is shown in Figure 2.6. It illustrates the physical picture of OAM: the phase front of the electric field rotates and propagates at the same time. Similarly, by multiplying a propagation phase term $e^{j\beta z}$, the phase evolution of the electric field carrying OAM become a function of propagation distance z:

$$\psi(z) \quad = \quad l\theta - \beta z. \tag{2.6}$$

By plotting this function, we can have the phase front evolution shown in Figure 2.6.

In Chapter III, a full mathematical derivation will be given to quantitatively

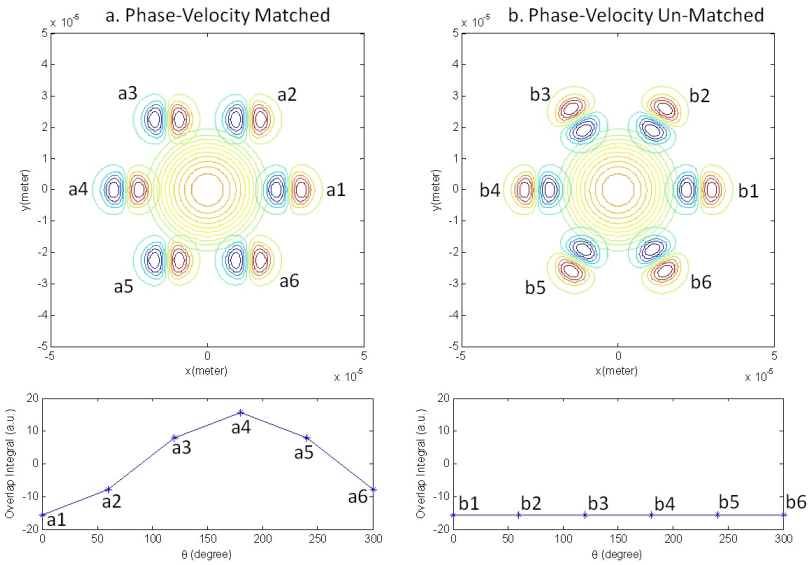

Figure 2.7: Intuitive and physical understanding of QPM.

explain the QPM conditions. Here, not with any mathematics but with a more intuitive and physical picture, we can use LP-modes carrying OAM to find out why the eigenmodes of CCC structure are the ones with optical angular momentum and how the QPM would happen. In order to do so, we take central core fundamental mode LP_{01} and side core LP_{11} mode for example. We can notice that there is a direct connection between the OAM quantum number l and the mode number $|l|$ of $LP_{|l|x}$ mode. Thus, the LP_{01} mode carries OAM with $l = 0$, and the mode LP_{11} carries OAM with $l = \pm 1$. By plotting their phase front evolution under two different scenarios in Figure 2.7, we can intuitively understand the relation between the QPM condition and optical angular momentum.

In Figure 2.7a, phase velocities are completely matched between central and side modes. It means we should see the same modal field phase front (scalar distribution) after every optical cycle. With exaggeration, we can consider the positions a1, a2, a3, a4, a5, and a6 are 6 sequential snapshots in time domain for 6 successive optical cycles. With identical phase velocity between central and side modes, the modal field distributions are exactly the same for each position, but the overlap integrals between

two modal field are varying:

$$\begin{aligned} I &= \int \left[R_a(x,y)\cdot e^{-j\beta_a z}\right]^* \cdot \left[R_b(x,y)\cdot \cos(Kz)\cdot e^{-j\beta_b z}\right] dxdy, \\ &= \int R_a(x,y)^* R_b(x,y)\cos(Kz)dxdy, \quad \text{When } \beta_a - \beta_b = 0, \end{aligned} \tag{2.7}$$

This indicates that, even though the phase velocity is identical, the relative phase difference between two modes is still changing with propagation due to the relative rotation between central and side core. By definition, we do not have actual phase matching under this scenario.

In Figure 2.7b, phase velocities are not matched between central and side modes. However, we can make the phase velocity difference $\beta_a - \beta_b$ right equal to angular rotation velocity of side core helix K. Similarly, we can plot the modal field at 6 sequential snapshots of positions b1, b2, b3, b4, b5, and b6 during 6 successive optical cycles. We can see that, when the modal field distribution of the side core mode LP_{11} is carrying OAM of $+\hbar$ or $-\hbar$, the modes could actually have the constant overlap integrals and phase matching condition:

$$\begin{aligned} I &= \int \left[R_a(x,y)\cdot e^{-j\beta_a z}\right]^* \cdot \left[R_b(x,y)\cdot e^{-jKz}\cdot e^{-j\beta_b z}\right] dxdy, \\ &= \int R_a(x,y)^* R_b(x,y)dxdy, \quad \text{When } \beta_a - \beta_b = K, \end{aligned} \tag{2.8}$$

The physical pictures in Figure 2.7 are not the whole story. The actual interaction between two modal fields includes not only the scalar field distribution (OAM) but also the vector field direction (SAM) as well. However, from this intuitive analysis, we can conclude:

1. CCC eigenmodes should be the ones with angular momentum;
2. QPM is achieved through angular momentum compensation.

2.1.3 Analytical Formula for CCC QPM Resonances

It turns out we can use a very simple analytical formula to predict and explain every resonance dips on the transmission spectrum of CCC fibers:

$$\Delta\beta = \beta_{|l_1|x_1} - \beta_{|l_2|x_2} \cdot \sqrt{1 + K^2R^2} + \Delta m \cdot K = 0, \tag{2.9}$$

where $\beta_{|l_1|x_1}$ and $\beta_{|l_1|x_1}$ are the propagation constants for $\mathrm{LP}_{|l_1|x_1}$ mode in the central core and $\mathrm{LP}_{|l_2|x_2}$ mode in the side core respectively, and the so called QPM number Δm takes every value in the following combinations:

$$\Delta m = \Delta l + \Delta s, \quad \Delta l = \pm|l_1| \pm |l_2|, \quad \Delta s = 0, \pm 1, \pm 2. \tag{2.10}$$

We can name this simple but powerful analytical formula as "QPM formula".

In this QPM formula, the "QPM number Δm" is the key to render multiple QPM resonances. The initial idea of determining the QPM number Δm for this formula originates from the analogy to Quantum Mechanics. Indeed, the difference in total angular momentum should come from the summation of the difference in OAM and the difference in SAM:

$$\Delta m \;\; = \;\; (l_1 - l_2) + (s_1 - s_2). \tag{2.11}$$

As has been pointed out, OAM quantum number is linked to the mode number of LP-modes $l_{1,2} = \pm|l_{1,2}|$. However, regarding SAM quantum number, we have to take 0 into account $s_{1,2} = \pm 1, 0$, which is generally not true for the spin of photons, but it makes the QPM formula fit the experimental observation very well. Until now we have characterized more than a dozen of different CCC samples, and the QPM formula always gives good agreement with experimental observation. In the next chapter, we will give the thorough and step-by-step proof of this QPM formula from

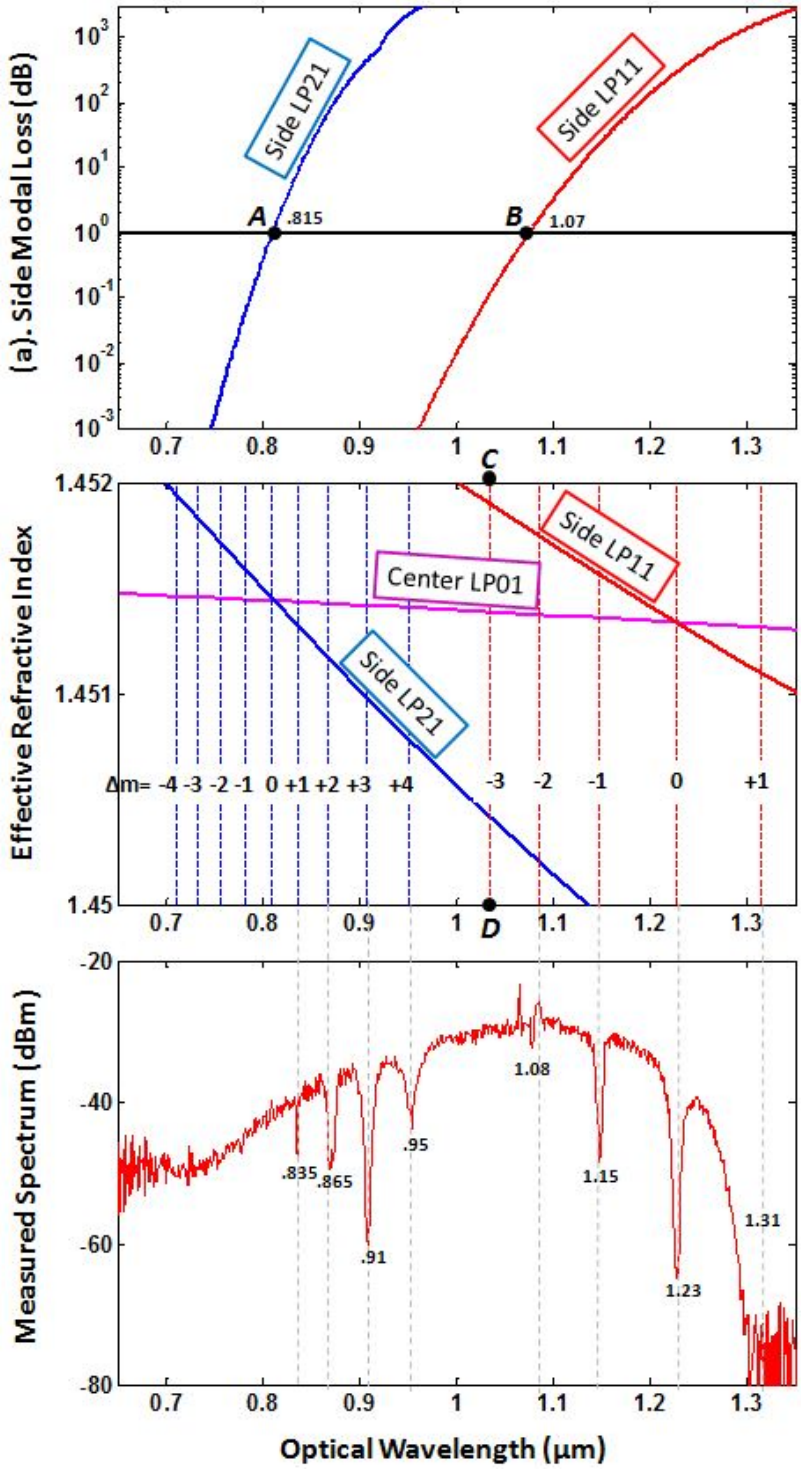

Figure 2.8: The QPM resonances explained by Eq. 2.9.

the first principle. Here, we take it as an imperial formula, and see how it fits the experimental observations.

Let's take the same transmission spectrum for example. The QPM formula predicts that LP_{01} and LP_{11} gives QPM number Δm =-3, -2, -1, 0, $+1$, $+2$, $+3$. Then, we can plot these resonance positions as red dash lines in Figure 2.8b. Thus, the resonances at 1080nm, 1150nm, 1230nm, and 1310nm correspond to the QPM number $\Delta m = -2, -1, 0, +1$. The resonance $\Delta m = -3$ designated by **C-D** line is invisible due to its negligible loss (comparing with point **B** in Figure 2.8a), which means that the light is bouncing back and forth between central and side core.

The QPM formula also predicts that LP_{01} and LP_{21} give QPM number $\Delta m = -4, -3, -2, -1,\ 0, +1, +2, +3, +4$. Similarly, we can plot these resonance positions as blue dash lines in Figure 2.8b. Thus, the resonances at 835nm, 865nm, 910nm, and 950nm correspond to the QPM number $\Delta m = +1, +2, +3, +4$, and all the other resonances are invisible due to negligible loss (comparing with point **A** in Figure 2.8a).

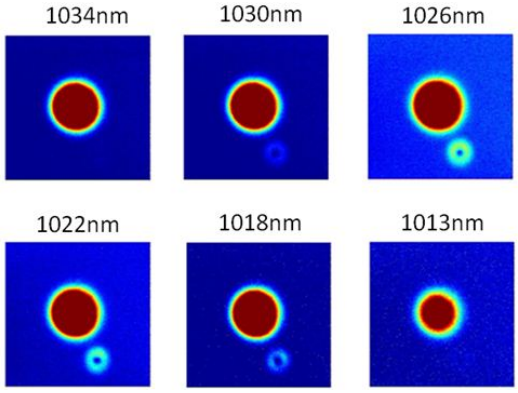

Figure 2.9: Detection of Lossless Resonance.

The wavelength positions predicted by this QPM formula in Eq.(2.9) fit the experimental observation very well. However, it is more convincing if we could detect the invisible resonance at the predicted wavelength position. In Figure 2.9, the detection of the **C-D** line is around 1026nm, where the phase matching condition couples the light from central core to the side core. It fits the prediction by QPM formula as well.

2.1.4 Measurement of Orbital Angular Momentum

In the previous sections, we have argued that the coupling between the central and side core in CCC fiber involves the angular momentum of optical waves and the eigenmodes of CCC fiber are the ones with orbital angular momentum $l\hbar$ and spin optical angular momentum $s\hbar$. Nevertheless, the analysis and proof presented above are kind of "indirect". Therefore, we need more direct evidence to demonstrate the angular momentum coupled optical waves in the CCC fibers. Here, we are going to demonstrate the direct measurement of orbital angular momentum which is carried by the eigenmodes of CCC fibers.

The experiment setup for measuring the orbital angular momentum of CCC eigenmodes is shown in Figure 2.10. The laser source in this setup is an "Toptica DL Pro" model with external cavity diode laser configuration. It can provide a narrow linewidth of less than 100KHz and a broad tunable range from 980nm to 1080nm. The grating spectrometer is used to monitor the wavelength of the tunable laser source.

In the last section, we have demonstrated that there is an invisible resonance around 1026nm, where the light is coupling forth and back between central and side

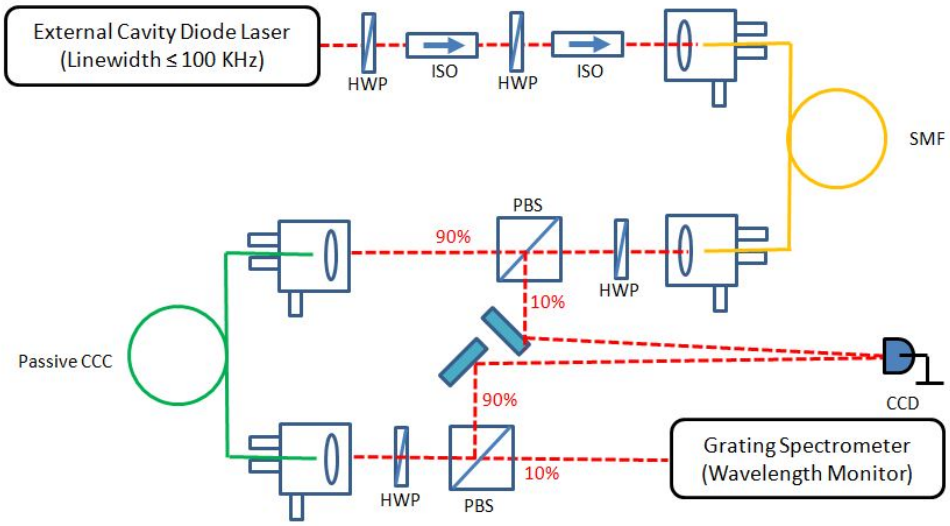

Figure 2.10: Experimental Setup for Measuring the Orbital Angular Momentum of CCC Eigenmodes.

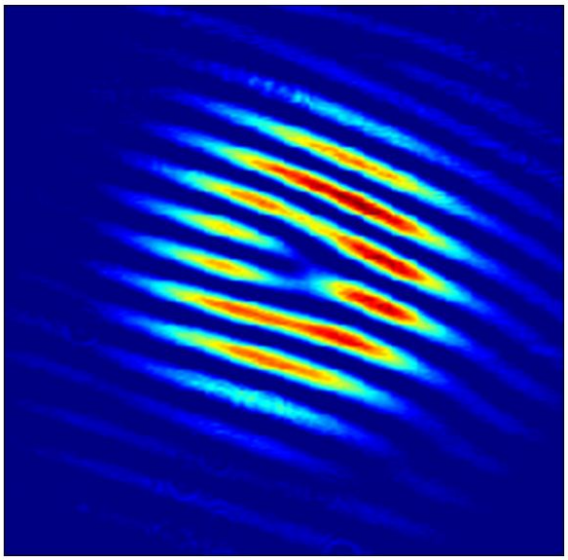

Figure 2.11: Measuring the Orbital Angular Momentum of CCC Eigenmodes.

core without any significant loss. During this detection, we have observed that the side core exhibits a ring-like intensity distribution as shown in Figure 2.9, and this ring-like intensity shape is consistent with the intensity pattern of the modes carrying non-zero orbital angular momentum. The QPM formula predicts that the orbital angular momentum of this resonance should be $l = \pm 1$. Let's use the setup in Figure 2.10 to verify the quantum number is $l = \pm 1$.

First, we tune the wavelength close to 1026nm to capture the resonance and ring-like side mode. Second, we couple the narrow linewidth signal into single mode fiber and then collimate the output out of the single mode fiber. Thus, we obtain a nearly-perfect plane wave after the single mode fiber. Then, we couple most of the signal into the CCC sample. After that, we let the signal from the side core ring-like mode interfere with the plane wave signal. The interference pattern is shown in Figure 2.11. By counting the misaligned number of interference fringes, we can know the quantum number of the orbital angular moment is ± 1 (*Marrucci et al.*, 2006), and it agrees with the prediction by QPM formula.

2.2 Effective Single-Mode Operation of CCC Fibers

2.2.1 Demonstration of Effective Single-Mode CCC

The same fiber sample that we have been exploring throughout this chapter is an effective single-mode CCC fiber. The center core of this fiber sample supports at least 5 different LP-modes, which are from lower-order to higher-order: LP_{01}, LP_{11}, LP_{21}, LP_{02}, LP_{31}. However, only the fundamental mode LP_{01} can propagate along this CCC fiber. We can call this kind of fiber as effective single-mode fiber.

Actually, the transmission spectrum of this particular fiber sample has implied that it is an effective single-mode CCC fiber. In Figure 2.12, we show the simulated transmission spectrum for each of 5 supported modes in this fiber sample: red solid curve is for LP_{01}, blue dash curve is for LP_{11}, green dash curve is for LP_{21}, cyan dash curve is for LP_{02}, and purple dash curve is for LP_{31}. We can see that all the other modes except LP_{01} have large loss across the whole spectrum. Thus, when optimizing the power transmission, we automatically optimize the excitation of fundamental mode LP_{01} at the launching end of the fiber. Even though there will be some small amount of other modes that get excited at the launching end, they will get stripped out of the central core by the large loss. Therefore, the transmission spectrum obtained at the output end of this fiber sample should only belong to the fundamental mode LP_{01}. Indeed, the red solid curve of simulated LP_{01} transmission spectrum gives good correspondence with experimental observed transmission spectrum.

The tool we use to obtain the simulation in Figure 2.12 is a self-developed numerical algorithm. In the next chapter, we will see that the multiple resonances designated by QPM number $\Delta m = \Delta l + \Delta s$ correspond to different physical origins. More specifically, the resonances with $\Delta s = 0$ correspond to the coupling induced by scalar refractive index perturbations. Similarly, $\Delta s = \pm 2$ correspond to the linear birefringence perturbations induced by linear stress, and $\Delta s = \pm 1$ correspond to the

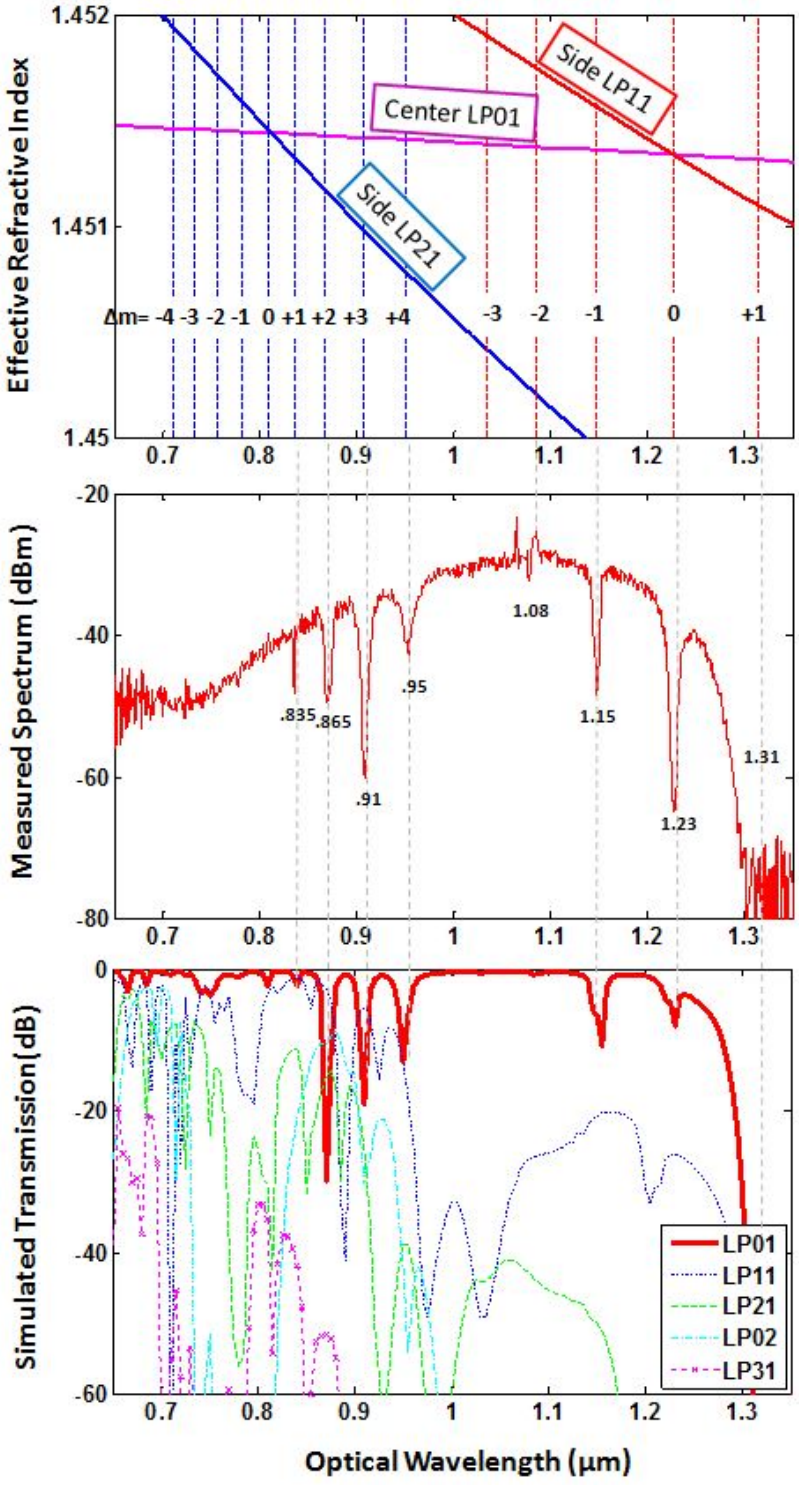

Figure 2.12: Explanation of CCC fiber single mode operation with FISTS simulation.

torsional birefringence perturbations induced by twist torsion. Thus, we need a tool that has the ability to simulate the optical fiber with twist torsion and linear stress. Up to date, there are no existing numerical method that has this ability and eligible speed. Therefore, we developed a numerical program called FISTS (FIber Simulator with Torsion and Stress), which is a BPM-based algorithm that has both the ability and eligible speed. Chapter V will be dedicated to discuss FISTS and other related simulation tools.

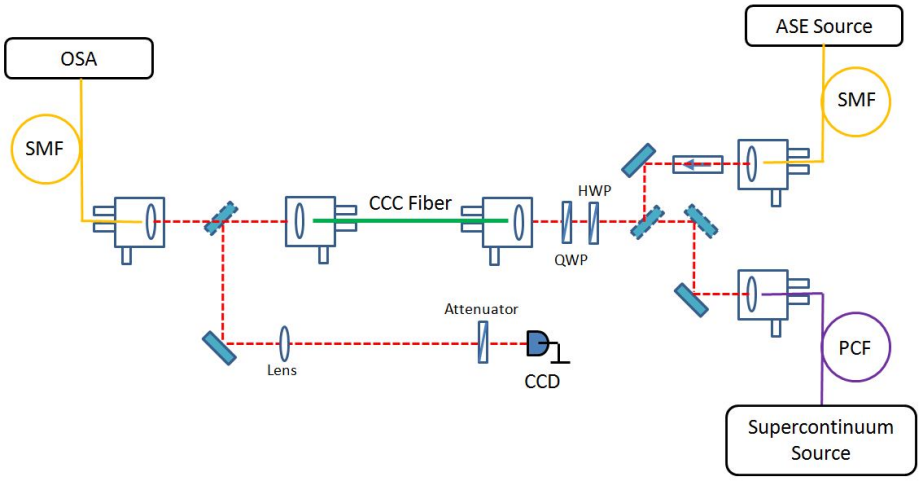

Figure 2.13: Measurement Setup for Characterizing The Performance of CCC Effective Single-Mode Operation.

To characterize the performance of CCC effective single-mode operation, we need measurement setup in Figure 2.13. The broadband source is sent into the fiber sample, and the signal out of the fiber sample is sent into the single mode fiber connected to an OSA. A flip mirror at the input setup gives us the flexibility to use either supercontinuum signal or ASE signal as broadband source. Another flip mirror at the output setup provides the flexibility to image the beam onto the CCD camera.

If the fiber sample supports multiple modes, we would observe spectrum beating on the OSA due to the modal dispersion. If the fiber sample supports a single mode, then the spectrum beating pattern would disappear. More details about this spectrum

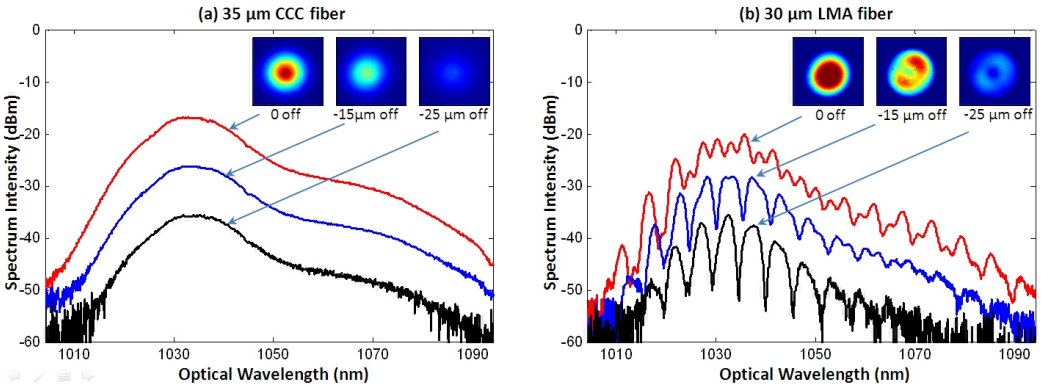

Figure 2.14: Single mode operation of CCC fibers compared with traditional LMA fibers.

beating pattern is discussed in the later section. Here, we apply this characterization to a 1.5-meter sample of this particular CCC fiber sample and a 2-meter 30um-diameter-core large mode area (LMA) fiber. The performances of both fiber samples are shown side by side in Figure 2.14.

For LMA fibers (see Figure 2.14b), even the optimum launching position ("0 off") gives the spectrum beating pattern (red curve). This optimum launching position is obtained by maximizing the power launched into the fiber sample. When the launching position is away off the optimum launching position, the higher order modes are more and more excited, and the spectrum pattern gets deeper and deeper ("-15 μm off" with blue curve and "-25 μm off" with black curve).

For effective single-mode CCC fibers (see Figure 2.14a), we can obtain the optimum launching position ("0 off") by maximizing the transmission power. Even off the optimum launching positions ("-15 μm off" and "-25 μm off"), there are no spectrum beating pattern at all. It means we have robust single-mode operation for this CCC fiber sample with this length. However, when the CCC fiber sample is short enough and the launching position is off the optimum position, we start to see slight spectrum beating pattern on the OSA and higher order mode profile on the CCD. For this particular fiber sample, experiment shows that any piece with more than 1.2 meter long could provide robust single mode operation.

2.2.2 S^2 Measurement of Effective Single-Mode CCC

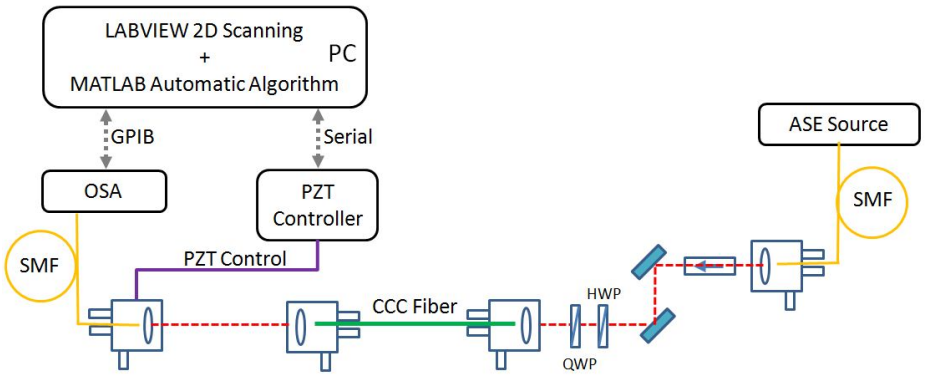

Figure 2.15: Setup for ASE-Based Spectrally and Spatially Resolved Imaging

The method to characterize the effective single-mode operation in the last section is rather qualitative. In this section, we present a more quantitative means to quantify the higher order mode percentage in the fiber sample, so we would quantify the performance of effective single mode operation of certain fiber sample. This method is called ASE-based Spectrally and Spatially resolved imaging. We can call it as S^2 measurement for convenience. Its experimental setup is shown in Figure 2.15.

The idea of this method comes from the fact that the Fourier transform of the power spectrum $S(\omega)$ is the group delay spectrum $\tau(n_{\text{eff}})$ as a function of modal effective refractive index n_{eff}. Since the power spectrum $S(\omega)$ is a superposition of all the fields after propagating through a certain length L:

$$S(\omega) \propto \left| \int e^{j\omega\tau} d\tau \right|, \tag{2.12}$$

we have the Fourier Transform of the power spectrum as

$$\tau(n_{\text{eff}}) \propto \mathcal{F}\left[S(\omega)\right]. \tag{2.13}$$

Here is just simple analysis to demonstrate the principle. To apply S^2 technique and extract the modal spectrum, we need rigorous and detailed derivations, which can be

found in references (*Nicholson et al.*, 2008).

The analysis above basically shows that the modal spectrum can be extracted by performing a Fourier transform to the power spectrum. This also mathematically explains the direct connection between spectrum beating pattern and the number of supported modes. More specifically, when the spectrum has no beating pattern but smooth DC signal, the Fourier transform of this power spectrum should have only the fundamental frequency (zero frequency), which shows the modal spectrum has only a single component. When the power spectrum has a beating pattern, the Fourier transform of the beating pattern would also show the frequency peaks other than fundamental frequency, which means we have multiple modes.

In the experiment setup in Figure 2.15, we use ASE signal as broadband source to catch the spectrum beating. A single mode fiber is aligned on the nanometer-precession adjustment stage to receive the signal out of the fiber sample and send the signal to the OSA. Since the reception area of this single mode fiber is much smaller than the beam size (or we can make the beam size larger by choosing the large focal length lens to collimate the beam), we can scan the single mode fiber reception end over the 2D plane of beam cross section point by point. By Fourier transform the power spectrum point by point, we can have the modal spectrum point by point across the 2D plane. In this way, we can obtain the 2D spatially and spectrally resolved image of the beam coming out of the fiber sample.

For the 1.5 meter of the passive CCC sample, the S^2 measured spacial profiles for LP_{11} mode and LP_{21} are shown in Figure 2.16. Due to the much shorter length of the fiber used for characterization, the S^2-measured spacial profiles of higher order modes are not as "pretty" as the ones shown in the reference, but they indeed show important physical information:

1. The relative intensity of higher order modes are more than 30dB/m down compared with fundamental mode, which indicates this short piece of uncoiled CCC

fiber is truly the effective single-mode large-mode-area fiber.

2. The spacial pattern of the higher order modes are ring-like, which also indicates the fact that the eigenmodes of CCC fibers are the ones carrying optical spin and orbital angular momentum.

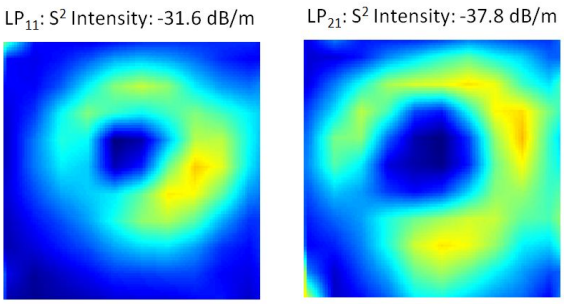

Figure 2.16: S^2 Measured Higher-Order Mode Spatial Distribution

One interesting thing is to consider such a situation: we launch a 100nm-broadband ASE source into a 1.5meter multi-mode fiber sample with 0.0002 modal effective-refractive-index difference between fundamental mode LP_{01} and first-order mode LP_{11} (typical number for 35um 0.06NA central core of CCC fibers), so the phase delay between the two modes through such a fiber with 1.5meter length is about 1 ps. But the coherent time of 100nm-bandwidth source is only about 30fs, which means the modes are separated so well that the interference between these two modes should not happen. Then, why do we see the spectrum beating even with a fiber longer than 1.5meter? This is actually because the grating in the optical spectrum analyzer stretch the coherent time of the incoming frequency component by narrowing the spectrum with a grating resolution. Therefore, it is critical to have a grating resolution narrow enough to see the beating pattern. With simple calculation, for 1.5meter of this particular fiber, we need at least 1nm-bandwidth grating resolution, and for 15meter we need at least 0.1nm-bandwidth. Fortunately, our OSA has a resolution as high as 0.05nm, which guarantees the proper working of the S^2 measurement.

2.2.3 High Power Fiber Laser with Effective Single-Mode CCC Fibers

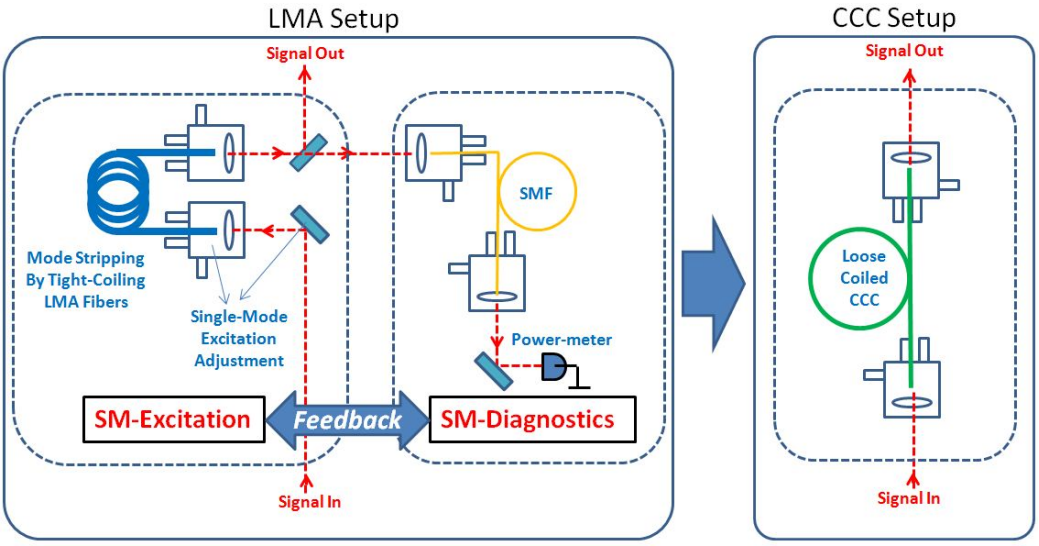

Figure 2.17: Effective Single-Mode Operation for LMA and CCC Setup.

Effective single-mode large-mode-area fibers are critical for developing kilowatt-level high power fiber lasers. Usually, the goal of high power fiber lasers is either to achieve high average power in CW laser setup or to achieve high energy pulse in pulsed laser amplifier setup. For both scenarios, implementing effective single-mode large-mode-area fibers is crucial to increase the power level and maintain the beam quality at the same time.

Before effective single-mode CCC fibers are invented, we use traditional LMA fibers and effective single-mode techniques to fulfill effective single-mode operation. In Figure 2.17, we can see how complicated it is to work with traditional LMA to obtain single-mode operation. First, the LMA fiber has to be tightly coiled to strip off the higher order modes. The coiling radius varies for different core size and core NA, and thus has to be calculated for different fibers. Second, there has to be a single-mode diagnostics stage, and the excitation at the signal input end of LMA has to cooperate with the excitation at input end of single-mode diagnostics stage. By adjusting both nanometer-precision adjustment stages and several associated mirrors,

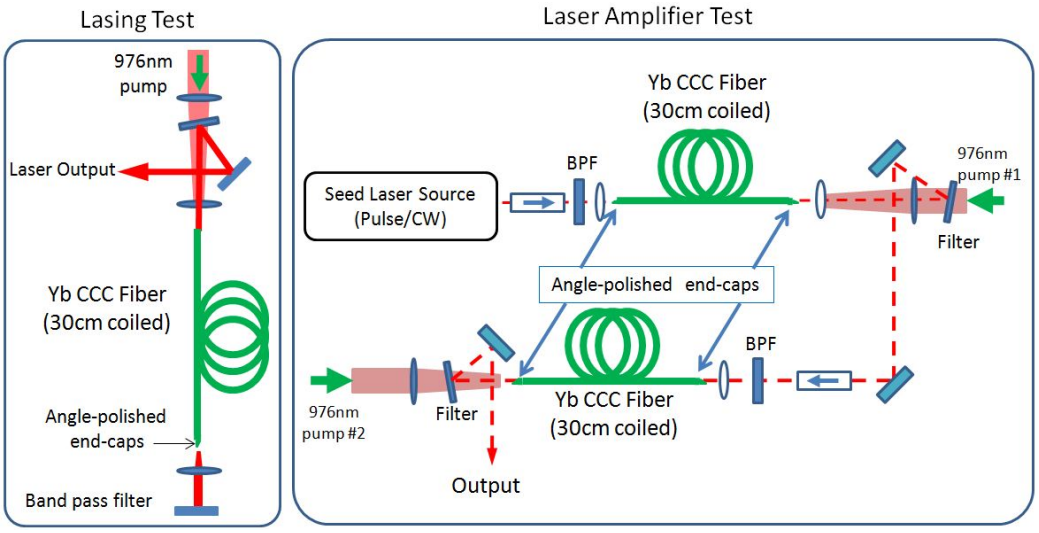

Figure 2.18: Experimental Setup for Lasing Test and Laser Amplifier Test (System Operated by Cheng Zhu and Shenghong Huang).

we can maximize the power output at the diagnostics stage. It indeed requires experienced skills and time-consuming effort to achieve successful single-mode operation with LMA setup, and most of the time this setup is not stable enough to stay working for a long time and can not provide robust and excellent beam quality as well.

However, with CCC fibers in Figure 2.17, it is very easy to achieve single-mode operation comparing with LMA fibers. It is truly working just like a single-mode fiber. The most important point is that, CCC fibers can be spliced together and still provide large-mode-area and single mode operation in a monolithic system. This is the dominating advantage of CCC fibers over LMA fibers.

The experimental setup for laser and laser amplifier with CCC fibers are shown in Figure 2.18. So far, we have successfully designed up to 37um-diameter Yb-doped double-clad CCC fibers with effective single-mode operation. For 37um polymer-coating CCC with 400um-diameter cladding, we have achieved 600Watts CW laser with diffraction-limited beam quality. For 37um air-clad CCC with 250um-diameter cladding, we have achieved 500Watts narrow-linewidth amplified laser signal also with good beam quality.

CHAPTER III

Theoretical Model in Helicoidal Coordinates System

In this chapter, we will mainly focus on building a rigorous theoretical model from the first principle and trying to explain and predict CCC fibers' performance with analytically derived expressions.

First, we introduce the covariant and contravariant dual space in the curvilinear helicoidal coordinates system. In this coordinates system, we re-formulate the Maxwell equation and derive the general form for coupled mode equations for optical parallel waveguides.

Then, we can formulate the CCC model and CCC anisotropic permittivity in this coordinates system, where CCC structure indeed becomes "unwounded". This means we can use the coupled mode equations derived for optical parallel waveguide to analyze this CCC model.

The key of this rigorous theoretical model is to obtain the eigenmodes of CCC structures: helical modes inside each isotropic core. Plugging these helical modes into the coupled mode equation derived in curvilinear Helicoidal coordinates, we can mathematically prove the analytical QPM formula by analytical derivations.

3.1 Maxwell Equation and Coupled Mode Equations in Helicoidal Coordinates and Curvilinear Reference Frame

3.1.1 Covariant and Contravariant Dual Space

In the anti-clockwise rotating helical system, we choose the so called Helicoidal coordinates $\{X, Y, Z\}$ as

$$\begin{cases} X = x \cdot \cos \tau z + y \cdot \sin \tau z, \\ Y = -x \cdot \sin \tau z + y \cdot \cos \tau z, \\ Z = z, \end{cases} \tag{3.1}$$

which are three single-valued functions of Cartesian coordinates $\{x, y, z\}$, and by definition, they form a so called general or curvilinear coordinates system. As common, we designate $\{X, Y, Z\}$ as $\{u^1, u^2, u^3\}$ for further discussion:

$$\begin{pmatrix} X \\ Y \\ Z \end{pmatrix} = \begin{pmatrix} u^1 \\ u^2 \\ u^3 \end{pmatrix}. \tag{3.2}$$

Here, we define u^i-constant surfaces as **coordinate surfaces** and their u^i-variable intersection curves as **coordinates curves**. The basis whose vectors are tangential to these curves are **covariant basis** $\{\mathbf{e}_1, \mathbf{e}_2, \mathbf{e}_3\}$. Correspondingly, we also call $\{u^1, u^2, u^3\}$ as **contravariant coordinates**.

The relation "tangential to coordinates curves" actually means that the vectors of covariant basis are along the coordinates curves, so we can have:

$$\mathbf{e}_i = \frac{\partial \mathbf{R}}{\partial u^i}. \tag{3.3}$$

In order to further write down $\mathbf{e}_i$ explicitly, we need to express $\mathbf{R}$ explicitly with the

Cartesian basis as $\mathbf{R} = x\hat{\mathbf{x}} + y\hat{\mathbf{y}} + z\hat{\mathbf{z}}$. Also, we need the inverse transformation of Eq.(3.1) to express $\{x, y, z\}$ with $\{X, Y, Z\}$ as:

$$\begin{cases} x = X \cdot \cos\tau Z - Y \cdot \sin\tau Z, \\ y = X \cdot \sin\tau Z + Y \cdot \cos\tau Z, \\ z = Z. \end{cases} \tag{3.4}$$

Plugging Eq.(3.4) into Eq.(3.3), we have the covariant basis explicitly expressed as

$$\begin{cases} \mathbf{e}_1 = \hat{\mathbf{x}} \cdot \cos\tau Z - \hat{\mathbf{y}} \cdot \sin\tau Z, \\ \mathbf{e}_2 = \hat{\mathbf{x}} \cdot \sin\tau Z + \hat{\mathbf{y}} \cdot \cos\tau Z, \\ \mathbf{e}_3 = \hat{\mathbf{z}} + \tau(x\hat{\mathbf{x}} + y\hat{\mathbf{y}}), \end{cases} \tag{3.5}$$

where $\{\hat{\mathbf{x}}, \hat{\mathbf{y}}, \hat{\mathbf{z}}\}$ are **Cartesian basis**.

This covariant basis in Eq.(3.5) is the one that we are going to use throughout this chapter. Here, we can see, the covariant vectors $\mathbf{e}_1$ and $\mathbf{e}_2$ are two orthogonal unit vector that are rotating with the "local" reference frame in xy plane. As has been point out earlier, within this local reference frame, the CCC structure is "unwounded", which is the whole purpose of using the general (curvilinear) coordinates system. The other covariant vector $\mathbf{e}_3$ is orthogonal to $\mathbf{e}_1$ and $\mathbf{e}_2$ when on-axis, and it coincides with $\hat{\mathbf{z}}$ on the rotation axis. However, it is nonorthogonal and oblique with respect to $\mathbf{e}_1$ and $\mathbf{e}_2$ when off-axis, i.e. $\tau(x\hat{\mathbf{x}}+y\hat{\mathbf{y}}) \neq 0$. This is an important feature of covariant basis vector $\mathbf{e}_3$ to keep in mind.

To fully express an nonorthogonal oblique coordinates system, we have to introduce the so called **dual space** and **reciprocal basis**. Here, the reciprocal basis of covariant basis $\{\mathbf{e}_1, \mathbf{e}_2, \mathbf{e}_3\}$ is the so called **contravariant basis** $\{\mathbf{e}^1, \mathbf{e}^2, \mathbf{e}^3\}$. The details about dual space and reciprocal basis can be found in references (*Borisenko et al.*, 1979). In general, a vector space must require two spaces represented by two different sets of vector basis. In fact, an orthogonal unitary coordinates system can

be seen as a special case for general nonorthogonal coordinates system, where covariant and contravariant basis in such an orthogonal unitary coordinates system (e.g. Cartesian Coordinates system) coincide with each other.

The contravariant basis is defined to be orthogonal to the coordinates surfaces, so we obtain the contravariant basis by taking the gradient of these surfaces:

$$\mathbf{e}^i \;=\; \nabla u^i. \tag{3.6}$$

Plugging Eq.(3.1) into Eq.(3.6), we can have contravariant basis as

$$\begin{cases} \mathbf{e}^1 = \hat{\mathbf{x}} \cdot \cos\tau Z + \hat{\mathbf{y}} \cdot \sin\tau Z + \tau Y \hat{\mathbf{z}}, \\ \mathbf{e}^2 = -\hat{\mathbf{x}} \cdot \sin\tau Z + \hat{\mathbf{y}} \cdot \cos\tau Z - \tau X \hat{\mathbf{z}}, \\ \mathbf{e}^3 = \hat{\mathbf{z}}. \end{cases} \tag{3.7}$$

This is a different set of basis other than the covariant basis in Eq.(3.5). We can see that the basis vector $\mathbf{e}^3$ is always along the $\hat{\mathbf{z}}$, which is consistent with the definition that $\mathbf{e}^3$ is always orthogonal to the Z-coordinates surface. X-coordinates and Y-coordinates surfaces are not easy to visualize, but they can be seen as the twisted xz and yz plane following the helix path. Thus, in general, the vectors $\mathbf{e}^1$ and $\mathbf{e}^2$ are nonorthogonal and oblique with respect to the vector $\mathbf{e}^3$.

Correspondingly, the coordinates based on the contravariant basis is called **covariant coordinates** represented as $\{u_1, u_2, u_3\}$. Since an unique spacial point can be expressed as both contravariant coordinates in covariant basis and covariant coordinates in contravariant basis, we have the relation $\Sigma_i u_i \mathbf{e}^i = \Sigma_j u^j \mathbf{e}_j$. Defining the so called **metric tensor** $g_{ij} = \mathbf{e}_i \cdot \mathbf{e}_j$, we can link covariant coordinates $\{u_1, u_2, u_3\}$ and contravariant coordinates $\{u^1, u^2, u^3\}$ as

$$u_i \;=\; \Sigma_j \; g_{ij} \; u^j. \tag{3.8}$$

Using Eq.(3.1), Eq.(3.5) and Eq.(3.8), we have the covariant coordinates as

$$\begin{cases} u_1 = X - (\tau Z) \cdot Y, \\ u_2 = Y + (\tau Z) \cdot X, \\ u_3 = [1 + \tau^2 (X^2 + Y^2)] Z. \end{cases} \tag{3.9}$$

3.1.2 Maxwell Equations in Helicoidal Coordinates System

Now, with the contravariant coordinates in covariant basis and covariant coordinates in contravariant basis, we can rewrite the Maxwell equations in this dual space with this Helicoidal coordinates system $\{X, Y, Z\}$ or $\{u^1, u^2, u^3\}$.

First, let's rewrite the curl of a general vector field $\mathbf{F}$ in this dual space. As usual, the curl of the vector field $\mathbf{F}$ is calculated by the line integral of $\mathbf{F}$ around an infinitesimal close path

$$(\nabla \times \mathbf{F}) \cdot \mathbf{n} = \lim_{L \to 0} \frac{1}{L} \int \mathbf{F} \cdot d\mathbf{l}. \tag{3.10}$$

However, comparing with the case in Cartesian coordinates, the differences are: the basis of vector $\mathbf{n}$ on the left-hand-side must take the contravariant basis $\{\mathbf{e}^1, \mathbf{e}^2, \mathbf{e}^3\}$ because it is always orthogonal to the coordinates surfaces; the basis of vector $d\mathbf{l}$ on the right-hand-side must take the covariant basis $\{\mathbf{e}_1, \mathbf{e}_2, \mathbf{e}_3\}$ because it is always along the coordinates curves. The Eq.(3.10) will end up with

$$(\nabla \times \mathbf{F}) \cdot \mathbf{e}^1 = \frac{1}{\sqrt{g}} \left[\frac{\partial}{\partial u^2} (\mathbf{F} \cdot \mathbf{e}_3) - \frac{\partial}{\partial u^3} (\mathbf{F} \cdot \mathbf{e}_2) \right], \tag{3.11}$$

where we choose the line integral on the $\mathbf{e}_1$-constant coordinate surface, and g is defined as the determination of metric tensor g_{ij}. For Helicoidal coordinates, we have

$$g \;=\; \det |g_{ij}| = 1. \tag{3.12}$$

In Eq.(3.11), the left-hand-side is the curl's contravariant component $(\nabla \times \mathbf{F})^i = (\nabla \times \mathbf{F}) \cdot \mathbf{e}^i$, while the right-hand-side is a function of the $\mathbf{F}$ vector's covariant component $F_i = \mathbf{F} \cdot \mathbf{e}_i$. Then, we can write down the equation for the curl of the vector field $\mathbf{F}$:

$$\nabla \times \mathbf{F} = \begin{vmatrix} \mathbf{e}_1 & \mathbf{e}_2 & \mathbf{e}_3 \\ \frac{\partial}{\partial X} & \frac{\partial}{\partial Y} & \frac{\partial}{\partial Z} \\ F_1 & F_2 & F_3 \end{vmatrix} = [\{\nabla^i\} \otimes \{F_i\}]\mathbf{e}_i, \tag{3.13}$$

where the $\{\nabla^i\} \otimes \{F_i\}$ catches the inner index rotation inside the determination. So in the Helicoidal coordinates, the curl of a vector field $\nabla \times \mathbf{F}$ is finally expressed with the following quantities: covariant basis $\mathbf{e}_i$, covariant components of the vector field $\{F_i\} = \{F_1, F_2, F_3\}$, and the derivative with respect to contravariant coordinates $\{\nabla^i\} = \{\nabla^1, \nabla^2, \nabla^3\} = \{\partial/\partial u^1, \partial/\partial u^2, \partial/\partial u^3\} = \{\partial/\partial X, \partial/\partial Y, \partial/\partial X\}$. Therefore, for the two curl equations in Maxwell equations, we have

$$\{\{\nabla^i\} \otimes \{E_i\}\} = -\frac{\partial}{\partial t}\{B^i\}, \tag{3.14}$$

$$\{\{\nabla^i\} \otimes \{H_i\}\} = \frac{\partial}{\partial t}\{D^i\}. \tag{3.15}$$

For the two divergence equations in Maxwell equation, we can write down as

$$\{\nabla^i\} \cdot \{B^i\} = 0, \tag{3.16}$$

$$\{\nabla^i\} \cdot \{D^i\} = 0, \tag{3.17}$$

where Einstein's notation is applied. Assuming monochromatic field, we can rewrite Eq.(3.14) and Eq.(3.15) as

$$\{\{\nabla^i\} \otimes \{E_i\}\} = -j\omega\{B^i\}, \tag{3.18}$$

$$\{\{\nabla^i\} \otimes \{H_i\}\} = j\omega\{D^i\}. \tag{3.19}$$

These two equations are going to be used in the later sections to derive the coupled mode equations in the Helicoidal coordinates system.

3.1.3 Cartesian to Helicoidal Coordinates Transformation

Regarding one-to-one principle from Cartesian coordinates $\{x, y, z\}$ to Helicoidal Coordinates $\{X, Y, Z\}$, we define the Jacobian matrix of Cartesian coordinates $\{x, y, z\}$ with respect to Helicoidal Coordinates $\{X, Y, Z\}$ as $\mathbf{J}^{x,y,z}_{X,Y,Z}$:

$$\mathbf{J}^{x,y,z}_{X,Y,Z} = \frac{\partial(x, y, z)}{\partial(X, Y, z)}, \tag{3.20}$$

$$= \begin{pmatrix} \cos\tau z & -\sin\tau z & -\tau X \sin\tau z - \tau Y \cos\tau z \\ \sin\tau z & \cos\tau z & \tau X \cos\tau z - \tau Y \sin\tau z \\ 0 & 0 & 1 \end{pmatrix}. \tag{3.21}$$

The name of "Jacobian matrix" comes from the definition that the determination $J = \det|\mathbf{J}^{x,y,z}_{X,Y,Z}|$ is called as "Jacobian of $\{x, y, z\}$ with respect to $\{X, Y, Z\}$". The Jacobian matrix $\mathbf{J}$ is actually characterizing the coordinates transformation from Helicoidal Coordinates to Cartesian coordinates:

$$\mathbf{J}^{\text{contrav.}}_{\text{Hel.}\to\text{Car.}} = \mathbf{J}^{x,y,z}_{X,Y,Z}, \tag{3.22}$$

which transforms from the coordinates X, Y, Z in subscripts to the coordinates x, y, z in superscripts. From now on, we will use $\mathbf{J} = \mathbf{J}^{x,y,z}_{X,Y,Z}$ for convenience.

Therefore, we have the transformation from contravariant component in Helicoidal coordinates $\{F^i\}_{\text{Hel.}}$ to Cartesian vector $\mathbf{F}_{\text{Car.}}$:

$$\mathbf{F}_{\text{Car.}} = \mathbf{J}\{F^i\}_{\text{Hel.}}. \tag{3.23}$$

Then, the inverse transformation gives the transformation from Cartesian vector $\mathbf{F}_{\text{Car.}}$

to contravariant component in Helicoidal coordinates $\{F^i\}_{\text{Hel.}}$ with the inverse Jacobian matrix $\mathbf{J^{-1}}$:

$$\{F^i\}_{\text{Hel.}} = \mathbf{J^{-1}}\mathbf{F}_{\text{Car.}}. \tag{3.24}$$

According to the relation of covariant and contravariant components, we can express the transformation from the covariant components in Helicoidal coordinates $\{F_i\}_{\text{Hel.}}$ to Cartesian vector $\mathbf{F}_{\text{Car.}}$ with the transpose of inverse Jacobian matrix $(\mathbf{J^{-1}})^{\mathbf{T}}$:

$$\mathbf{F}_{\text{Car.}} = (\mathbf{J^{-1}})^{\mathbf{T}}\{F_i\}_{\text{Hel.}}. \tag{3.25}$$

With these transformations between Helicoidal coordinates and Cartesian coordinates, we can apply the constitutive relation to the right-hand-side of Eq.(3.18) and Eq.(3.19) , and have the following expressions:

$$\begin{aligned} \{B^i\} &= \mathbf{J^{-1}}\mathbf{B}_{\text{Car.}}, \\ &= \mathbf{J^{-1}}\mu_0\tilde{\mu}_c\mathbf{H}_{\text{Car.}}, \\ &= \mu_0\mathbf{J^{-1}}\tilde{\mu}_c(\mathbf{J^{-1}})^{\mathbf{T}}\{H_i\}, \end{aligned} \tag{3.26}$$

where $\tilde{\mu}_c$ tensor is expressed in Cartesian coordinates. Similarly, we have

$$\{D^i\} = \epsilon_0\mathbf{J^{-1}}\tilde{\epsilon}_c(\mathbf{J^{-1}})^{\mathbf{T}}\{E_i\}, \tag{3.27}$$

where $\tilde{\epsilon}_c$ tensor is expressed in Cartesian coordinates.

Now, by substituting Eq.(3.26) and Eq.(3.27) into Eq.(3.18) and Eq.(3.19), we can express the two curl Maxwell equations with covariant coordinates $\{u_1, u_2, u_3\}$ and covariant basis $\{\mathbf{e}_1, \mathbf{e}_2, \mathbf{e}_3\}$. Thus, we can write down the two curl Maxwell equations in Helicoidal coordinates (Eq.(3.18) and Eq.(3.19)) in the same mathematical form

as in Cartesian coordinates but with different meaning of each physical quantity:

$$\nabla \times \mathbf{E} = -j\mu_0\omega\tilde{\mu}_h\mathbf{H}, \tag{3.28}$$

$$\nabla \times \mathbf{H} = j\epsilon_0\omega\tilde{\epsilon}_h\mathbf{E}, \tag{3.29}$$

where the curl product operates with the covariant basis $\{\mathbf{e}_i\}$, the vector field is expressed with covariant components $\mathbf{E} = \{E_1, E_2, E_3\}, \mathbf{H} = \{H_1, H_2, H_3\}$, the derivative is with respect to the contravariant coordinates $\nabla = \{\partial/\partial u^1, \partial/\partial u^2, \partial/\partial u^3\}$, and the new electric permittivity tensor $\tilde{\epsilon}_h$ and magnetic permeability tensor $\tilde{\mu}_h$ are

$$\tilde{\epsilon}_h = \mathbf{J^{-1}}\tilde{\epsilon}_c(\mathbf{J^{-1}})^{\mathbf{T}}, \tag{3.30}$$

$$\tilde{\mu}_h = \mathbf{J^{-1}}\tilde{\mu}_c(\mathbf{J^{-1}})^{\mathbf{T}}. \tag{3.31}$$

Therefore, we can have such a general conclusion: In any general coordinates system regardless of their orthogonality or unitary properties, the Maxwell equations can keep the same mathematical form as in Cartesian coordinates system, and the only difference is captured by the electric permittivity tensor $\tilde{\epsilon}$ and magnetic permeability tensor $\tilde{\mu}$, which follow the transformation in Eq.(3.30) and Eq.(3.31).

More simply put, in a new coordinates system other than Cartesian coordinates, instead of changing the mathematical form of Maxwell equations written in Cartesian coordinates, we can change the material property (changing the electric permittivity tensor $\tilde{\epsilon}$ and magnetic permeability tensor $\tilde{\mu}$) for the convenience of keeping the same mathematical form in the new coordinates system. Taking the homogenous isotropic medium for example, a scalar number of the electric permittivity or magnetic permeability can turn into a tensor with inhomogeneous distribution and anisotropic off-diagonal components: the homogenous isotropic material will appear to be inhomogenous and anisotropic in the new coordinates system. However, by sacrificing the material simplicity (go from homogenous isotropic to inhomogenous anisotropic), it is

also possible that, in the new coordinates system, the complex geometry of unsolved problem can have a simple and straightforward geometry, which would thus provide an easy approach of solution. This is the general idea of building the theoretical model for CCC structures in the Helicoidal coordinates system.

3.1.4 Coupled Mode Equations in Helicoidal Coordinates System

Intuitively, working with the Helicoidal coordinates will make CCC structure's geometry become straight parallel waveguides, so it allows us to employ analytical means (i.e. coupled mode equations) to analyze the modal propagation. Therefore, it is essential to formulate the coupled mode equations in the Helicoidal coordinates based on the Maxwell equations Eq.(3.28) and Eq.(3.29).

First, in the Helicoidal coordinates, we assume two modal field $\{\mathbf{E_a}, \mathbf{H_a}\}$ and $\{\mathbf{E_b}, \mathbf{H_b}\}$ are propagating with slowly varying envelope $A(Z)$ and $B(Z)$ respectively. Thus, we have the two curl Maxwell equations for each individual modal fields as

$$\nabla \times \mathbf{E_{a,b}} = -j\omega\mu_0\tilde{\mu}_h\mathbf{H_{a,b}}, \quad \nabla \times \mathbf{H_{a,b}} = j\omega\epsilon_0(\tilde{\epsilon}_h^s + \Delta\tilde{\epsilon}_h^{a,b})\mathbf{E_{a,b}}, \tag{3.32}$$

and for two curl Maxwell equations with total fields $A(Z)\mathbf{E_a}+B(Z)\mathbf{E_b}$ and $A(Z)\mathbf{H_a}+B(Z)\mathbf{H_b}$, we have

$$\nabla \times [A(Z)\mathbf{E_a} + B(Z)\mathbf{E_b}] = -j\omega\mu_0\tilde{\mu}_h [A(Z)\mathbf{H_a} + B(Z)\mathbf{H_b}], \tag{3.33}$$

$$\nabla \times [A(Z)\mathbf{H_a} + B(Z)\mathbf{H_b}] = j\omega\epsilon_0(\tilde{\epsilon}_h^s + \Delta\tilde{\epsilon}_h^a + \Delta\tilde{\epsilon}_h^b + \Delta\tilde{\epsilon}_h^{ptb}) [A(Z)\mathbf{E_a} + B(Z)\mathbf{E_b}]. \tag{3.34}$$

where $\tilde{\epsilon}_h^s$ is the substrate permittivity, $\Delta\tilde{\epsilon}_h^a, \Delta\tilde{\epsilon}_h^b$ are the permittivity differences for guiding the two modal fields, and $\Delta\tilde{\epsilon}_h^{ptb}$ is the general perturbations.

For an arbitrary scalar function $f(Z)$, which actually implies the slowly varying

envelope $A(Z)$ or $B(Z)$, Eq.(3.13) gives

$$\begin{aligned}
\nabla \times [f(Z)\mathbf{F}] &= \begin{vmatrix} \mathbf{e}_1 & \mathbf{e}_2 & \mathbf{e}_3 \\ \frac{\partial}{\partial X} & \frac{\partial}{\partial Y} & \frac{\partial}{\partial Z} \\ f(Z)F_1 & f(Z)F_2 & f(Z)F_3 \end{vmatrix}, \\
&= f(Z)[\nabla \times \mathbf{F}] + \begin{vmatrix} \mathbf{e}_1 & \mathbf{e}_2 & \mathbf{e}_3 \\ 0 & 0 & \frac{\partial}{\partial Z} f(Z) \\ F_1 & F_2 & F_3 \end{vmatrix}, \\
&= f(Z)[\nabla \times \mathbf{F}] + \frac{df(Z)}{dZ}\{-F_2, F_1, 0\}, \qquad (3.35)
\end{aligned}$$

We define unit vector $\hat{\mathbf{Z}}$ as:

$$\hat{\mathbf{Z}} = \frac{\mathbf{e}_3}{|\mathbf{e}_3|} = \{0, 0, 1\}, \qquad (3.36)$$

Then, we can rewrite Eq.(3.35) more compact as

$$\nabla \times [f(Z)\mathbf{F}] = f(Z)[\nabla \times \mathbf{F}] + \frac{df(Z)}{dZ}[\hat{\mathbf{Z}} \times \mathbf{F}]. \qquad (3.37)$$

Using Eq.(3.32)-(3.34) and Eq.(3.37), we can obtain

$$\begin{aligned}
\frac{dA(Z)}{dZ}[\hat{\mathbf{Z}} \times \mathbf{E_a}] + \frac{dB(Z)}{dZ}[\hat{\mathbf{Z}} \times \mathbf{E_b}] &= 0, \qquad (3.38) \\
\frac{dA(Z)}{dZ}[\hat{\mathbf{Z}} \times \mathbf{H_a}] + \frac{dB(Z)}{dZ}[\hat{\mathbf{Z}} \times \mathbf{H_b}] &= j\omega\epsilon_0(\Delta\tilde{\epsilon}_h^a + \Delta\tilde{\epsilon}_h^{ptb})\mathbf{E_b}B(Z) \\
&\quad + j\omega\epsilon_0(\Delta\tilde{\epsilon}_h^b + \Delta\tilde{\epsilon}_h^{ptb})\mathbf{E_a}A(Z). \qquad (3.39)
\end{aligned}$$

Now, we substitute Eq.(3.38) and Eq.(3.39) into the following integrals which integrate over the entire Z-constant surface (coordinate surface):

$$\int [\mathbf{E_a^*} \cdot (3.39) - \mathbf{H_a^*} \cdot (3.38)] dS|_Z = 0, \ \int [\mathbf{E_b^*} \cdot (3.39) - \mathbf{H_b^*} \cdot (3.38)] dS|_Z = 0, \qquad (3.40)$$

where we have the area $dS|_Z$ expressed in the dual space of Helicoidal coordinates with $\sqrt{g} = 1$ and $|\mathbf{e}^3| = 1$:

$$dS|_Z \quad = \quad \sqrt{g}|\mathbf{e}^3|dXdY, \tag{3.41}$$

Substituting Eq.(3.41) and the relations

$$\mathbf{E}^* \cdot (\hat{\mathbf{Z}} \times \mathbf{H}) = -\hat{\mathbf{Z}} \cdot (\mathbf{E}^* \times \mathbf{H}), \quad \mathbf{H}^* \cdot (\hat{\mathbf{Z}} \times \mathbf{E}) = \hat{\mathbf{Z}} \cdot (\mathbf{E} \times \mathbf{H}^*), \tag{3.42}$$

into Eq.(3.40), we can obtain the forms:

$$\begin{cases} dA/dz + X_{ab} \cdot dB/dz = -j\kappa_{aa} \cdot A - j\kappa_{ab} \cdot B, \\ dB/dz + X_{ab} \cdot dA/dz = -j\kappa_{ba} \cdot A - j\kappa_{bb} \cdot B. \end{cases} \tag{3.43}$$

To include the longitudinal dependence into the equation, we take the substitution

$$\mathbf{E}_{a,b} \rightarrow \mathbf{E}_{a,b} e^{-j\beta_{a,b}z}, \quad \mathbf{H}_{a,b} \rightarrow \mathbf{H}_{a,b} e^{-j\beta_{a,b}z}, \tag{3.44}$$

into Eq.(3.40), we can obtain the general form of coupled mode equations:

$$\begin{cases} dA/dz \cdot e^{-j\beta_a z} + X_{ab} \cdot dB/dz \cdot e^{-j\beta_b z} = -j\kappa_{aa} \cdot Ae^{-j\beta_a z} - j\kappa_{ab} \cdot Be^{-j\beta_b z}, \\ dB/dz \cdot e^{-j\beta_b z} + X_{ab} \cdot dA/dz \cdot e^{-j\beta_a z} = -j\kappa_{ba} \cdot Ae^{-j\beta_a z} - j\kappa_{bb} \cdot Be^{-j\beta_b z}, \end{cases} \tag{3.45}$$

where X_{ab} and X_{ba} are two dimensionless **cross power ratios**:

$$X_{pq} \quad = \quad \frac{\int\int \hat{\mathbf{Z}} \cdot (\mathbf{E}_\mathbf{p}^* \times \mathbf{H}_\mathbf{q} + \mathbf{E}_\mathbf{q} \times \mathbf{H}_\mathbf{p}^*) dXdY}{\int\int \hat{\mathbf{Z}} \cdot (\mathbf{E}_\mathbf{p}^* \times \mathbf{H}_\mathbf{p} + \mathbf{E}_\mathbf{p} \times \mathbf{H}_\mathbf{p}^*) dXdY}, \quad p, q = a, b; \tag{3.46}$$

κ_{aa} and κ_{bb} are two **self-coupling terms**:

$$\kappa_{pp} \quad = \quad \frac{\omega\epsilon_0 \int\int \mathbf{E}_\mathbf{p}^* (\Delta\tilde{\epsilon}_h^q + \Delta\tilde{\epsilon}_h^{ptb}) \mathbf{E}_\mathbf{p} dXdY}{\int\int \hat{\mathbf{Z}} \cdot (\mathbf{E}_\mathbf{p}^* \times \mathbf{H}_\mathbf{p} + \mathbf{E}_\mathbf{p} \times \mathbf{H}_\mathbf{p}^*) dXdY}, \quad p = a, b; \tag{3.47}$$

κ_{ab} and κ_{ba} are two **cross-coupling terms** which quantify the coupling strength between the two modal fields:

$$\kappa_{pq} = \frac{\omega\epsilon_0 \int\int \mathbf{E}_\mathbf{p}^*(\Delta\tilde{\epsilon}_h^p + \Delta\tilde{\epsilon}_h^{ptb})\mathbf{E}_\mathbf{q} dXdY}{\int\int \hat{\mathbf{Z}} \cdot (\mathbf{E}_\mathbf{p}^* \times \mathbf{H}_\mathbf{p} + \mathbf{E}_\mathbf{p} \times \mathbf{H}_\mathbf{p}^*) dXdY}, \quad p, q = a, b. \tag{3.48}$$

We can see the coupled mode equations in the Helicoidal coordinates also have the same mathematical form that has been derived in the Cartesian coordinates as long as we keep in mind that the quantities here have their specific meaning with respect to covariant and contravariant dual space.

We can simplify the coupled mode equations as

$$\begin{cases} dA/dz = -j\kappa_{ab} \cdot Be^{-j(\beta_b - \beta_a)z}, \\ dB/dz = -j\kappa_{ba} \cdot Ae^{-j(\beta_a - \beta_b)z}, \end{cases} \tag{3.49}$$

where the new forms of propagation constants β_a and β_b take the substitutions:

$$\beta_a + \frac{\kappa_{aa} - \kappa_{ba}X_{ab}}{1 - X_{ab}X_{ba}} \to \beta_a, \quad \beta_b + \frac{\kappa_{bb} - \kappa_{ab}X_{ba}}{1 - X_{ab}X_{ba}} \to \beta_b, \tag{3.50}$$

and the new forms of coupling coefficients κ_{ab} and κ_{ba} take the substitutions:

$$\frac{\kappa_{ab} - \kappa_{bb}X_{ab}}{1 - X_{ab}X_{ba}} \to \kappa_{ab}, \quad \frac{\kappa_{ba} - \kappa_{aa}X_{ba}}{1 - X_{ab}X_{ba}} \to \kappa_{ba}. \tag{3.51}$$

This is a very simple form of ordinary differential equations, and its analytical solution is very well known. In later chapters, we will obtain the analytical solution of this two-mode coupling equations, which can be used to analyze the general designing approach of certain CCC fibers.

In some literature, there is another form of coupled mode equations which is completely equivalent but more convenient to see the physical meaning of each terms. We can put the harmonic longitudinal dependence $e^{-j\beta z}$ into the envelope function

$A(Z)$ and $B(Z)$

$$Ae^{-j\beta_a z} \to A, \quad Be^{-j\beta_b z} \to B. \tag{3.52}$$

Then, we can use this sort of "fast-varying" envelope to formulate the general form of coupled mode equations in another way:

$$\begin{pmatrix} 1 & X_{ab} \\ X_{ba} & 1 \end{pmatrix} \begin{pmatrix} dA/dZ \\ dB/dZ \end{pmatrix} = -j \begin{pmatrix} \beta_a + \kappa_{aa} & \kappa_{ab} + \beta_b X_{ab} \\ \kappa_{ba} + \beta_a X_{ba} & \beta_b + \kappa_{bb} \end{pmatrix} \begin{pmatrix} A \\ B \end{pmatrix}. \tag{3.53}$$

Here, we can see that the self-coupling terms κ_{aa} and κ_{bb} only contribute as additional corrections to the effective propagation constants as $[\beta_{a,b} + \kappa_{aa,bb}]$. Usually, the two coupling modes are supposed to be orthogonal or almost orthogonal, so the terms with X_{ab} and X_{ba} are commonly small enough to be neglected. Thus, the key of this coupling system relies on the cross-coupling terms κ_{ab} and κ_{ab}.

To evaluate the cross-coupling terms κ_{ab} and κ_{ab}, all we need to know are:

1. The perturbing permittivity tensors.
2. The eigenmode fields that get perturbed.

In the next section, we will focus on the permittivity of CCC structure, which is the first item. Then, we will analyze the eigenmode fields perturbed by different types of perturbing permittivity tensors, which is the second item.

3.2 CCC Permittivity and Structure in Cartesian Coordinates System and Helicoidal Coordinates System

3.2.1 Permittivity and Structure of CCC Fibers

Now, let's start illustrating the coordinates transformation procedure of CCC permittivity and structure. For a given CCC permittivity $\tilde{\epsilon}$, we first start with the expression in a fixed Cartesian cross-section $\{x_0, y_0, z_0\}$. In this cross-section, we have the CCC permittivity tensor $\tilde{\epsilon}$ expressed as a general form:

$$\tilde{\epsilon}_c(x_0, y_0, z = z_0) = \begin{pmatrix} \epsilon_1(x_0, y_0) & \epsilon_6(x_0, y_0) & \epsilon_5(x_0, y_0) \\ \epsilon_6(x_0, y_0) & \epsilon_2(x_0, y_0) & \epsilon_4(x_0, y_0) \\ \epsilon_5(x_0, y_0) & \epsilon_4(x_0, y_0) & \epsilon_3(x_0, y_0) \end{pmatrix}. \tag{3.54}$$

The reason to start with this expression is that, this general permittivity expression is a z-independent 2D expression, which will help deriving the permittivity tensor for the 3D rotating CCC structure in both Cartesian coordinates $\tilde{\epsilon}_c(x, y, z)$ and Helicoidal coordinates $\tilde{\epsilon}_h(X, Y, Z)$.

The transformation from 2D cross-section expression $\tilde{\epsilon}_c(x_0, y_0)$ to 3D Cartesian CCC rotating structure $\tilde{\epsilon}_c(x, y, z)$ is actually a rotation operation in terms of coordinates transformation, which is graphically shown in Figure 3.1. This rotation operation requires two steps:

1. Transform the tensor matrix $\tilde{\epsilon}$;
2. Rotate the scalar distribution function by making the substitution from $\{x_0, y_0, z_0\}$ to $\{x, y, z\}$.

It is very important to fulfill both of two operations.

Regarding the first step, we have the tensor matrix rotation transformation ac-

cording to the Jones matrix theory (*Yariv and Yeh*, 2003):

$$\tilde{\epsilon}_c(x_0, y_0) \rightarrow \mathbf{R_3^{-1}}(\tau z) \cdot \tilde{\epsilon}_{c_0}(x_0, y_0) \cdot \mathbf{R_3}(\tau z). \tag{3.55}$$

This is the new tensor form, but the scalar distribution functions $\epsilon_{1,2,3,4,5,6}$ of each components are still functions of $\{x_0, y_0\}$. Thus, we need to make the substitution from $\{x_0, y_0, z_0\}$ to $\{x, y, z\}$ to fulfill the second step:

$$\begin{pmatrix} x_0 \\ y_0 \\ z_0 \end{pmatrix} = \begin{pmatrix} x\cos\tau z + y\sin\tau z \\ -x\sin\tau z + y\cos\tau z \\ z \end{pmatrix} = \mathbf{R_3}(\tau z) \begin{pmatrix} x \\ y \\ z \end{pmatrix}. \tag{3.56}$$

Therefore, the 3D Cartesian CCC permittivity $\tilde{\epsilon}_c(x, y, z)$ can be expressed as:

$$\begin{aligned} \tilde{\epsilon}_c(x, y, z) &= \mathbf{R_3^{-1}}(\tau z) \cdot \tilde{\epsilon}_{c_0}(x_0, y_0) \cdot \mathbf{R_3}(\tau z), \\ &= \mathbf{R_3^{-1}}(\tau z) \cdot \tilde{\epsilon}_{c_0}(x\cos\tau z + y\sin\tau z, -x\sin\tau z + y\cos\tau z) \cdot \mathbf{R_3}(\tau z). \end{aligned} \tag{3.57}$$

Here, the 3D anti-clockwise rotation matrix $\mathbf{R_3}(\theta)$ and its inverse matrix $\mathbf{R_3^{-1}}(\theta) = \mathbf{R_3}(-\theta)$ as clockwise rotation are defined as

$$\mathbf{R_3}(\theta) = \begin{pmatrix} \mathbf{R}(\theta) & 0 \\ 0 & 1 \end{pmatrix}, \quad \mathbf{R_3}(-\theta) = \begin{pmatrix} \mathbf{R}(-\theta) & 0 \\ 0 & 1 \end{pmatrix}, \tag{3.58}$$

where $\mathbf{R}(\theta)$ and $\mathbf{R^{-1}}(\theta) = \mathbf{R}(-\theta)$ are the 2D anti-clockwise and clockwise rotation:

$$\mathbf{R}(\theta) = \begin{pmatrix} \cos\theta & \sin\theta \\ -\sin\theta & \cos\theta \end{pmatrix}, \quad \mathbf{R}(-\theta) = \begin{pmatrix} \cos\theta & -\sin\theta \\ \sin\theta & \cos\theta \end{pmatrix}. \tag{3.59}$$

The transformation from Cartesian CCC permittivity $\tilde{\epsilon}_c(x, y, z)$ to Helicoidal CCC

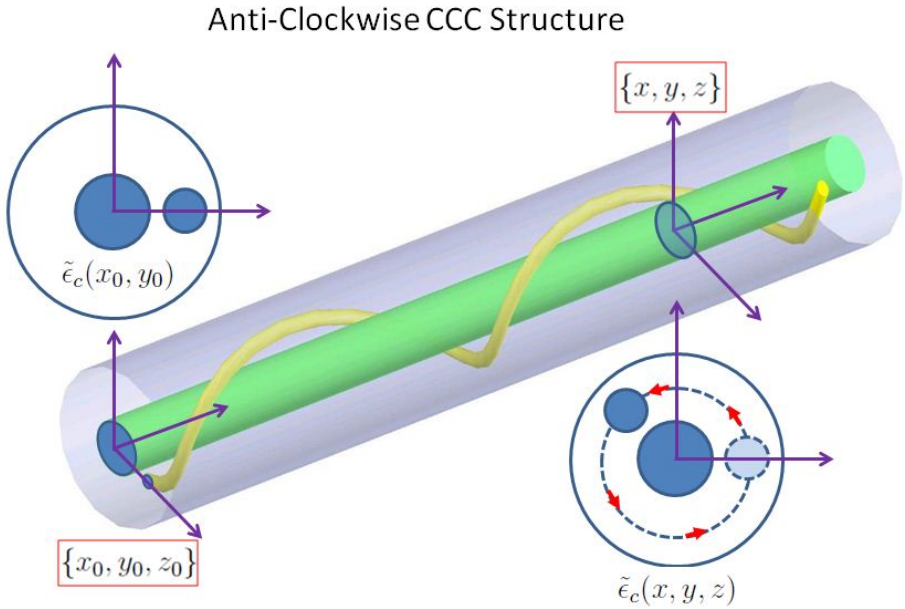

Figure 3.1: Anti-Clockwise CCC Structure: The 3D anti-clockwise CCC structure is generated by anti-clockwisely rotating the fixed $z = z_0$ 2D cross-section.

permittivity $\tilde{\epsilon}_h(X, Y, Z)$ also requires two operations — tensor matrix transformation following Eq.(3.30) and scalar distribution substitution following Eq.(3.4):

$$\begin{aligned} \tilde{\epsilon}_h(X, Y, Z) &= \mathbf{J^{-1}} \cdot \tilde{\epsilon}_c(x, y, z) \cdot (\mathbf{J^{-1}})^{\mathbf{T}}, \\ &= \mathbf{J^{-1}} \cdot \tilde{\epsilon}_c(X \cos \tau Z - Y \sin \tau Z, X \sin \tau Z + Y \cos \tau Z, Z) \cdot (\mathbf{J^{-1}})^{\mathbf{T}}, \end{aligned} \tag{3.60}$$

where the variables of scalar function are substituted from $\{x, y, z\}$ to $\{X, Y, Z\}$:

$$\begin{pmatrix} x \\ y \\ z \end{pmatrix} = \begin{pmatrix} X \cos \tau Z - Y \sin \tau Z \\ X \sin \tau Z + Y \cos \tau Z \\ Z \end{pmatrix} = \mathbf{R_3^{-1}}(\tau z) \begin{pmatrix} X \\ Y \\ Z \end{pmatrix}. \tag{3.61}$$

Therefore, using Eq.(3.57) and Eq.(3.60), we have the transformation from the 2D

cross-section expression $\tilde{\epsilon}_c(x_0, y_0)$ to 3D Helicoidal CCC permittivity $\tilde{\epsilon}_h(X, Y, Z)$:

$$\begin{aligned} \tilde{\epsilon}_h(X,Y,Z) &= \mathbf{J^{-1}} \cdot \mathbf{R_3^{-1}} \cdot \tilde{\epsilon}_c(x_0, y_0) \cdot \mathbf{R_3} \cdot (\mathbf{J^{-1}})^{\mathbf{T}}, \\ &= \mathbf{J^{-1}} \cdot \mathbf{R_3^{-1}} \cdot \tilde{\epsilon}_c(X, Y) \cdot \mathbf{R_3} \cdot (\mathbf{J^{-1}})^{\mathbf{T}}, \end{aligned} \tag{3.62}$$

where the substitution from $\{x_0, y_0, z_0\}$ to $\{X, Y, Z\}$ follows Eq.(3.56) and Eq.(3.61):

$$\begin{pmatrix} x_0 \\ y_0 \\ z_0 \end{pmatrix} = \mathbf{R_3}(\tau z) \cdot \left[\mathbf{R_3^{-1}}(\tau z) \cdot \begin{pmatrix} X \\ Y \\ Z \end{pmatrix} \right] = \begin{pmatrix} X \\ Y \\ Z \end{pmatrix}, \tag{3.63}$$

Here, we can rewrite the expression of Jacobian Matrix $\mathbf{J}$ in Eq.(3.21) as:

$$\mathbf{J} = \begin{pmatrix} \mathbf{R^{-1}}(\tau z) & \tau \mathbf{R^{-1}}(\tau z)\bar{\rho} \\ 0 & 1 \end{pmatrix}, \quad \bar{\rho} = \begin{pmatrix} -Y \\ X \end{pmatrix}. \tag{3.64}$$

With this compact form, we can write down $\mathbf{J^{-1}}$ and $(\mathbf{J^{-1}})^{\mathbf{T}}$ as:

$$\mathbf{J^{-1}} = \begin{pmatrix} \mathbf{R}(\tau z) & -\tau\bar{\rho} \\ 0 & 1 \end{pmatrix}, \quad (\mathbf{J^{-1}})^{\mathbf{T}} = \begin{pmatrix} \mathbf{R^{-1}}(\tau z) & 0 \\ -\tau\bar{\rho}' & 1 \end{pmatrix}, \tag{3.65}$$

which leads to two matrices on left and right of $\tilde{\epsilon}_c(X, Y)$ in Eq.(3.62) as:

$$\mathbf{T_L} = \mathbf{J^{-1}} \cdot \mathbf{R_3^{-1}} = \begin{pmatrix} \mathbf{I} & -\tau\bar{\rho} \\ 0 & 1 \end{pmatrix} = \begin{pmatrix} 1 & 0 & \tau Y \\ 0 & 1 & -\tau X \\ 0 & 0 & 1 \end{pmatrix}, \tag{3.66}$$

$$\mathbf{T_R} = \mathbf{R_3} \cdot (\mathbf{J^{-1}})^{\mathbf{T}} = \begin{pmatrix} \mathbf{I} & 0 \\ -\tau\bar{\rho}' & 1 \end{pmatrix} = \begin{pmatrix} 1 & 0 & 0 \\ 0 & 1 & 0 \\ \tau Y & -\tau X & 1 \end{pmatrix}. \tag{3.67}$$

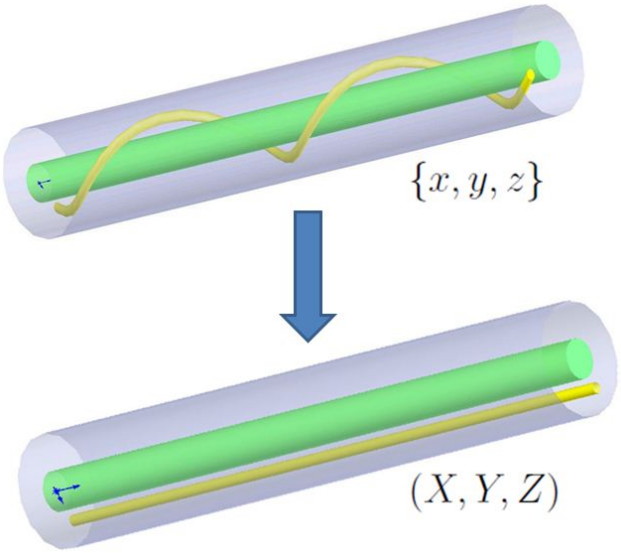

Figure 3.2: "Unwounded" CCC Structure: The CCC structure is "unwounded" by coordinates transformation. The CCC permittivity tensor in Helicoidal coordinates system is z-independent (Z-independent in Eq.(3.68)).

Then, due to the rule of associativity for matrix chain multiplication, we can finally express the general form of CCC permittivity in Helicoidal coordinates $\tilde{\epsilon}_h(X, Y, Z)$ by substituting Eq.(3.66), Eq.(3.66) and Eq.(3.54) into Eq.(3.62):

$$\begin{aligned}\tilde{\epsilon}_h(X, Y, Z) &= \mathbf{T_L} \cdot \tilde{\epsilon}_c(x_0, y_0) \cdot \mathbf{T_R} \\ &= \begin{pmatrix} 1 & 0 & \tau Y \\ 0 & 1 & -\tau X \\ 0 & 0 & 1 \end{pmatrix} \begin{pmatrix} \epsilon_1(X,Y) & \epsilon_6(X,Y) & \epsilon_5(X,Y) \\ \epsilon_6(X,Y) & \epsilon_2(X,Y) & \epsilon_4(X,Y) \\ \epsilon_5(X,Y) & \epsilon_4(X,Y) & \epsilon_3(X,Y) \end{pmatrix} \begin{pmatrix} 1 & 0 & 0 \\ 0 & 1 & 0 \\ \tau Y & -\tau X & 1 \end{pmatrix},\end{aligned} \tag{3.68}$$

which indeed shows that the CCC structure is "unwounded" by coordinates transformation, and the CCC permittivity tensor in the Helicoidal coordinates system is z-independent. We can see that, the cancelation of z-dependent rotation term τz in Eq,(3.62) comes from the fact that the rotation of distribution function and the rotation of coordinates basis are always opposite to each other.

3.2.2 Anisotropic Model of CCC Fibers

The ideal CCC fibers are made of amorphous fused silica, which means the ideal CCC fibers are supposed to be isotropic medium. However, the practically-made CCC fibers contain the strain-induced birefringence due to the manufacture process. These strain-induced birefringence are weak compared with the isotropic part, so we consider them as perturbations. We are going to build a model to analyze the anisotropic CCC structure, which includes two isotropic cores, one perturbation regions with linear and torsional birefringence, and a homogeneous isotropic cladding.

The linear birefringence will appear due to the cooling process when CCC fibers are drawn (*Yablon*, 2004). The refractive index differences between cladding, central core and side core are achieved by applying different doping concentration in the regions of central and side cores. The differences in doping concentration, in turn, induce the differences in thermal-expansion coefficients. Thus, during the cooling process of CCC fiber drawing, plane strain e_{xx}, e_{yy} and e_{xy} (also e_{yx}) will rise, which would cause linear birefringence terms $\Delta\epsilon_1$, $\Delta\epsilon_2$ and ϵ_6 to appear through photoelastic effect (*Tai and Rogowski*, 2002).

The torsional birefringence is caused by the rotation process during the CCC fibers fabrication. As known, fused silica fibers are drawn when the amorphous fiber preform is heated to a condition with a viscosity. The differences in doping concentration also cause the differences in viscosity coefficients. Hence, when the CCC fiber preform is rotating when it is drawn, different viscosity will induce shear strain e_{xz} and e_{zx}, and e_{yz} and e_{zy} (*Pietralunga et al.*, 2006; *Li et al.*, 2004), which would in turn cause torsional birefringence ϵ_4 and ϵ_5 to rise through photoelastic effect.

Since the plane strain terms are well-known and easily calculable physical quantities, we can calculate the distribution of plane strains in the cross section of the CCC fibers either analytically or numerically. We use FEM-based software called "COMSOL Multi-Physics" to simulate the cooling-induced linear strains . The distribution

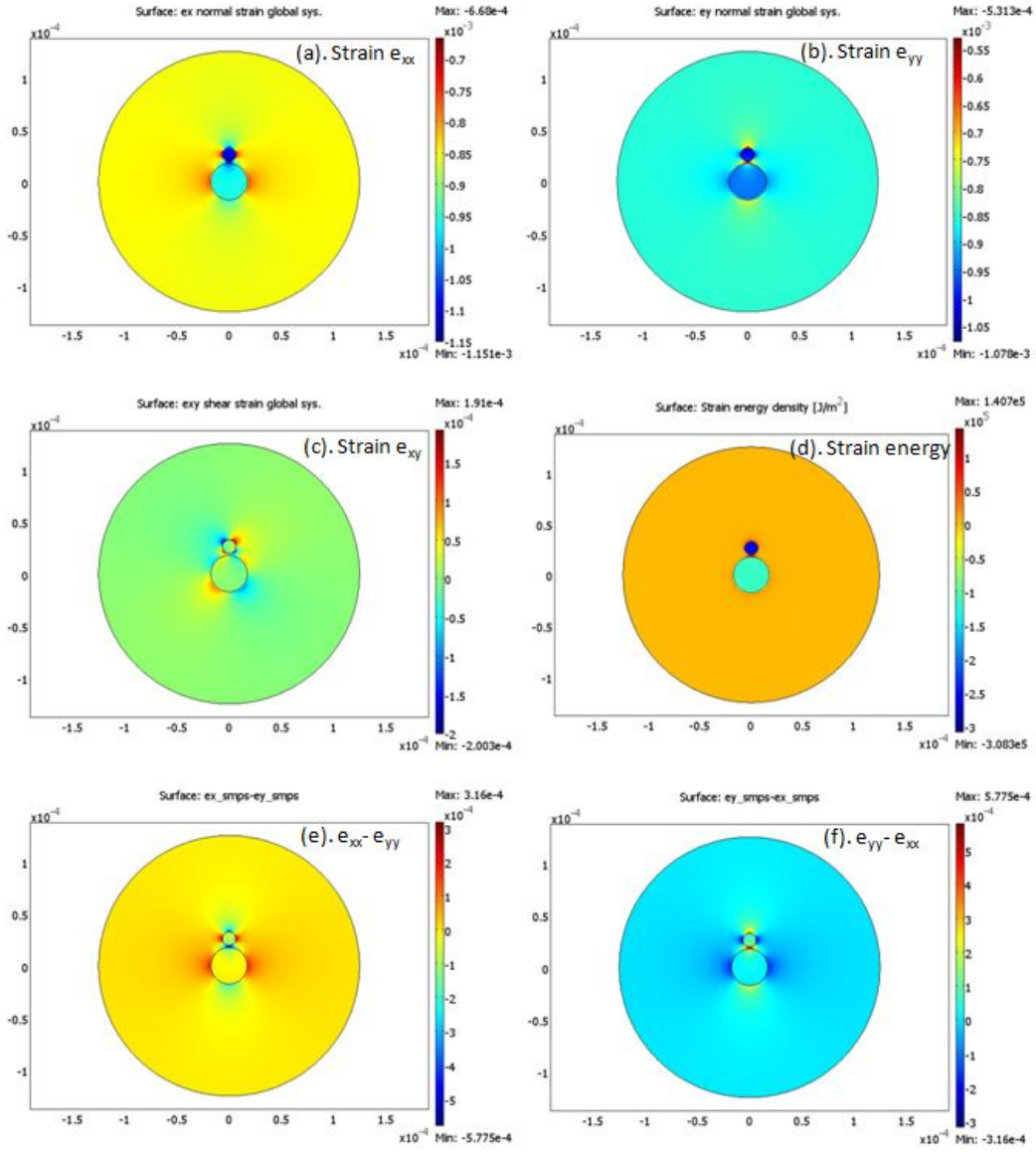

Figure 3.3: COMSOL-Calculated Strain Distribution in CCC Fiber Cross Section.

of e_{xx}, e_{yy} and e_{xy} are simulated and shown in Figure 3.3. In this figure, subplot (d) shows the strain energy distribution is a ring shape surrounding the two cores, while the orientation of this particular cross section gives different distributions of e_{xx}, e_{yy} and e_{xy} in (a), (b)and (c). Also from (d), we can see that the plane strain is more heavily distributed at the region between the two cores. This is because the doping concentration experiences the most dramatic change in this region, which in turn causes the most dramatic change in thermal-expansion coefficients.

The shear strains e_{xz} and e_{zx}, and e_{yz} and e_{zy} are not quantitatively calculable. However, we can legitimately assume these shear strain terms are also heavily distributed in the region between two cores, because it is supposed to have the most dramatic change in viscosity coefficients as well. In addition, the measurement doesn't show any sign of shear strain induced optical activity in the core, so it is also necessary to assume that the shear strain region is outside the cores.

It is possible to use the simulated strain distribution in Figure 3.3 to simulate the performance of practically-made CCC fibers. However, to continue with a less complicated physical model, we simplify the specific distribution of strains shown in Fig. 3.3 into a mathematically describable distribution of strains and strain-induced birefringence. Because both the linear and the torsional birefringence is heavily distributed at the region between two cores, and the more important point is we are mainly studying the coupling between two cores, it is physically reasonable and necessary to assume that the birefringence region is a single ellipse located between the two core, as shown in Figure 3.4.

Therefore, our anisotropic model of CCC fibers is based on the distribution on Figure 3.4, and there are totally 4 parts: a homogenous isotropic cladding ϵ_c^s, an isotropic cylindrically central-symmetric central core $\Delta\epsilon_c^a(x_0, y_0)$, an isotropic cylindrical side core $\Delta\epsilon_c^b(x_0, y_0)$, and an anisotropic ellipse region with a tensor perturbation $\Delta\tilde{\epsilon}_c^{ptb}(x_0, y_0)$. We can separate the expression of anisotropic CCC permittivity

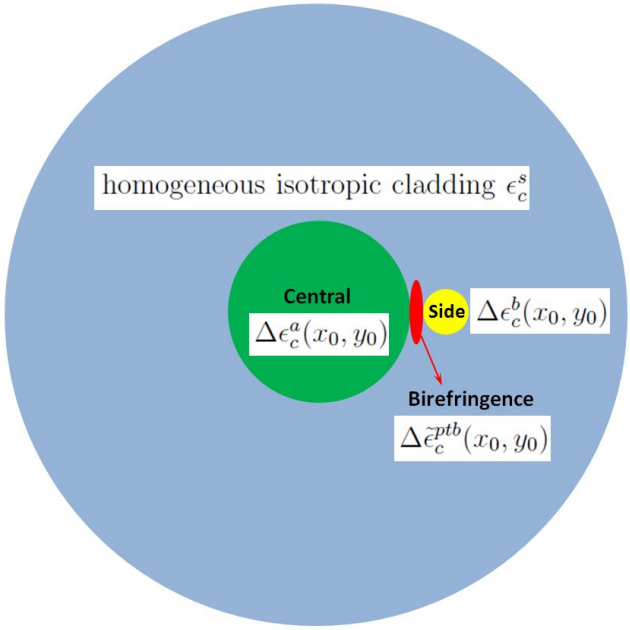

Figure 3.4: Simplified Perturbation Region for Anisotropic CCC Fibers.

into an isotropic part $\tilde{\epsilon}_c^{\text{Iso}}(x_0, y_0)$ and an anisotropic part $\Delta\tilde{\epsilon}_c^{ptb}(x_0, y_0)$:

$$\tilde{\epsilon}_c(x_0, y_0, z = z_0) \quad = \quad \tilde{\epsilon}_c^{\text{Iso}}(x_0, y_0) + \Delta\tilde{\epsilon}_c^{ptb}(x_0, y_0), \tag{3.69}$$

where the isotropic permittivity tensor $\tilde{\epsilon}_c^{\text{Iso}}(x_0, y_0)$ contains isotropic cladding ϵ_c^s, and two isotropic cores $\Delta\epsilon_c^a(x_0, y_0)$ and $\Delta\epsilon_c^b(x_0, y_0)$:

$$\tilde{\epsilon}_c^{\text{Iso}}(x_0, y_0) = \left[\epsilon_c^s + \Delta\epsilon_c^a(x_0, y_0) + \Delta\epsilon_c^b(x_0, y_0)\right] \cdot \mathbf{I}. \tag{3.70}$$

and the anisotropic perturbation tensor $\Delta\tilde{\epsilon}_c^{ptb}(x_0, y_0)$ contains linear birefringence $\Delta\tilde{\epsilon}_c^L(x_0, y_0)$ and torsional birefringence $\Delta\tilde{\epsilon}_c^T(x_0, y_0)$:

$$\Delta\tilde{\epsilon}_c^{ptb}(x_0, y_0) = \Delta\tilde{\epsilon}_c^L(x_0, y_0) + \Delta\tilde{\epsilon}_c^T(x_0, y_0). \tag{3.71}$$

In the following sections, we will separately investigate the linear birefringence $\Delta\tilde{\epsilon}_c^L(x_0, y_0)$ and torsional birefringence $\Delta\tilde{\epsilon}_c^T(x_0, y_0)$ in detail.

3.2.3 Linear Birefringence of Anisotropic CCC

The plane strain induced linear birefringence at $z = z_0$ cross section can be expressed as:

$$\Delta\tilde{\epsilon}_c^L(x_0, y_0, z = z_0) = \begin{pmatrix} \Delta\epsilon_1(x_0, y_0) & \epsilon_6(x_0, y_0) & 0 \\ \epsilon_6(x_0, y_0) & \Delta\epsilon_2(x_0, y_0) & 0 \\ 0 & 0 & 0 \end{pmatrix}. \tag{3.72}$$

From the plane strain simulation, we can see that, at certain cross section (shown in Figure 3.3c), $\epsilon_6(x_0, y_0)$ can be approximated to be zero between two cores, while $\Delta\epsilon_1(x_0, y_0)$ and $\Delta\epsilon_2(x_0, y_0)$ reach the peak values. Therefore, we can assume Eq.(3.72) is written in such a cross section, so $\epsilon_6(x_0, y_0) \approx 0$, and $\Delta\epsilon_1(x_0, y_0)$ and $\Delta\epsilon_2(x_0, y_0)$ are the peak values: $\Delta\epsilon_{1,2}(x_0, y_0) = -n_0^4 p_{11} e_{1,2}(x_0, y_0)$, where the plane strain distribution gives $e_1(x_0, y_0) = -e_2(x_0, y_0)$. Thus, the linear birefringence dn_l between the fast and slow axis is proportional to $|e_1 - e_2| = |e_{xx} - e_{yy}| = |e_{xx}| + |e_{yy}|$ (shown in Figure 3.3e and Figure 3.3f), and it would take the form

$$dn_l = -n_0^3 p_{11}[|e_{xx}(x_0, y_0)| + |e_{yy}(x_0, y_0)|], \tag{3.73}$$

for which we give it a moderate estimate to be 0.5×10^{-3}. Then, we can define the distribution function of linear birefringence $D(x_0, y_0)$ at $\{x_0, y_0\}$ cross section as

$$D(x_0, y_0) = n_0 \cdot dn_l(x_0, y_0) = \Delta\epsilon_1(x_0, y_0) = -\Delta\epsilon_2(x_0, y_0). \tag{3.74}$$

Hence, we have linear perturbation such a 2D cross section as

$$\Delta\tilde{\epsilon}_c^L(x_0, y_0) = \begin{pmatrix} D(x_0, y_0) & 0 & 0 \\ 0 & -D(x_0, y_0) & 0 \\ 0 & 0 & 0 \end{pmatrix}. \tag{3.75}$$

Substituting the Eq.(3.75) into Eq.(3.57) and using the substitution $(x_0, y_0) \rightarrow (x\cos\tau z + y\sin\tau z, -x\sin\tau z + y\cos\tau z)$, we have the 3D distribution of linear perturbation in Cartesian coordinates expressed as:

$$\Delta\tilde{\epsilon}_c^L(x,y,z) = \begin{pmatrix} D(x,y,z)\cdot\cos 2\tau z & D(x,y,z)\cdot\sin 2\tau z & 0 \\ D(x,y,z)\cdot\sin 2\tau z & -D(x,y,z)\cdot\cos 2\tau z & 0 \\ 0 & 0 & 0 \end{pmatrix}. \tag{3.76}$$

This means that the 3D distribution function of linear perturbation in Cartesian coordinates system is a z-dependent function $D(x, y, z)$. In addition, the tensor components become "double-helix" winding following the helical rotation(evolving as $\sin 2\tau z$ and $\cos 2\tau z$), which is consistent with the fact that this linear birefringence is along the radius vector. This is an very important conclusion regarding the physical picture of QPM conditions in CCC fibers within Cartesian coordinates. When we numerically simulate the optical waves propagation in CCC structure within the so called "laboratory" coordinates system (essentially Cartesian coordinates system), this double-helix winding is critical to understand the origin of QPM. Detailed discussion can be found in Chapter V.

Substituting the Eq.(3.75) into Eq.(3.68) and using substitution in Eq.(3.61), we have the linear perturbation in the Helicoidal coordinates:

$$\Delta\tilde{\epsilon}_h^L(X,Y,Z) = \begin{pmatrix} D(X,Y) & 0 & 0 \\ 0 & -D(X,Y) & 0 \\ 0 & 0 & 0 \end{pmatrix}. \tag{3.77}$$

This means both the amplitude distribution and the direction distribution of the linear birefringence are fixed in the Helicoidal coordinates, which are expected from the general analysis in Eq.(3.68). This is the form we are going to use for the CCC theoretical model in Helicoidal coordinates system.

3.2.4 Torsional Birefringence of Anisotropic CCC

For the torsional birefringence induced by the shear strain, the elasticity theory shows the shear strains as $e_5 = -\tau y$ and $e_4 = \tau x$ (*Timoshenko*, 1970), so photoelastic theory gives (*Ulrich and Simon*, 1979):

$$\begin{cases} \epsilon_5 = -n_0^4[\frac{1}{2}(p_{11} - p_{12})]e_5 = -n_0^4[\frac{1}{2}(p_{11} - p_{12})](-\tau y) = -\sigma\tau y, \\ \epsilon_4 = -n_0^4[\frac{1}{2}(p_{11} - p_{12})]e_4 = -n_0^4[\frac{1}{2}(p_{11} - p_{12})]\tau x = \sigma\tau x, \end{cases} \tag{3.78}$$

where we define torsional photoelastic constant σ as

$$\sigma = -n_0^4 \left[\frac{1}{2}(p_{11} - p_{12})\right]. \tag{3.79}$$

Then, we have the torsional birefringence in the fixed z_0 cross section

$$\Delta\tilde{\epsilon}_c^T(x_0, y_0) = \begin{pmatrix} 0 & 0 & -\sigma(x_0, y_0)\tau y_0 \\ 0 & 0 & \sigma(x_0, y_0)\tau x_0 \\ -\sigma(x_0, y_0)\tau y_0 & \sigma(x_0, y_0,)\tau x_0 & 0 \end{pmatrix}. \tag{3.80}$$

However, Eq.(3.80) is derived for a twisted rod with elasticity (*Timoshenko*, 1970), which applies for the case of twisting an optical fiber. Here, we have a different situation: a rod with viscosity (heated CCC fiber preform) is twisted, and the torsional strain is frozen into CCC fibers during the cooling process. Thus, the form of torsional birefringence is expected to be different from Eq.(3.80). Here, we assume the form of the torsional birefringence as

$$\Delta\tilde{\epsilon}_c^T(x_0, y_0, z) = \begin{pmatrix} 0 & 0 & -\sigma(x_0, y_0)\tau y' \\ 0 & 0 & \sigma(x_0, y_0)\tau x' \\ -\sigma(x_0, y_0)\tau y' & \sigma(x_0, y_0)\tau x' & 0 \end{pmatrix}, \tag{3.81}$$

where $x' = x_0 \cos\tau z - y_0 \sin\tau z$, $y' = x_0 \sin\tau z + y_0 \cos\tau z$. This assumption means that we still assume the same amplitude distribution function for torsional birefringence as $\sigma(x_0, y_0)$, but the direction of the torsional strain is different from the one in Eq.(3.80). Because the torsional strains induced by viscosity is not clear yet, we are not sure why it could take this form in Eq.(3.81) other than the one in Eq.(3.80) at this point, but we do know that the form in Eq.(3.81) leads us to the right conclusion.

Substituting Eq.(3.81) into Eq.(3.57), we can have the 3D torsional birefringence perturbation in the Cartesian coordinates as

$$\Delta\tilde{\epsilon}_c^T(x,y,z) = \tau\sigma(x,y,z) \begin{pmatrix} 0 & 0 & -y'' \\ 0 & 0 & x'' \\ -y'' & x'' & 0 \end{pmatrix}, \tag{3.82}$$

where $x'' = x\cos\tau z + y\sin\tau z$, $y'' = -x\sin\tau z + y\cos\tau z$. Comparing with the linear birefringence $\Delta\tilde{\epsilon}_c^L(x,y,z)$ in Eq.(3.76) which is double-helix winding and always parallel to the radius vector, we can see that the torsional birefringence perturbation $\Delta\tilde{\epsilon}_c^T(x,y,z)$ here is single-helix winding and always perpendicular to the radius vector.

Substituting Eq.(3.81) into Eq.(3.68), we can explicitly write down the torsional birefringence perturbation in the Helicoidal coordinates as

$$\Delta\tilde{\epsilon}_h^T(X,Y,Z) = \sigma(X,Y) \begin{pmatrix} -2\tau^2 Yy & \tau^2(Xy+xY) & -\tau y \\ \tau^2(Xy+xY) & -2\tau^2 Xx & \tau x \\ -\tau y & \tau x & 0 \end{pmatrix}, \tag{3.83}$$

where $x' = X\cos\tau Z - Y\sin\tau z$, $y' = X\sin\tau Z + Y\cos\tau Z$. This is the form we are going to use for the CCC theoretical model in the Helicoidal coordinates system.

3.3 Helical Modes and QPM Resonances

3.3.1 Helical Modes Inside Each Isotropic Core

By substituting Eq.(3.70) into Eq.(3.68) and using substitution $\{x_0 \to X, y_0 \to Y\}$, we can have the isotropic permittivity of CCC fibers in Helicoidal coordinates as

$$\tilde{\epsilon}_h^{\text{Iso}}(X,Y) \;=\; \left[\epsilon_c^s + \Delta\epsilon_h^a(X,Y) + \Delta\epsilon_h^b(X,Y)\right] \cdot \mathbf{T_L} \cdot \mathbf{T_R}. \tag{3.84}$$

Inside each isotropic core, we have the permittivity tensor expressed as

$$\tilde{\epsilon}_h^{\text{Core}}(X,Y,Z) \;=\; \left[\epsilon_c^s + \Delta\epsilon_c^{a,b}(X,Y)\right] \cdot \mathbf{T_L} \cdot \mathbf{T_R}. \tag{3.85}$$

We can separate this permittivity tensor into two parts

$$\tilde{\epsilon}_h^{\text{Core}}(X,Y) \;=\; \epsilon_h^{Str} + \Delta\tilde{\epsilon}_h^{Rot}, \tag{3.86}$$

where the scalar part ϵ_h^{Str} acts as a **straight** isotropic core:

$$\epsilon_h^{Str} \;=\; \epsilon_c^s + \Delta\epsilon_h^{a,b}(X,Y), \tag{3.87}$$

and the tensor part $\Delta\tilde{\epsilon}_h^{Rot}$ describes the **rotation effect** of CCC structure:

$$\begin{aligned}
\Delta\tilde{\epsilon}_h^{Rot} &= [\epsilon_h^s + \Delta\epsilon_h^{a,b}(X,Y)] \cdot \mathbf{T_L} \cdot \mathbf{T_R} \approx \epsilon_c^s \cdot \mathbf{T_L} \cdot \mathbf{T_R}, \\
&= \epsilon_c^s \begin{pmatrix} \tau^2 Y^2 & -\tau^2 XY & \tau Y \\ -\tau^2 XY & \tau^2 X^2 & -\tau X \\ \tau Y & -\tau X & 0 \end{pmatrix}.
\end{aligned} \tag{3.88}$$

This leads to an important fact that, the straight fiber static modes (carrying no angular momentum) inside each isotropic core are not eigenmodes anymore in the

Helicoidal coordinates system: an extra perturbation tensor term $\Delta\tilde{\epsilon}_h^{Rot}$ appears. The fundamental physics behind this conclusion is associated with the symmetry of Helicoidal coordinates system. Indeed, the symmetry of Helicoidal coordinates is a lower degree of symmetry compared with the traditional cylindrical symmetry in straight fibers. Thus, the straight fiber static modes carrying the cylindrical symmetry would not be the eigenmodes anymore.

To obtain the new fiber modes (as eigenmodes) inside each isotropic core in Helicoidal coordinates system, two approaches are used in this thesis: one is numerical, and another is analytical. The numerical approach is to rigorously solve the Maxwell equations for the eigenmodes with the permittivity tensor of each core $\tilde{\epsilon}_h^{\text{Core}}(X,Y)$ in Eq.(3.86). The analytical approach is to use the coupled mode theory to analytically solve for normal modes. The straight fiber static modes that are solved with the ϵ_h^{Str} can be considered as "zero-order" solutions. Then, the degenerate pairs of straight fiber static modes would be perturbed by $\Delta\tilde{\epsilon}_h^{Rot}$ and mixed into the new eigenmodes, which can be obtained by solving the coupled mode equations.

Due to the periodicity of CCC rotation structure, there might exist another modal solution that is to the analogy of Bloch modes in periodical structures. Since the analytical approach based on the coupled mode equations is actually giving a first order approximation solutions, the Bloch mode approach might provide a more exact modal solution in comparison. However, this Bloch mode approach would be more complicated considering the nature of its rotational periodicity instead of linear periodicity. Here, we just point out this approach for future analysis.

During the rest part of this section, we mainly focus on the analytical approach based on the coupled mode equations. It would give us the **helical modes** carrying orbital and spin optical angular momentums, and eventually lead us to the QPM conditions of CCC fibers. We will not discuss the numerical approach in details, but the numerical simulation results will be shown to confirm the results derived by the

analytical approach.

The general form of coupled mode equations in Helicoidal coordinates is presented in Eq.(3.53). For this particular problem — the coupling between a pair of two degenerate zero-order straight fiber static modes denoted by "o" and "e" inside either core "a" or core "b", we can rewrite the coupled mode equations as

$$\frac{d}{dz}\begin{pmatrix} A_o^{a,b} \\ A_e^{a,b} \end{pmatrix} = -j\begin{pmatrix} \beta_{a,b}+\kappa_{oo}^{a,b} & \kappa_{oe}^{a,b} \\ \kappa_{eo}^{a,b} & \beta_{a,b}+\kappa_{ee}^{a,b} \end{pmatrix}\begin{pmatrix} A_o^{a,b} \\ A_e^{a,b} \end{pmatrix}. \tag{3.89}$$

Here, the cross-power ratio X_{oe} and X_{eo} disappear for two degenerate orthogonal modal fields $\mathbf{E}^o$ and $\mathbf{E}^e$. The two self-coupling terms κ_{aa} and κ_{bb} are defined as

$$\kappa_{pp} = \frac{\omega\epsilon_0 \int\int \mathbf{E}_\mathbf{p}^* \Delta\tilde{\epsilon}_h^{Rot} \mathbf{E}_\mathbf{p} dXdY}{\int\int \hat{\mathbf{Z}} \cdot (\mathbf{E}_\mathbf{p}^* \times \mathbf{H}_\mathbf{p} + \mathbf{E}_\mathbf{p} \times \mathbf{H}_\mathbf{p}^*) dXdY}, \quad p = a, b. \tag{3.90}$$

Also, the two cross-coupling terms κ_{ab} and κ_{ba} are defined as:

$$\kappa_{pq} = \frac{\omega\epsilon_0 \int\int \mathbf{E}_\mathbf{p}^* \Delta\tilde{\epsilon}_h^{Rot} \mathbf{E}_\mathbf{q} dXdY}{\int\int \hat{\mathbf{Z}} \cdot (\mathbf{E}_\mathbf{p}^* \times \mathbf{H}_\mathbf{p} + \mathbf{E}_\mathbf{p} \times \mathbf{H}_\mathbf{p}^*) dXdY}, \quad p, q = a, b. \tag{3.91}$$

Pairs of two degenerate zero-order straight fiber modes are very well known as $\mathrm{HE}_{nx}^{o,e}(n = 1, 2, 3, ..., x = 1, 2, 3, ...)$ modal pairs and $\mathrm{EH}_{nx}^{o,e}(n = 2, 3, 4, ..., x = 1, 2, 3, ...)$ modal pairs, whose modal field expressions can be found in numerous textbooks and references. For convenience, we present their expressions in the appendix of this chapter.

Substituting the modal fields of a certain degenerate zero-order modal pair into Eq.(3.90) and Eq.(3.91), we can have two very interesting and important integration results after some algebra calculation.

First, the integration result of Eq.(3.90), regardless of which modal pair plugged in, always shows

$$\kappa_{ee}^{a,b} = \kappa_{oo}^{a,b} = \frac{\delta}{2}\tau^2 R_h^2 \beta_b, \tag{3.92}$$

where the symbol δ stands for:

$$\delta \quad = \quad \begin{cases} 0, \text{ on-axis core,} \\ 1, \text{ off-axis core,} \end{cases} \tag{3.93}$$

which means this term only exists for side core and vanishes for central core. This is very important in physics, because it means that the effective propagation constant of side core is lifted by the helical path, which has been intuitively pointed out:

$$\beta_b + \kappa^b_{ee,oo} = \beta_b(1 + \frac{1}{2}\tau^2 R_h^2) \approx \beta_b\sqrt{1 + \frac{1}{2}K^2 R_h^2} \to \beta_b, \tag{3.94}$$

where we have relation $\tau = K$.

Second, the integration result of Eq.(3.91), regardless of which modal pair plugged in, always shows

$$\kappa^{a,b}_{eo} = -\kappa^{a,b}_{oe} = -jn\tau = -jnK. \tag{3.95}$$

This is also a very important result. It shows that the two off-diagonal cross-coupling terms $\kappa^{a,b}_{eo}$ and $\kappa^{a,b}_{oe}$ are both pure imaginary quantities and mutually complex conjugate to each other, so they are analogous to the two optical activity terms in the coupled mode equations of two orthogonally linearly polarized modes, which means they would have the similar effect of optical activity. It turns out that these two terms are the ones associated with angular momentum, and we would see that they are responsible for the angular momentum associated new eigenmodes.

Then, with the substitution of Eq.(3.94) and Eq.(3.95), the coupled mode equations Eq.(3.89) becomes a coupling system with complex-conjugate off-diagonal terms

$$\frac{d}{dz}\begin{pmatrix} A^{a,b}_o \\ A^{a,b}_e \end{pmatrix} = -j\begin{pmatrix} \beta_{a,b} & jnK \\ -jnK & \beta_{a,b} \end{pmatrix}\begin{pmatrix} A^{a,b}_o \\ A^{a,b}_e \end{pmatrix}. \tag{3.96}$$

For this linear system, we can solve it as an eigenvalue problem to obtain the new eigenvector(eigenmodes) and eigenvalue(modal propagation constants):

$$\frac{d}{dz}\begin{pmatrix} A_o^{a,b} + jA_e^{a,b} \\ A_o^{a,b} - jA_e^{a,b} \end{pmatrix} = -j\begin{pmatrix} \beta_{a,b} + nK & 0 \\ 0 & \beta_{a,b} - nK \end{pmatrix}\begin{pmatrix} A_o^{a,b} + jA_e^{a,b} \\ A_o^{a,b} - jA_e^{a,b} \end{pmatrix}. \quad (3.97)$$

Therefore, we have found the eigenmodes for the CCC structure:

$$\mathbf{E}_{\pm} = \mathbf{E}_o \pm j\mathbf{E}_e, \quad (3.98)$$

with their new modal propagation constants as

$$\beta_{\pm} = \beta \pm nK, \quad (3.99)$$

which clearly shows the degeneracy breaking in the Helicoidal coordinates.

The new eigenmodes are the 90°-phase-shift combination of degenerate mode pair $\mathrm{HE}_{nx}^{o,e}(n \geq 1)$ or $\mathrm{EH}_{nx}^{o,e}(n \geq 2)$, or near-degenerate mode pair TE_{0x} and TM_{0x}. Here, we limit our discussion to weakly-guiding fibers, so the near-degenerate mode pair TE_{0x} and TM_{0x} can be approximated as degenerate mode pair and have the same modal-field expression of $\mathrm{EH}_{nx}^{o,e}(n = 0)$. We call these new eigenmodes as "Helical modes", and their general form of modal field takes:

$$\mathbf{E}_{nx}^{s} = s\begin{pmatrix} E_T\bar{S}_s \\ \gamma E_z \end{pmatrix} e^{-j(\beta+\gamma snK)z}, \quad (3.100)$$

where E_T and E_z are expressed as

$$E_T = \beta/u \cdot Z_{n-\gamma} \cdot e^{-j(\gamma sn-s)\theta}, \quad E_z = jZ_n \cdot e^{-j\gamma sn\theta}, \quad (3.101)$$

$\bar{S}_s$ and $s = \pm 1$ are the circular polarization ($\bar{S}_+$corresponds to LCP, and $\bar{S}_-$corresponds

to RCP) and its chiral sign (spin quantum number) of particular helical mode $\mathbf{E}_{nx}^{s}$:

$$\bar{S}_s = \begin{pmatrix} 1 \\ sj \end{pmatrix}, \tag{3.102}$$

and γ is the "type sign" depending on which type of helical modes:

$$\gamma = \begin{cases} +1, & \mathrm{HE}_{nx}^{\pm} = \mathrm{HE}_{nx}^{\mathrm{odd}} \pm j\mathrm{HE}_{nx}^{\mathrm{even}}, \quad n = 1, 2, 3, ... \\ -1, & \mathrm{EH}_{nx}^{\pm} = \mathrm{EH}_{nx}^{\mathrm{odd}} \mp j\mathrm{HE}_{nx}^{\mathrm{even}}, \quad n = 2, 3, 4, ... \\ -1, & \mathrm{EH}_{nx}^{\pm} = \mathrm{TE}_{0x}^{\mathrm{odd}} \mp j\mathrm{TM}_{0x}^{\mathrm{even}}, \quad n = 0. \end{cases} \tag{3.103}$$

For a certain pair of HE helical modes, namely $\mathrm{HE}_{nx}^{\pm} = \mathrm{HE}_{nx}^{\mathrm{odd}} \pm j\mathrm{HE}_{nx}^{\mathrm{even}}$, the phase term $e^{-j[\pm(n-1)]\theta}$ of E_T is carrying orbital-angular-momentum(OAM) of $\pm(n-1)\hbar$, and the term $e^{-j[\pm\theta]}$ of circular polarization $\bar{S}_{\pm}$ is carrying spin-angular-momentum(SAM) of $\pm\hbar$. The summation of OAM and SAM gives the total-angular-momentum(TAM) as $\pm n\hbar$, which is actually the physical reason why the helical modes $\mathrm{HE}_{nx}^{\pm}$ requires an extra increment of propagation constant $\Delta\beta = \pm nK$.

For a certain pair of EH helical modes, namely $\mathrm{EH}_{nx}^{\pm} = \mathrm{EH}_{nx}^{\mathrm{odd}} \mp j\mathrm{EH}_{nx}^{\mathrm{even}}$ including $\mathrm{TE}_{0x}^{\mathrm{odd}} \mp j\mathrm{TM}_{0x}^{\mathrm{even}}$, the phase term $e^{-j[\mp(n+1)]\theta}$ of E_T is carrying orbital-angular-momentum(OAM) of $\mp(n+1)\hbar$, and the term $e^{-j[\pm\theta]}$ of circular polarization $\bar{S}_{\pm}$ is carrying spin-angular-momentum(SAM) of $\pm\hbar$. So the summation of OAM and SAM gives the total-angular-momentum(TAM) as $\mp n\hbar$, which is also the physical reason why the helical modes $\mathrm{EH}_{nx}^{\pm}$ requires an extra increment of propagation constant $\Delta\beta = \mp nK$.

We can also notice that, for either HE or EH helical modes, the longitudinal modal field $s\gamma E_z e^{-j(\beta+\gamma snK)z}$ doesn't have SAM. Thus, the longitudinal modal field only has OAM, and TAM is equal to OAM. Physically, this is because the electric field of the longitudinal modal field is always pointing at the same direction as the propagation direction, so it would not have a circular polarization nor even a linear polarization

at all. However, we can see that it is still consistent to have TAM equal to $\pm n\hbar$ and $\mp n\hbar$ for HE and EH helical modes respectively.

By combining the degenerate or near-degenerate straight fiber modes into so called "LP-modes"(modal groups), we can summarize the helical modes in $\mathrm{LP}_{|l|x}$ group as

$$\mathbf{E}^{\mathrm{LP}}_{|l|x} = s \begin{pmatrix} \beta/u \cdot Z_{|l|} e^{-jl\theta} \cdot \bar{S}_s \\ \gamma \cdot jZ_{|l+s|} e^{-j(l+s)\theta} \end{pmatrix} e^{-j(\beta+lK+sK)z}, \tag{3.104}$$

where the $|l|$ is the mode order of $\mathrm{LP}_{|l|x}$ mode and the $l = \pm|l|$ is the orbital quantum number, $s = \pm 1$ and $\gamma = \pm 1$ remain their meaning, and γ actually takes the sign of $(|l+s| - |l|)$.

Here, we need to clarify the relation between LP-modes and vector modes (HE modes, EH modes, TE and TM modes). In optics and even fiber-optics community, people are more familiar with LP-modes, which is derived by assuming the modal electric fields are linearly polarized all over the fiber cross-section in cylindrical symmetry. However, the assumption of linearly polarized modal fields would never fulfill the boundary condition of cylindrical symmetry for Maxwell equation, so LP-modes are actually approximated modal solutions. In fact, only the longitudinal field component $\mathbf{E_z}$ of the modal fields can fulfill the cylindrical symmetry, so we can solve for $\mathbf{E_z}$ first and use relation between $\mathbf{E_z}$ and $\mathbf{E_{x,y}}$ in Maxwell equation to obtain the whole modal solution. Following this procedure, we have the solution of vector modes which contains HE modes, EH modes, TE and TM modes. When the fiber is approaching "weakly guiding limit", a group of vector modes will have approximately the same propagation constants, and they can combine together to render the LP-modes. Thus, the vector modes are the true eigenmodes of Maxwell equation in cylindrical fibers, and the LP-modes are just the superposition of different vector modes. We can also consider LP-modes as modal groups which contain several different vector modes with degenerate or near-degenerate modal propagation constants.

Table 3.1: LP Helical Modes with SAM and OAM

	$\|l\|$	Modes	l	s	$m = l + s$	$\Delta\beta_{OAM+SAM} = mKz$
$\mathrm{LP}_{\|l\|x}$	$\|l\| = 0$	$\mathrm{HE}^{+}_{1,x}$	0	$+1$	1	Kz
		$\mathrm{HE}^{-}_{1,x}$	0	-1	-1	$-Kz$
	$\|l\| = 1$	$\mathrm{HE}^{+}_{2,x}$	$+1$	$+1$	2	$2Kz$
		$\mathrm{TE}_{0,x}$	$0(+1)$	$0(-1)$	0	0
		$\mathrm{TM}_{0,x}$	$0(-1)$	$0(-1)$	0	0
		$\mathrm{HE}^{-}_{2,x}$	-1	-1	-2	$-2Kz$
	$\|l\| \geq 2$	$\mathrm{HE}^{+}_{l+1,x}$	$+l$	$+1$	$l+1$	$(l+1)Kz$
		$\mathrm{EH}^{-}_{l-1,x}$	$+l$	-1	$l-1$	$(l-1)Kz$
		$\mathrm{EH}^{+}_{l-1,x}$	$-l$	$+1$	$-(l-1)$	$-(l-1)Kz$
		$\mathrm{HE}^{-}_{l+1,x}$	$-l$	-1	$-(l+1)$	$-(l+1)Kz$

By defining the total quantum number $m = (l + s)$, we can summarize LP-modes and vector modes in Table 3.1. In this table, we can see it shows a strong analogy to the angular momentum of electrons in quantum mechanics. We know that the microscopic photon is also a quantum particle, so here comes a very interesting question: should macroscopic laser beam exhibit the same angular momentum effect in quantum mechanics? If we consider the coherent laser beam as a giant Bose-Einstein Condensation(BEC) of photons, then the laser beam should also exhibit the quantum effect as well. In this table, we can see that it basically follows the rule of $m = l+s$, and l and s should take any value available. From this table we can also see that, the modal order $|l|$ for a $\mathrm{LP}_{|l|x}$ mode is the absolute value of its orbital quantum number. Also, the modal order n for a vector mode (e.g. $\mathrm{HE}^{\pm}_{nx}$) is the absolute value of its angular quantum number $m = \pm n$. Hence, for a given vector mode we can easily know its corresponding propagation constant increment $\Delta\beta_{OAM+SAM} = mKz$.

We have also rigorously confirmed our derived helical modes by solving the modal fields in the helical reference frame with Finite-Element-Method(FEM) (*Nicolet et al.*,

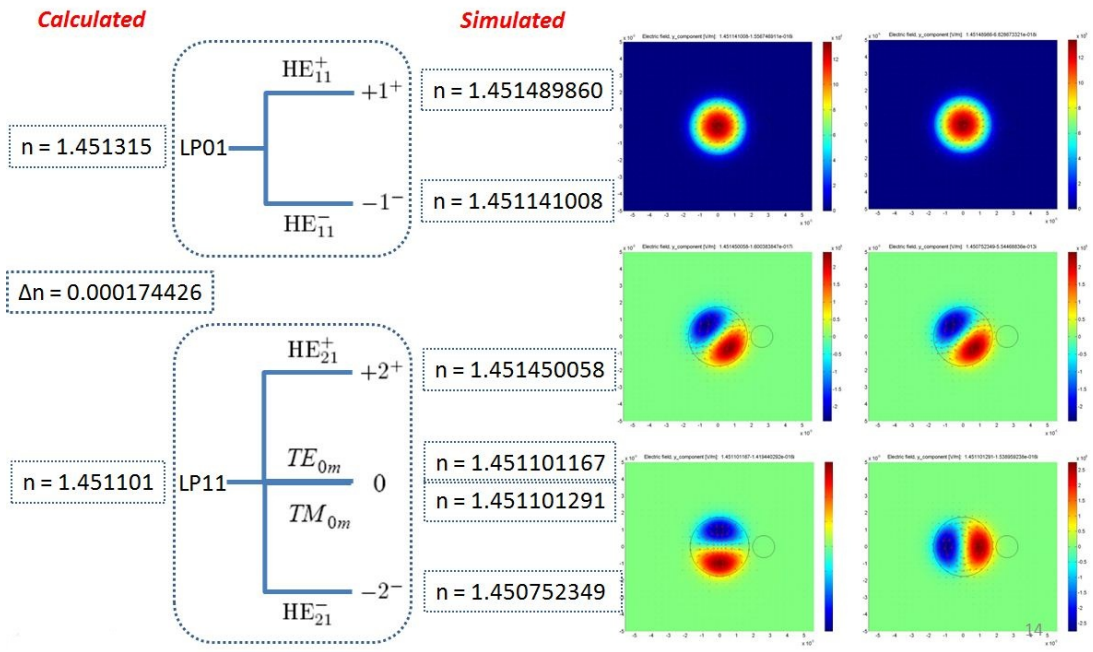

Figure 3.5: FEM Simulated Helical Modes in Helical Reference Frame.

2004). In Fig. 3.5, the left column of the refractive index are the calculated number for the modal effective refractive index in the Cartesian reference frame, while the right column of the refractive index are the simulated number. It clearly shows the degeneracy breaking in the helical reference frame. The propagation constant increments also fit the derived expression from the theory $\Delta\beta_{OAM+SAM} = mKz$.

3.3.2 Central-Side Coupling of Vector Helical Modes

Now, we can treat helical modes as unperturbed zero-order solutions, and substitute the modal expression of helical modes of both central and side core into the coupled mode equation Eq.(3.53) to solve the phase matching conditions for the central-side helical-modes coupling. In this subsection, we will use the modal expression in Eq.(3.100) for vector helical modes, and derive the phase matching conditions for two LP groups from central and side core (central LP_{01} and side LP_{21}). We will see that, however, it is rather complicated and tedious to illustrate QPM conditions with vector helical mode. In the next subsection, we will find out that

it is rather straightforward to use the modal expression Eq.(3.104) for LP groups of helical modes to derive the qausi-phase-matching conditions, which leads to the proof of QPM formula in Eq.(2.9) and Eq.(2.10).

Based on the analysis following Eq.(3.53), we know that the phase matching condition in this central-side coupling system only relies on the cross-coupling terms in Eq.(3.48). Furthermore, we can see that the key to determine the cross-coupling terms expressed in Eq.(3.48) is the interaction function I_{pq}, which is essentially the part to be integrated in the numerator integral of Eq.(3.48):

$$I_{pq} = \mathbf{E}_{\mathbf{p}}^{*}(\Delta\tilde{\epsilon}_h^p + \Delta\tilde{\epsilon}_h^{ptb})\mathbf{E}_{\mathbf{q}}, \quad p, q = a, b, \tag{3.105}$$

where a and b are specifically referring to central core "a" and side core "b". Obviously, the phase matching of this coupling system is determined as the condition when the propagation phase of interaction function I_{pq} is equal to zero:

$$\text{Phase}\{I_{pq}\} \equiv 0. \tag{3.106}$$

We can rewrite the permittivity tensor in Eq.(3.105) as

$$\Delta\tilde{\epsilon}_h^p + \Delta\tilde{\epsilon}_h^{ptb} = \Delta\tilde{\epsilon}_h^S + \Delta\tilde{\epsilon}_h^L + \Delta\tilde{\epsilon}_h^T. \tag{3.107}$$

Here the scalar perturbation $\Delta\tilde{\epsilon}_h^S$ comes from another isotropic core

$$\Delta\tilde{\epsilon}_h^S = \Delta\epsilon_h^p \begin{pmatrix} 1+\tau^2Y^2 & -\tau^2XY & \tau Y \\ -\tau^2XY & 1+\tau^2X^2 & -\tau X \\ \tau Y & -\tau X & 1 \end{pmatrix} \approx \Delta\epsilon_h^p, \tag{3.108}$$

where the rotation of this isotropic core is neglected, because it is an even smaller effect than the scalar perturbation of this isotropic core itself. By substituting Eq.(3.107)

into Eq.(3.105), we have interaction function separated into three parts:

$$I_{pq} = I_{pq}^{S} + I_{pq}^{L} + I_{pq}^{T}, \tag{3.109}$$

where the scalar interaction I_{pq}^{S}, the linear interaction I_{pq}^{S}, and the torsional interaction I_{pq}^{S} are defined respectively as:

$$I_{pq}^{S} = \mathbf{E}_{\mathbf{p}}^{*} \Delta\tilde{\epsilon}_{h}^{S} \mathbf{E}_{\mathbf{q}}, \quad I_{pq}^{L} = \mathbf{E}_{\mathbf{p}}^{*} \Delta\tilde{\epsilon}_{h}^{L} \mathbf{E}_{\mathbf{q}}, \quad I_{pq}^{T} = \mathbf{E}_{\mathbf{p}}^{*} \Delta\tilde{\epsilon}_{h}^{T} \mathbf{E}_{\mathbf{q}}, \tag{3.110}$$

Regarding the scalar interaction I_{pq}^{S}, we can substitute Eq.(3.108) and Eq.(3.100) to obtain its expression. By keeping the largest term with $E_T^{p*} E_T^{q}$ and neglecting other smaller terms with $E_T^{p*} E_z^{q}$, $E_z^{p*} E_T^{q}$ or $E_z^{p*} E_z^{q}$, we have

$$I_{pq}^{S} \approx s_p s_q E_T^{p*} E_T^{q} (1 + s_p s_q) \cdot \Delta\epsilon_h^{p} \cdot e^{-j(\beta_q - \beta_p)z} e^{-j(\gamma_q s_q n_q - \gamma_p s_p n_p)Kz}, \tag{3.111}$$

which requires $s_p = s_q$ to obtain non-zero value of scalar interaction I_{pq}^{S}:

$$I_{pq}^{S} \approx \begin{cases} 2E_T^{p*} E_T^{q} \Delta\epsilon_h^{p} e^{-j(\beta_q - \beta_p)z} e^{-j(\gamma_q n_q - \gamma_p n_p)Kz}, & s_p = s_q, \\ 0, & s_p \neq s_q. \end{cases} \tag{3.112}$$

Therefore, the QPM conditions for scalar interactions are

$$\Delta m = \gamma_q n_q - \gamma_p n_p, \quad s_p = s_q. \tag{3.113}$$

Taking the helical modes in LP_{01}^{p} group and LP_{21}^{q} group for example, we have the following QPM conditions:

$$\begin{cases} \Delta m = +2, \quad \mathrm{HE}_{11}^{+} \bigoplus \mathrm{HE}_{31}^{+}; \quad \Delta m = -2, \quad \mathrm{HE}_{11}^{-} \bigoplus \mathrm{HE}_{31}^{-}; \\ \Delta m = +2, \quad \mathrm{HE}_{11}^{-} \bigoplus \mathrm{EH}_{31}^{-}; \quad \Delta m = -2, \quad \mathrm{HE}_{11}^{+} \bigoplus \mathrm{EH}_{31}^{+}, \end{cases} \tag{3.114}$$

where "$\bigoplus$" means interaction between the two modes. We can see that the scalar interaction term I_{pq}^{S} comes from the interaction between modal fields with the same circularly polarization. Since the two modal fields interact in the way as if they interact with each other with only scalar modal functions, we can call these QPM resonances as scalar resonances.

Regarding the linear interaction I_{pq}^{L}, we can use Eq.(3.77) and Eq.(3.100) to obtain its expression. Similarly, by keeping the largest term with $E_T^{p*}E_T^{q}$ and neglecting other smaller terms with $E_T^{p*}E_z^{q}$, $E_z^{p*}E_T^{q}$ or $E_z^{p*}E_z^{q}$, we have

$$I_{pq}^{L} \approx s_p s_q E_T^{p*} E_T^{q} (1 - s_p s_q) \cdot D(X,Y) \cdot e^{-j(\beta_q - \beta_p)z} e^{-j(\gamma_q s_q n_q - \gamma_p s_p n_p)Kz}, \tag{3.115}$$

which requires $s_p \neq s_q$ to obtain non-zero value of scalar interaction I_{pq}^{L}:

$$I_{pq}^{L} \approx \begin{cases} 2E_T^{p*} E_T^{q} \Delta\epsilon_h^{p} e^{-j(\beta_q - \beta_p)z} e^{-j(\gamma_q n_q - \gamma_p n_p)Kz}, & s_p \neq s_q, \\ 0, & s_p = s_q. \end{cases} \tag{3.116}$$

Then, the QPM conditions for linear interactions are

$$\Delta m = \gamma_q n_q - \gamma_p n_p, \quad s_p \neq s_q. \tag{3.117}$$

Again, taking LP_{01}^{p} group and LP_{21}^{q} group for example, we have the following QPM conditions for linear interactions:

$$\begin{cases} \Delta m = +4, & \mathrm{HE}_{11}^{-} \bigoplus \mathrm{HE}_{31}^{+}; \quad \Delta m = -4, \quad \mathrm{HE}_{11}^{+} \bigoplus \mathrm{HE}_{31}^{-}; \\ \Delta m = 0\ , & \mathrm{HE}_{11}^{-} \bigoplus \mathrm{EH}_{31}^{+}; \quad \Delta m = 0\ , \quad \mathrm{HE}_{11}^{+} \bigoplus \mathrm{EH}_{31}^{-}. \end{cases} \tag{3.118}$$

We can see that the linear interaction term I_{pq}^{L} comes from the interaction between two orthogonal circularly polarized modal fields. The physics behind this is that, the linear birefringence couples two orthogonal circularly polarized fields. So we can call

these QPM resonances as linear birefringence resonances.

Regarding the torsional interaction I_{pq}^{T}, we can use Eq.(3.83), Eq.(3.100) to obtain its expression by neglecting the smallest term with $E_z^{p*}E_z^q$. Since the expression of I_{pq}^{T} is much more complicated than the previous two scenarios, it is more convenient to separate I_{pq}^{T} into three terms:

$$I_{pq}^{T} = I_{pq}^{tt} + I_{pq}^{tz} + I_{pq}^{zt},$$

where I_{pq}^{tt} contains the transverse-transverse coupling term $E_T^{p*}E_T^q$, I_{pq}^{tz} contains the transverse-longitudinal coupling term $E_T^{p*}E_z^q$, and I_{pq}^{zt} contains the longitudinal-transverse coupling term $E_z^{p*}E_T^q$. For transverse-transverse coupling term I_{pq}^{tt}, we have

$$\begin{aligned} I_{pq}^{tt} &= -s_p s_q \sigma\tau^2 E_T^{p*}E_T^q \cdot e^{-j(\beta_q-\beta_p)z} e^{-j(\gamma_q s_q n_q - \gamma_p s_p n_p)Kz} \cdot \\ &\quad \left\{(1+s_p s_q)(X^2+Y^2)\left[e^{-j(-\tau z)} + e^{-j(\tau z)}\right]/2 \right. \\ &\quad \left. +2(s_q - s_p)[(Y^2-X^2)(s_q-s_p)/4 - jXY]e^{-j(s_p-s_q)\tau z/2}\right\}, \end{aligned} \quad (3.119)$$

which leads to the phase term

$$\text{Phase}\{I_{pq}^{tt}\} = \begin{cases} e^{-j(\beta_q-\beta_p)z} e^{-j(\gamma_q s_q n_q - \gamma_p s_p n_p)Kz} \cdot \left[e^{j\tau z} + e^{-j\tau z}\right], & s_p = s_q, \\ e^{-j(\beta_q-\beta_p)z} e^{-j(\gamma_q s_q n_q - \gamma_p s_p n_p)Kz} \cdot e^{-j(s_p-s_q)\tau z/2}, & s_p \neq s_q. \end{cases} \quad (3.120)$$

By taking the helical modes in LP_{01}^{p} and LP_{21}^{q} group for example, we can summarize the QPM conditions as: no matter the circular polarizations of the two interacting modal fields are orthogonal or the same, this term always gives

$$\Delta m = \pm 3, \pm 1. \quad (3.121)$$

For the other two terms I_{pq}^{tz} and I_{pq}^{zt}, since both of these two terms are the interactions between one transverse field from one mode and one longitudinal field from another

mode, we can put them together and have the expression:

$$I_{pq}^{tz} + I_{pq}^{zt} = -s_p s_q \sigma\tau \cdot e^{-j(\beta_q - \beta_p)z} e^{-j(\gamma_q s_q n_q - \gamma_p s_p n_p)Kz} \cdot \left[\gamma_q E_T^{p*} E_z^q (Y + j s_p X) e^{-s_p \tau z} + \gamma_p E_z^{p*} E_T^q (Y - j s_p X) e^{j s_q \tau z}\right]. \quad (3.122)$$

Going through the same procedures, we will find out that these two terms render the same QPM conditions for the helical modes in LP_{01}^p group and LP_{21}^q group:

$$\Delta m = \pm 3, \pm 1. \quad (3.123)$$

Thus, all three terms in torsional interaction term I_{pq}^T give the same conclusion, and they all come from the physical consequence of torsional birefringence which couples one transverse field and one longitudinal field. We can call these QPM resonances as torsional birefringence resonances.

Combining the analysis of the three individual parts I_{pq}^S, I_{pq}^L and I_{pq}^T, we can summarize the QPM conditions for the interaction between LP_{01}^p group and LP_{21}^q group as $\Delta m = -4, -3, -2, -1, 0, +1, +2, +3, +4$, in which ± 2 are scalar resonances, $0, \pm 4$ are linear birefringence resonances, and $\pm 1, \pm 3$ are torsional birefringence resonances. Furthermore, given any arbitrary two helical modes inside central and side core, we can use the above analyzing procedure to find out their QPM conditions. However, as has been pointed out, it is rather tedious to use vector helical mode expression in Eq.(3.100) to derive the QPM conditions. There is a much more straightforward way to do it, which is illustrated in the next subsection.

3.3.3 Central-Side Coupling of LP-Modes and QPM Formula

For $\mathrm{LP}_{|l_p|x_p}^p$ group and $\mathrm{LP}_{|l_q|x_q}^q$ group, it would be more convenient and intuitive to directly use LP-modes expression in Eq.(3.104) instead of modal expression for each vector helical modes expression Eq.(3.100) inside each LP group. For further

convenience, we can express the propagation phase of interaction function I_{pq} as the product of a propagation constant phase mismatch $\Delta\beta$ and propagation distance z:

$$\text{Phase}\{I_{pq}\} = \text{Phase}\{\kappa_{pq}\} = \Delta\beta z, \tag{3.124}$$

Thus, we can have a more convenient definition for phase matching condition as

$$\Delta\beta \equiv 0, \tag{3.125}$$

which is equivalent to Eq.(3.106).

By substituting the LP-modes expression Eq.(3.104) into coupled mode equation and cross-coupling terms, we can have the three parts I_{pq}^S, I_{pq}^L and I_{pq}^T of interaction function one by one. For scalar interaction I_{pq}^S, we have

$$I_{pq}^S \propto (1 + s_p s_q) \cdot e^{-j[\beta_q - \beta_p + (l_q - l_p + s_q - s_p)K]z}. \tag{3.126}$$

For linear interaction I_{pq}^L, we have

$$I_{pq}^L \propto (1 - s_p s_q) \cdot e^{-j[\beta_q - \beta_p + (l_q - l_p + s_q - s_p)K]z}, \tag{3.127}$$

For the torsional interaction I_{pq}^T, we have to separate the discussion into three terms:

1. The transverse-transverse term I_{pq}^{tt} gives

$$I_{pq}^{tt} \propto \begin{cases} [e^{-jKz} + e^{jKz}] \cdot e^{-j[\beta_q - \beta_p + (l_q - l_p)K]z}, \ s_p = s_q, \\ e^{-j[\beta_q - \beta_p + (l_q - l_p + s_q)K]z}, \ s_p \to -s_q, \\ e^{-j[\beta_q - \beta_p + (l_q - l_p - s_p)K]z}, \ s_q \to -s_p, \end{cases} \tag{3.128}$$

2. The transverse-longitudinal term I_{pq}^{tz} gives

$$I_{pq}^{tz} \propto e^{-js_pKz} \cdot e^{-j[\beta_q-\beta_p+(l_q-l_p+s_q-s_p)K]z}, \tag{3.129}$$

3. The longitudinal-transverse term I_{pq}^{zt} gives

$$I_{pq}^{zt} \propto e^{-j(-s_q)Kz} \cdot e^{-j[\beta_q-\beta_p+(l_q-l_p+s_q-s_p)K]z}. \tag{3.130}$$

Thus, we can summarize the general expression for torsional interaction I_{pq}^{T} as

$$I_{pq}^{T} \propto e^{-j[\beta_q-\beta_p+(l_q-l_p+s_{p,q})K]z}, \tag{3.131}$$

Then, from Eq.(3.126), Eq.(3.127) and Eq.(3.131), we can see that, for all three cases we can have a general expression for phase-matching condition following Eq.(3.125):

$$\Delta\beta = \beta_q - \beta_p + \Delta mK = 0. \tag{3.132}$$

where the so called QPM number Δm (from Chapter II) follows:

$$\Delta m = \Delta l + \Delta s, \tag{3.133}$$

with $\Delta l = l_q - l_p$ and $\Delta s = s_q - s_p$ (except for torsional interaction we have $\Delta s = s_{p,q}$). The orbital quantum number renders $l_{p,q} = \pm|l_{p,q}|$, which we have always known, so Δl would take all possible number of $\{\pm|l_q| \pm |l_p|\}$. The spin quantum number renders $s_{p,q} = \pm 1$, so Δs would take all possible number of $\{0, \pm 1, \pm 2\}$. In fact, this is how Eq.(2.9) and Eq.(2.10) come from.

Also from Eq.(3.126), Eq.(3.127) and Eq.(3.131), we can obtain the correspondence between the interaction type and the value of Δs:

1. Scalar Perturbation: $\Delta s = 0$.

2. Linear Perturbation: $\Delta s = \pm 2$.

3. Torsional Perturbation: $\Delta s = \pm 1$.

Thus, we can identify the interaction type of a certain QPM resonance by identifying the number of Δs.

If taking $q = a$ as central core and $p = b$ as side core, and counting the side core correction fact $\sqrt{1 + K^2 R_h^2}$, we can conclude the QPM conditions for $\mathrm{LP}^a_{|l_a|x_a}$ modal group and $\mathrm{LP}^b_{|l_b|x_b}$ modal group as:

$$\Delta\beta = \beta_a - \beta_b \sqrt{1 + K^2 R_h^2} + \Delta m K = 0, \tag{3.134}$$

where we have

$$\Delta m = \Delta l + \Delta s, \quad \Delta l = \pm|l_a| \pm |l_b|, \quad \Delta s = 0, \pm 1, \pm 2. \tag{3.135}$$

Therefore, we have proven the QPM formula for anisotropic CCC fibers.

Appendix

HE and EH modes are expressed as

$$\mathrm{HE}^{\mathrm{odd}} = \begin{pmatrix} j\beta/uZ_{n-1}[-\sin(n-1)\theta] \\ j\beta/uZ_{n-1}[-\cos(n-1)\theta] \\ Z_n \sin n\theta \end{pmatrix}, \quad \mathrm{HE}^{\mathrm{even}} = \begin{pmatrix} j\beta/uZ_{n-1}[-\cos(n-1)\theta] \\ j\beta/uZ_{n-1}[\sin(n-1)\theta] \\ Z_n \cos n\theta \end{pmatrix},$$

$$\mathrm{EH}^{\mathrm{odd}} = \begin{pmatrix} j\beta/uZ_{n+1}[\sin(n+1)\theta] \\ j\beta/uZ_{n+1}[-\cos(n+1)\theta] \\ Z_n \sin n\theta \end{pmatrix}, \quad \mathrm{EH}^{\mathrm{even}} = \begin{pmatrix} j\beta/uZ_{n+1}[\cos(n+1)\theta] \\ j\beta/uZ_{n+1}[\sin(n+1)\theta] \\ Z_n \cos n\theta \end{pmatrix}.$$

CHAPTER IV

Design Principle and Core-Size Scalability of Effective Single-Mode CCC Fibers

In this chapter, the core-size scalability of effective single-mode CCC fibers is briefly discussed.

The two-mode coupling model is formulated with the coupled mode theory. The analytical solution illustrates the working mechanism of CCC effective single-mode operations, which is essentially to control the central mode effective loss α_a as a function of two-mode coupling strength κ, two-mode phase mismatch $\Delta\beta$ and side mode loss α_b.

Then, based on the analytical solutions of two-mode coupling model, we can discuss the design of effective single-mode CCC, and obtain the ultimate core-size scalability.

4.1 Two-Mode Coupling Model For CCC Fibers

4.1.1 Analytical Solution of Two-Mode Coupling Model

To investigate the core-size scalability of effective single-mode CCC design, we need to study the dynamics of mode coupling inside CCC fibers. First, let's start with the simplest case and explore the dynamics of two-mode coupling model: one central-mode amplitude $A(z)$ couples with one side-mode amplitude $B(z)$. The dynamics of this coupling is governed by the coupled mode equations derived in the early chapters. Here, we define the phase mismatch (propagation constant difference) $\Delta\beta$ as

$$\Delta\beta = \frac{\beta_a - \beta_b}{2}. \tag{4.1}$$

Substituting this quantity into the coupled mode equations Eq.(3.49), we have the coupled mode equations for two lossless modal coupling as

$$\begin{cases} dA/dz = -j\kappa_{ab} \cdot Be^{j2\Delta\beta z}, \\ dB/dz = -j\kappa_{ba} \cdot Ae^{-j2\Delta\beta z}, \end{cases} \tag{4.2}$$

where β_a, β_b and κ_{ab}, κ_{ba} are the modified ones in Eq.(3.50) and Eq.(3.51). In the dynamics of effective single-mode operation, the side mode amplitude loss $\alpha_b/2$ is necessary to consider, so we modify Eq.(4.2) to obtain the two-mode coupling model expressed as

$$\begin{cases} dA/dz = -j\kappa_{ab} \cdot Be^{j2\Delta\beta z}, \\ dB/dz = -j\kappa_{ba} \cdot Ae^{-j2\Delta\beta z} - \alpha_b/2 \cdot B, \end{cases} \tag{4.3}$$

We can solve this set of ordinary differential equations either numerically or analytically. In the following discussions, we are going to explore the analytical solutions for the initial condition: $A(0) = A_0$ and $B(0) = 0$, which is mimicking the condition of

launching the optical light into CCC fibers. Also, we will give numerical calculation to show the agreement between analytical and numerical results. With this initial condition, the analytical solutions for lossless coupled mode equations Eq.(4.2) are

$$A(z) = A_0 e^{-j\bar{\beta}z}\left[\cos(\sqrt{\Delta\beta^2+\kappa^2}z) - j\frac{\Delta\beta}{\sqrt{\Delta\beta^2+\kappa^2}}\sin(\sqrt{\Delta\beta^2+\kappa^2}z)\right], \quad (4.4)$$

$$B(z) = A_0 e^{-j\bar{\beta}z}\frac{-j\tilde{\kappa}_{ba}}{\sqrt{\Delta\beta^2+\kappa^2}}\cdot\sin(\sqrt{\Delta\beta^2+\kappa^2}z), \quad (4.5)$$

where we define average propagation constant $\bar{\beta}$ and effective coupling coefficient κ:

$$\bar{\beta} = \frac{\beta_a+\beta_b}{2}, \quad \kappa^2 = \kappa_{ab}\kappa_{ba}. \quad (4.6)$$

Eq.(4.3) shows that, we can include the side mode loss α_b into the propagation constant of side core:

$$\beta_b \to \beta_b - j\alpha_b/2. \quad (4.7)$$

so that Eq.(4.3) would be the same form as Eq.(4.2). Correspondingly, $\bar{\beta}$ and $\Delta\beta$ would include the side mode loss α_b as well:

$$\bar{\beta} \to \bar{\beta} - j\alpha_b/4, \quad \Delta\beta \to \Delta\beta + j\alpha_b/4. \quad (4.8)$$

Substituting the relations in Eq.(4.8) into the solution Eq.(4.4), we have the lossless central mode amplitude expressed as

$$A(z) = A_0 e^{-j\bar{\beta}z}e^{-\frac{\alpha_b}{4}z}\left[\cos(\sqrt{\Delta\beta^2-\alpha_b^2/16+j\alpha_b\Delta\beta/2+\kappa^2}z)\right.$$
$$\left.-j\frac{\Delta\beta+j\alpha_b/4}{\sqrt{\Delta\beta^2-\alpha_b^2/16+j\alpha_b\Delta\beta/2+\kappa^2}}\sin(\sqrt{\Delta\beta^2-\alpha_b^2/16+j\alpha_b\Delta\beta/2+\kappa^2}z)\right]. \quad (4.9)$$

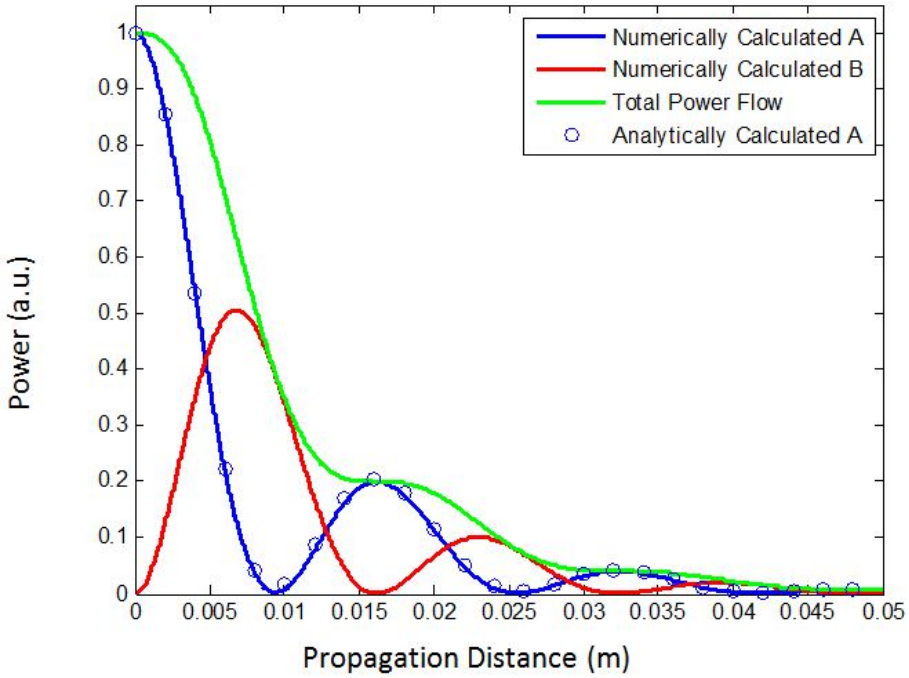

Figure 4.1: Typical Power Flow in Two-Mode Coupling Model.

Thus, the power flow of the lossless central mode $P_A(z)$ should follow

$$P_A(z) = |A(z)|^2. \tag{4.10}$$

To verify the validity of the analytically derived expression, we plot the numerical and analytical calculation results in Figure 4.1. We can see that, the blue circle of analytical calculation following Eq.(4.9) match the blue solid curve solved numerically based on the coupled mode equations in Eq.(4.3). It verifies that the analytical expression in Eq.(4.9) is the solution for the coupled mode equations in Eq.(4.3). Therefore, we would use this expression to derive the central mode effective loss in the following subsections.

4.1.2 Central Mode Effective Loss in CCC Fibers

Actually, the Figure 4.1 shows a typical power flow of coupling dynamics in a two-mode coupling model, which demonstrates that the power in such a coupling system

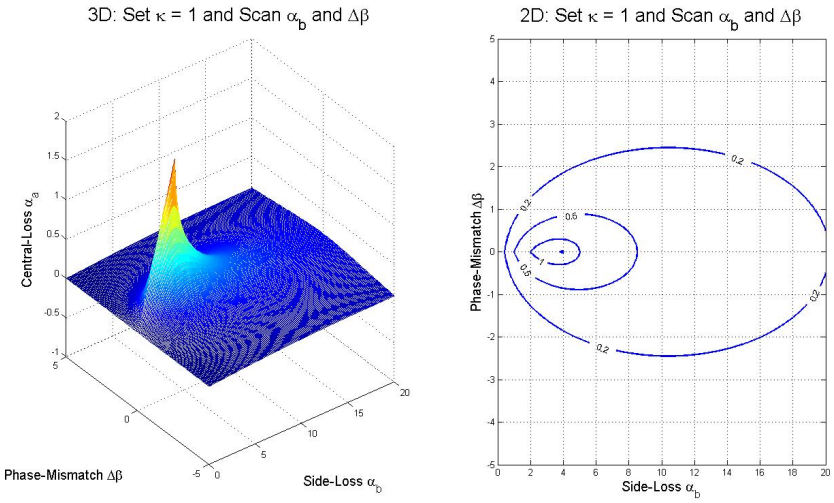

Figure 4.2: The general loss formula for the effective loss of lossless central core in CCC structure. The 3D plot and 2D contour plot of central-core loss as a function of coupling coefficient κ_{ab} and side-core loss α_b are shown side by side. The peak corresponds to the completely-phase-matching condition.

is going back and forth between central and side modes. Looking at the power flow of each individual mode, we can also see that, the power flow of central mode $P_A(z)$ exhibits a loss as it is going down after each coupling cycle and eventually disappears to be zero. Unlike the side mode, the central mode should have no intrinsic power loss, so we can call it as "central mode effective loss", which is due to the two-mode coupling:

$$\alpha_a = 0 \longrightarrow \alpha_a(\Delta\beta, \kappa, \alpha_b) > 0. \tag{4.11}$$

It means that the effective loss of the central mode should depend on the coupling condition which involves the phase mismatching $\Delta\beta$ and the cross-coupling coefficient κ, and the side modal loss α_b.

From the definition of modal loss, we can express the lossy amplitude evolution as this form:

$$|A(z)| \quad = \quad |A_0| \cdot e^{-\frac{\alpha_a}{2}z}. \tag{4.12}$$

By comparing Eq.(4.9) and Eq.(4.12), we can extract the analytical formula for central mode effective loss as

$$\alpha_a = \frac{\alpha_b}{2} - Im\left\{2\sqrt{\Delta\beta^2 - \alpha_b^2/16 + j\alpha_b\Delta\beta/2 + \kappa^2}\right\}. \tag{4.13}$$

Indeed, the central mode effective loss α_a is a function of phase-mismatch $\Delta\beta$, coupling strength κ, and side mode loss α_b.

To show how the central mode effective loss $\alpha_a(\Delta\beta, \kappa, \alpha_b)$ is dependent on the three parameter variables, we can assume one of variable is 1 and plot the function value against the other two variables. In Figure 4.2, we set $\kappa = 1$, and then we can plot the effective loss formula as a function of $\Delta\beta$ and κ. A 3D plot is on the left, where the value of central mode effective loss α_a is plotted as a surface. A 2D contour plot is on the right, where the contour line of α_a =1, 0.6, and 0.2 are plotted.

When large phase mismatch presents $\Delta\beta \gg 1$, we can see from Figure 4.2 that, the central mode effective loss is essentially zero $\alpha_a = 0$, no matter what value the other two parameters take. It means, when phase mismatch is large (at the wavelength off the phase matching condition resonances), the light propagating in this central mode would have no loss or negligible loss. This corresponds to the high transmission wavelength range in CCC transmission spectrum. When phase mismatch is zero $\Delta\beta = 0$, we can also see from the Figure 4.2 that, there is a peak value of central core effective loss α_a, which actually corresponds to the lossy dips we observed in CCC transmission spectrum. Within the bandwidth of these lossy dips, the central mode is expected to have large modal loss, so we can use these lossy dips with certain bandwidth to suppress the high order modes in the central core.

In fact, the key of designing effective single-mode CCC fibers relies on the two conditions: $\Delta\beta \gg 1$ and $\Delta\beta = 0$. We will have more discussion of these two cases in the next section.

4.2 Design Principle and Core-Size Scalability

4.2.1 Phase Mismatched Fundamental Mode: $\Delta\beta \gg \kappa$

To achieve CCC effective single-mode operation, the fundamental mode must be designed to have large phase mismatched $\Delta\beta \gg \kappa$ at the operation wavelength range. In other words, for a sample of CCC working around 1μm wavelength, the phase matching resonance conditions of central core fundamental mode in this CCC fiber must be away from 1μm wavelength as far as possible.

This can be explained by numerical plot in Figure 4.2. When we have large phase mismatched $\Delta\beta \gg \kappa$, the plot shows practically zero central mode effective loss, so the fundamental mode can be unperturbed and propagating along the CCC fibers.

This can also be explained by some analytical analysis. For the general case with finite value of phase-mismatch $\Delta\beta \neq 0$, we can rewrite the general loss formula in Eq.(4.13) to a more explicit form:

$$\begin{aligned} \alpha_a &= \frac{\alpha_b}{2} - 2\sqrt{\left(\Delta\beta^2 - \alpha_b^2/16 + \kappa^2\right)^2 + \left(\alpha_b\Delta\beta/2\right)^2} \\ &\quad \times \sin\left[\frac{1}{2}\tan^{-1}\left(\frac{\alpha_b\Delta\beta/2}{\Delta\beta^2 - \alpha_b^2/16 + \kappa^2}\right)\right]. \end{aligned} \tag{4.14}$$

Assuming large phase mismatch:

$$\Delta\beta \gg \alpha_b, \kappa. \tag{4.15}$$

we can approximate the Eq.(4.14) into such a form:

$$\alpha_a \rightarrow \frac{\alpha_b}{2} \times \left[1 - \frac{\Delta\beta}{\sqrt{\Delta\beta^2 - \alpha_b^2/16 + \kappa^2}}\right] \rightarrow 0, \tag{4.16}$$

which means the central mode effective loss is nearly zero under the condition of large phase mismatch.

4.2.2 Phase Matched Higher-Order-Modes: $\Delta\beta = 0$

To achieve CCC effective single-mode operation, the higher-order-mode(HOM) in the central core must be designed to achieve phase matched condition $\Delta\beta = 0$ at operating wavelength range. Thus, HOM would have large central mode effective loss based on the numerical plot in Figure 4.2. However, depending on the relative ratio between coupling strength κ and side mode loss α_b, the effective loss of the central mode also varies in a dramatic way in Figure 4.2. Therefore, let's assume phase matching condition $\Delta\beta = 0$, and investigate how to maximize the HOM effective loss, which is to essentially optimize the suppression of HOM.

By substituting $\Delta\beta = 0$ into the general loss formula Eq.(4.13), we have the central mode effective loss as a function of coupling strength κ and side mode loss α_b:

$$\alpha_a = \frac{\alpha_b}{2} - Im\left\{2\sqrt{-\alpha_b^2/16 + \kappa^2}\right\}, \tag{4.17}$$

which can be expressed more explicitly as

$$\alpha_a = \begin{cases} \alpha_b/2, \ \alpha_b < 4\kappa; \\ 2\kappa, \ \alpha_b = 4\kappa; \\ \alpha_b/2 - 2\sqrt{\alpha_b^2/16 - \kappa^2}, \ \alpha_b > 4\kappa. \end{cases} \tag{4.18}$$

The derived expression in Eq.(4.18) is a very important result. In Figure 4.3, we plot the central core loss α_a/κ as a function of side core loss α_b/κ based on the expression in Eq.(4.18).

We can see $\alpha_b = 4\kappa$ is a critical value. When the side core loss is below this critical value $\alpha_b < 4\kappa$, the central mode effective loss α_a is following half of the side mode loss $\alpha_b/2$. This makes perfect sense, because the central mode effective loss is essentially from the side mode loss. We would expect that the higher the side loss is, the higher the central effective loss is.

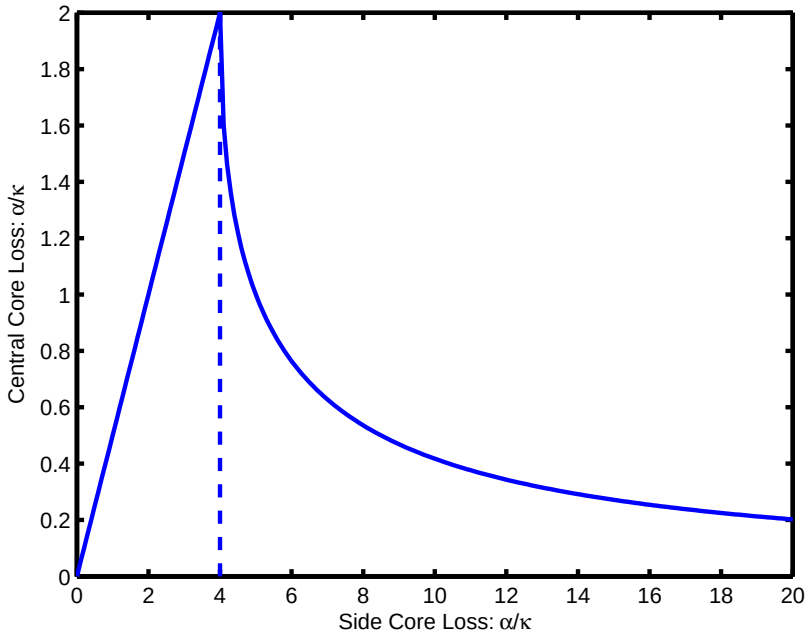

Figure 4.3: CCC Central Core Effective Loss At Phase Matching Condition.

However, when the side core loss is above the critical value $\alpha_b > 4\kappa$, the central mode effective loss starts to decrease when side loss further increases, which is a little counterintuitive. We can understand this in a more intuitive way by considering the extreme case — the side loss is infinitely large $\alpha_b = \infty$, which also implies that this side mode barely exists. To couple with a mode barely existed, the two-mode coupling must be quenched. Therefore, the excessively large side mode loss ($\alpha_b > 4\kappa$) would quench the coupling between the two cores, and thus quench the central mode effective loss as well.

When the side core loss is right equal to the critical value $\alpha_b = 4\kappa$, we can achieve the maximum suppression for the HOM. Therefore, in order to optimize the suppression for the central HOM in CCC fiber structure, not only the phase match condition $\Delta\beta = 0$ must be achieved, but the coupling κ and the side loss α_b must also "balance" with each other, and this "balance" is the key to design the well working effective single mode CCC fibers.

4.2.3 Ultimate Core-Size Scalability

Based on the Eq.(4.18) and Figure 4.3, we have known that the maximum suppression of HOM can only be achieved when $\alpha_b = 4\kappa$, and the maximum suppression can be achieved is 2 times of κ:

$$\alpha_{a,\max} = 2\kappa. \tag{4.19}$$

This actually means that we have an ultimate theoretical limit for HOM suppression. By simply calculating the coupling coefficient κ in the CCC structure, we can obtain this theoretical limit.

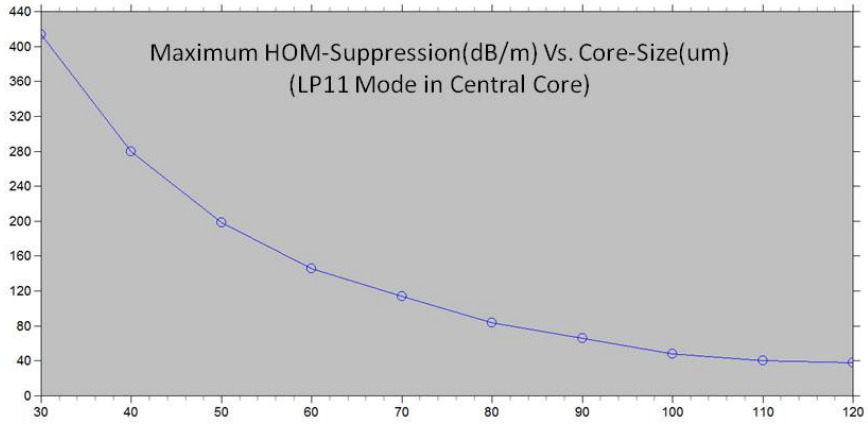

Figure 4.4: Demonstration of Ultimate Core-Size Scalability.

In Figure 4.4, for different core size of the central core in the horizontal axis, we calculate the ultimate HOM suppression in dB/m using Eq.(4.19) for the central core LP_{11} mode. Since LP_{11} mode always renders the lowest suppression compared with other HOM, Figure 4.3 could represent the ultimate core-size scalability for large-core effective single-mode operation. It shows that, even when core size reaches 120μm, we can still have the HOM suppression as high as 40dB/m. Knowing that the industrial standard for large-core effective single mode operation is 20dB HOM suppression with a certain length of fibers, 40dB/m HOM suppression is high enough to perform very well effective single-mode operations.

CHAPTER V

Numerical Algorithm and Related Simulation Tools

This chapter is dedicated to the numerical simulation of CCC fibers. Since CCC fiber is a real-world engineering device, analytical explanation of its performance is not sufficient. We need to fully understand the details of optical light propagating inside CCC fibers, and accurately predict the CCC performance with certain parameters. It turns out that, our self-developed Beam Propagating Method (BPM) algorithm is the only candidate that has such ability.

In the beginning of this chapter, we will start with the derivation from Maxwell equation to different BPM algorithms. Then, we will talk about different existing BPM algorithms, which would provide a context of how to formulate a BPM algorithm. Based on this given context, we will demonstrate the discretization, implementation and verification of self-developed BPM algorithm. After that, a few computer programs developed for simulating and designing the CCC fibers are briefly discussed.

5.1 From Maxwell Equation to Different BPM Formulations

5.1.1 Wave Equation with Anisotropic Permittivity

We start from the so called Source-Free Maxwell Equations:

$$\nabla \times \mathbf{E} = -\frac{\partial \mathbf{B}}{\partial t} \qquad \text{Faraday's law,} \tag{5.1a}$$

$$\nabla \times \mathbf{H} = \frac{\partial \mathbf{D}}{\partial t} \qquad \text{Ampère's law,} \tag{5.1b}$$

$$\nabla \cdot \mathbf{B} = 0 \qquad \text{Gauss's law for magnetism,} \tag{5.1c}$$

$$\nabla \cdot \mathbf{D} = 0 \qquad \text{Gauss's law,} \tag{5.1d}$$

where we have Non-Magnetic Anisotropic Material

$$\mathbf{B} = \mu_0 \mathbf{H}, \tag{5.2a}$$

$$\mathbf{D} = \epsilon_0 \tilde{\epsilon}_r \mathbf{E}, \tag{5.2b}$$

where ϵ_0 is vacuum dielectric constant, and the relative dielectric constant $\tilde{\epsilon}_r$ is a full tensor in general. To derive with electric field, we usually start from Faraday's Law:

$$\nabla \times (\nabla \times \mathbf{E}) \;=\; -\nabla \times \frac{\partial}{\partial t}\mathbf{B}. \tag{5.3}$$

The Left-Hand-Side(L.H.S.) and Right-Hand-Side(R.H.S.) of this equation are:

$$\text{L.H.S.} \;= \nabla \times (\nabla \times \mathbf{E}) = \nabla \cdot (\nabla \cdot \mathbf{E}) - \nabla^2 \mathbf{E}, \tag{5.4}$$

$$\text{R.H.S.} \;= -\nabla \times \frac{\partial}{\partial t}\mathbf{B} = -\mu_0 \frac{\partial}{\partial t} \nabla \times \mathbf{H} = -\epsilon_0 \mu_0 \frac{\partial^2}{\partial^2 t} \tilde{\epsilon}_r \mathbf{E}. \tag{5.5}$$

With the substitution $\epsilon_0 \mu_0 \to 1/c_0^2$, we have the Time-dependent Wave Equation:

$$\nabla^2 \mathbf{E} - \frac{1}{c_0^2} \frac{\partial^2}{\partial^2 t} \tilde{\epsilon}_r \mathbf{E} - \nabla \cdot (\nabla \cdot \mathbf{E}) = 0. \tag{5.6}$$

Assuming monochromatic wave propagation $\partial/\partial t \rightarrow j\omega$, we have the expression for optical waves propagating in space — Propagation Wave Equation:

$$\nabla^2\mathbf{E} + k_0^2\tilde{\epsilon}_r\mathbf{E} - \nabla\left[\nabla\cdot\mathbf{E}\right] = 0, \tag{5.7}$$

where $k_0 = \omega/c$ is the wave vector. Let's separate the permittivity tensor into a scalar permittivity ϵ_s representing the isotropic refractive index of the CCC fibers and another perturbation tensor term $\tilde{\epsilon}$ representing the linear and torsional birefringence $\tilde{\epsilon}_r = \epsilon_s + \tilde{\epsilon}$, where the perturbation $\tilde{\epsilon}$ is a full tensor as

$$\tilde{\epsilon} = \begin{pmatrix} \Delta\epsilon_1 & \epsilon_6 & \epsilon_5 \\ \epsilon_6 & \Delta\epsilon_2 & \epsilon_4 \\ \epsilon_5 & \epsilon_4 & 0 \end{pmatrix}, \tag{5.8}$$

Then, Gauss's Law goes

$$\nabla\cdot\mathbf{D} = \nabla\cdot(\tilde{\epsilon}_r\mathbf{E}) \approx \nabla\epsilon_s\cdot\mathbf{E} + \epsilon_s(\nabla\cdot\mathbf{E}) + \nabla(\tilde{\epsilon}\ \mathbf{E}) = 0, \tag{5.9}$$

which leads to:

$$\nabla\cdot\mathbf{E} \;=\; -\frac{\nabla\epsilon_s}{\epsilon_s}\cdot\mathbf{E} - \frac{1}{\epsilon_s}\nabla(\tilde{\epsilon}\ \mathbf{E}). \tag{5.10}$$

Substituting Eq.(5.10) into Eq.(5.7), we have an explicit form of Propagation Wave Equation with ϵ_s and $\tilde{\epsilon}$ as:

$$\nabla^2\mathbf{E} + k_0^2\tilde{\epsilon}_r\mathbf{E} + \nabla\left[\nabla\epsilon_s/\epsilon_s\cdot\mathbf{E}\right] + (1/\epsilon_s)\cdot\nabla\left[\nabla(\tilde{\epsilon}\ \mathbf{E})\right] = 0. \tag{5.11}$$

Since ϵ_s is the scalar refractive index of the fiber, the third term $\Delta\epsilon_s/\epsilon$ in Eq.(5.11) actually describes the guiding effect of the isotropic core and cladding. Thus, we can

call this term $\nabla\left[\nabla\epsilon_s/\epsilon_s \cdot \mathbf{E}\right]$ as the Guiding Term. For most of the optical fibers, they are actually so called weakly-guiding optical fibers, and this term can be approximated to be zero $\nabla\left[\nabla\epsilon_s/\epsilon_s \cdot \mathbf{E}\right] \to 0$. This is the case we call it as "weakly-guiding limit" (*Gloge*, 1971). However, for planner waveguides made of semiconductors or nonlinear crystals, the refractive-index change in these waveguide structures are large enough to produce physical effect, and the guiding term will become necessary to explain the entire physics described by the propagation wave equation in Eq.(5.11).

Since the expression $\nabla(\tilde{\epsilon}\ \mathbf{E})$ in the middle parenthesis of the fourth term $(1/\epsilon_s) \cdot \nabla\left[\nabla(\tilde{\epsilon}\ \mathbf{E})\right]$ in Eq.(5.11) has the same physical meaning as spacial change density in Gauss's Law, we can call this whole term as "Fictitious Charge term". Substituting the general form for the anisotropic perturbation tensor, the fourth term shows explicitly as:

$$\frac{1}{\epsilon_s} \cdot \nabla\left[\nabla(\tilde{\epsilon}\ \mathbf{E})\right] = \frac{1}{\epsilon_s} \cdot \nabla \left[\begin{pmatrix} \partial/\partial x \\ \partial/\partial y \\ \partial/\partial z \end{pmatrix} \begin{pmatrix} \Delta\epsilon_1 & \epsilon_6 & \epsilon_5 \\ \epsilon_6 & \Delta\epsilon_2 & \epsilon_4 \\ \epsilon_5 & \epsilon_4 & 0 \end{pmatrix} \begin{pmatrix} E_x \\ E_y \\ E_z \end{pmatrix} \right]. \tag{5.12}$$

If we assume the modal electric field has a longitudinal dependence $e^{-j\beta z}$, this expression can be approximated as

$$\frac{1}{\epsilon_s} \cdot \nabla\left[\nabla(\tilde{\epsilon}\ \mathbf{E})\right] \approx -\frac{j\beta}{\epsilon_s} \cdot \nabla\left[\epsilon_5 E_x + \epsilon_4 E_y\right], \tag{5.13}$$

where all the small terms are neglected and only the dominant terms are present. It shows that this term only contains the torsional birefringence ϵ_4 and ϵ_5. Thus, the fictitious charge term can be neglected when no torsional birefringence appears in the waveguide.

5.1.2 Overview of Different BPM Formulations

The transverse-field-based Beam-Propagation-Method(BPM) is the most popular algorithm used to simulate the propagation of optical waves in the waveguides, which is to essentially solve the propagation wave equation in Eq.(5.11). More accurately speaking, the BPM algorithm is to numerically solve the propagation wave equation by solving its approximated forms: Paraxial Equations. Thus, the BPM algorithm is definitely not the most accurate algorithm. However, since the paraxial equation is the first-order derivative of propagation variable z comparing with the second-order derivative in wave equation, the BPM algorithm certainly gives more promising speed. Plus, since the implicit BPM algorithm is essentially solving an eigenvalue problem of a tridiagonal matrix, it turns out to be very efficient and fast.

In fact, the transverse-field-based implicit FD-BPM is considered to be the fastest and the most reliable numerical algorithm for simulating the propagation wave equation so far. This is also the reason why we have to choose it to simulate the CCC fibers: it is the only numerical method that is capable of simulating long enough CC-C fiber structures (at least a few centimeters) within minutes. We have investigated several different numerical methods, and some of them such as Finite-Difference-Time-Domain (FDTD) and Finite-Element-BPM (FE-BPM) could certainly promise better accuracy and precision, but none of them could provide the eligible speed.

There are different BPM formulations when dealing with different forms of wave equation in Eq.(5.11). For example, when dealing with free-space propagation or propagation along ideal isotropic weakly-guiding fibers, neither the guiding term nor the fictitious charge term would appear in the wave equation, so the wave equation degrades to the vectorial Helmholtz equation:

$$\nabla^2\mathbf{E} + k_0^2\epsilon_s\mathbf{E} = 0, \tag{5.14}$$

where each component E_x, E_y and E_z of the vector field $\mathbf{E}$ is following the scalar Helmholtz equation independently:

$$\nabla^2 E(x,y,z) + k_0^2 n^2(x,y,z) E(x,y,z) = 0. \tag{5.15}$$

Solving this equation leads to the so called scalar BPM problem.

In terms of specific algorithm formulation, there is also quite a significant difference between 2D BPM problem and 3D BPM problem. The 3D function $E(x,y,z)$ in Eq.(5.15) indicates itself as a 3D BPM problem. If the 2D function $E(x,z)$ is used in Eq.(5.15) instead, then it is a 2D scalar problem. It turns out that the direct implementation of a 2D scalar problem would end up with a tridiagonal matrix, but 3D scalar problem would not. Thus, a very important technique called alternating-direction-implicit(ADI) method is used to convert a 3D scalar problem into a 2D scalar problem. More details are discussed in the following sections.

Other than scalar BPM formulation, there are several different FD-BPM algorithms available in literature and commercial market. Even though each of them is claimed or named to be "Vectorial BPM", none of them can really solve the problem with a full anisotropic permittivity tensor, especially with torsional birefringence. Up to date, the FD-BPM algorithm is limited to the formulation with only linear part of the anisotropic perturbation tensor, so permittivity tensor is

$$\tilde{\epsilon}_r = \epsilon_s + \begin{pmatrix} \Delta\epsilon_1 & \epsilon_6 & 0 \\ \epsilon_6 & \Delta\epsilon_2 & 0 \\ 0 & 0 & 0 \end{pmatrix}. \tag{5.16}$$

When the torsional birefringence is gone, we only have the guiding term:

$$\nabla^2 \mathbf{E} + k_0^2 \tilde{\epsilon}_r \mathbf{E} + \nabla \left[\nabla \epsilon_s / \epsilon_s \cdot \mathbf{E} \right] = 0. \tag{5.17}$$

Since the fictitious charge term is already dropped, we can write this wave equation in another form as

$$\nabla^2\mathbf{E} + k_0^2\tilde{\epsilon}_r\mathbf{E} - \nabla\left[\nabla\cdot\mathbf{E}\right] = 0, \tag{5.18}$$

where the permittivity tensor is expressed as

$$\tilde{\epsilon}_r \;=\; \begin{pmatrix} \epsilon_1 & \Delta\epsilon_6 & 0 \\ \Delta\epsilon_6 & \epsilon_2 & 0 \\ 0 & 0 & \epsilon_3 \end{pmatrix}. \tag{5.19}$$

This is actually the most comprehensive and complicated existing transverse-field-based FD-BPM so far. In our language, we can call this BPM formulation as "3D vectorial BPM".

We will show that, the direct implementation of 3D vectorial BPM could not work with ADI technique, and further simplifications with approximations or scarification from 2nd-order accuracy to 1st-order accuracy is needed to make it work. Thus, this BPM formulation is considered to be immature. However, there are two broadly used BPM algorithms called "Semi-Vectorial BPM" and "Full-Vectorial BPM", which are essentially simplified versions of 3D vectorial BPM. More specifically, they only keep the guiding term but throw the linear birefringence away:

$$\nabla^2\mathbf{E} + k_0^2\epsilon_s\mathbf{E} + \nabla\left[\nabla\epsilon_s/\epsilon_s\cdot\mathbf{E}\right] = 0. \tag{5.20}$$

Obviously, these two BPM formulations only contain scalar permittivity, and no vectorial tensor effect is involved. The word "Vectorial" here only means that, the large refractive index change $\Delta\epsilon_s$ is inducing different effects for different linearly polarized fields (Semi-Vectorial BPM) and sometimes even the cross-coupling effect between different linearly polarized fields (Full-Vectorial BPM).

From previous chapters, we have known that the practically-made CCC fibers contain linear and torsional birefringence. This means all the existing BPM formulations that we have discussed above are not capable of simulating the performance of CCC fibers. Therefore, we need to develop our own BPM algorithm to implement CCC anisotropic permittivity with both linear and torsional birefringence. In order to do so, our initial thinking is to do two things:

1. Drop the guiding term;

2. Keep the fictitious charge term.

Thus, we have wave equation for CCC problems as

$$\nabla^2\mathbf{E} + k_0^2(\epsilon_s + \tilde{\epsilon})\mathbf{E} + (1/\epsilon_s)\cdot\nabla\left[\nabla(\tilde{\epsilon}\ \mathbf{E})\right] = 0. \tag{5.21}$$

To drop the guiding term in CCC problem is not only legitimate due to the nature of the weakly guiding optical fibers, but also necessary to work with ADI method and obtain 2nd-order accuracy as a 3D propagation problem. However, to keep the fictitious charge term is a challenge: to the best of our knowledge, no one has ever managed to make it work in term of BPM formulations. We found out that, by making some approximations, we can derive an energy-conserved BPM formulation including the effect of torsional birefringence. We also benchmarked this BPM formulation with analytical results in the references. One of the following sections will be dedicated to discuss this self-developed BPM algorithm.

5.2 Existing BPM Formulations and Techniques

5.2.1 The Simplest Case: 2D Scalar BPM

As just has been pointed out, we have scalar Helmholtz equation for isotropic weakly guiding fibers as

$$\nabla^2 E(x,y,z) + k_0^2 n^2(x,y,z) E(x,y,z) = 0, \tag{5.22}$$

where refractive index is used instead of scalar permittivity $\epsilon_s(x,y,z) = n^2(x,y,z)$. We can separate the field envelope and the longitudinal propagation phase term

$$E(x,y,z) = \varepsilon(x,y,z) \cdot e^{-j\beta z}, \tag{5.23}$$

where β is effective propagation constant of the propagating waves, and often called as "reference k-vector". Then, we can substitute into the scalar Helmholtz Equation:

$$\left[\frac{\partial^2}{\partial x^2} + \frac{\partial^2}{\partial y^2} + \frac{\omega^2}{c^2} n^2(x,y,z)\right] \varepsilon(x,y,z) \cdot e^{-j\beta z} + \frac{\partial^2}{\partial z^2}\left[\varepsilon(x,y,z) \cdot e^{-j\beta z}\right] = 0, \tag{5.24}$$

which leads to

$$-\frac{d^2\varepsilon}{dz^2} + 2j\beta\frac{d\varepsilon}{dz} = \left[\frac{\partial^2}{\partial x^2} + \frac{\partial^2}{\partial y^2}\right] \varepsilon(x,y,z) + \left[k_0^2 \cdot n^2(x,y,z) - \beta^2\right] \varepsilon(x,y,z). \tag{5.25}$$

This equation is actually describing the propagating evolution of the electromagnetic optical field propagating along z direction. The left-hand-side is the evolution of the field along z direction, and the right-hand-side is the function of transverse distribution, waveguide configuration and propagating velocity. By definition, the modal field has no evolution at all because it is a stationary solution along the z direction, so the evolution on the left-hand-side of the Eq.(5.25) is required to be zero. Hence,

a modal field must satisfy the following equation:

$$\left[\frac{\partial^2}{\partial x^2}+\frac{\partial^2}{\partial y^2}\right]\varepsilon(x,y,z)+\left[k_0^2\cdot n^2(x,y,z)-\beta^2\right]\varepsilon(x,y,z)=0. \tag{5.26}$$

On the other hand, if the modal envelope function $\varepsilon(x,y,z)$ is given, we can use this equation to calculate the effective propagation constant β.

Usually, we apply Slowly Varying Envelope Approximation (SEVA) to Eq.(5.25)

$$\left|\frac{d^2\varepsilon}{dz^2}\right|\to 0, \tag{5.27}$$

then we have the envelope's paraxial equation:

$$2j\beta\frac{d}{dz}\varepsilon(x,y,z)=\left[\frac{\partial^2}{\partial x^2}+\frac{\partial^2}{\partial y^2}\right]\varepsilon(x,y,z)+\left[k^2(x,y,z)-\beta^2\right]\varepsilon(x,y,z), \tag{5.28}$$

where $k(x,y,z)$ is expressed as

$$k(x,y,z) \;=\; k_0\cdot n(x,y,z). \tag{5.29}$$

We have been discussing BPM for a while, but the real definition of the BPM method comes here: the numerical method that uses the paraxial equation Eq.(5.28) to simulate the electromagnetic wave propagating along one direction in space is called Beam Propagation Method (*Okamoto*, 2006; *Kawano and Kitoh*, 2001).

BPM algorithm is based on the paraxial equation Eq.(5.28), and the paraxial equation relies on two conditions:

1. Paraxial wave: less than 15° angle in ray picture;
2. Slowly varying envelope approximation: slowly varying structures.

Therefore, the problems that break either of the two conditions should not be qualified to use BPM method. For example, a photonic crystal waveguide with 90 degree

guiding corners breaks both of the above conditions, so it requires more accurate numerical method such as FDTD to do the simulation. The propagations inside CCC fibers satisfy both conditions, so we can use BPM method on CCC fibers.

Moreover, the core of the 2D scalar implicit FD-BPM is to solve an eigenvalue problem of a tridiagonal matrix, which is very fast (*Scarmozzino and Osgood, Jr.*, 1990). It turns out that, the BPM method could be less accurate, but it is the fastest in speed compared with other simulation methods (*Scarmozzino et al.*, 2000). Since CCC fibers typically have a helical period of several millimeters, we need to simulate at least a few centimeters to obtain the real performance and observe the physical effect. On the other hand, the time consuming must be within a few minutes per run. Thus, considering the fact that CCC fibers obey the paraxial equation and also require fast speed to simulate long propagation length, the BPM algorithm is the best and probably the only candidate so far.

Under the so called "Engineering Convention", we have the 2D scalar BPM

$$2j\beta u_z = u_{xx} + \left[k(x,z)^2 - \beta^2\right] u, \tag{5.30}$$

where the notation follows

$$u_z = \frac{du}{dz}, \quad u_{xx} = \frac{d^2u}{dx^2}, \quad u_{yy} = \frac{d^2u}{dy^2} \tag{5.31}$$

By further defining A, B coefficients as

$$A = \frac{1}{2j\beta},\ B = \frac{k^2(x,z) - \beta^2}{2j\beta}, \tag{5.32}$$

we can rewrite the 2D scalar BPM as

$$u_z = Au_{xx} + Bu. \tag{5.33}$$

With so called CN-Scheme (*Scarmozzino and Osgood, Jr.*, 1990), we can write the discretization of the Eq.(5.33) at the middle point $u_s^{r+1/2}$ (see Figure.5.1):

$$\begin{aligned}\frac{u_s^{r+1}-u_s^r}{\Delta z} &= \frac{1}{2}A_s^{r+1/2}\left[\frac{u_{s-1}^{r+1}-2u_s^{r+1}+u_{s+1}^{r+1}}{\Delta x^2}+\frac{u_{s-1}^{r}-2u_s^{r}+u_{s+1}^{r}}{\Delta x^2}\right] \\ &\quad +\frac{1}{2}B_s^{r+1/2}\left[u_s^{r+1}+u_s^r\right], \end{aligned} \tag{5.34}$$

where r stands for discretization along longitudinal z direction, and s stands for the discretization along transverse x or y direction. For convenience and simplicity, we define ascending symbol δ^+ and descending symbol δ^- as

$$\delta_\pm u_s = u_{s\pm1}. \tag{5.35}$$

Then, Eq.(5.34) becomes

$$2u_s^{r+1}-2u_s^r = \left[\rho A(\delta^+ + \delta^- - 2) + hB\right]\cdot\left(u_s^{r+1}+u_s^r\right), \tag{5.36}$$

with the substitutions

$$\rho = \frac{\Delta z}{\Delta x^2}, \quad h = \Delta z, \quad A = A_s^{r+1/2}, \quad B_s = B_s^{r+1/2}. \tag{5.37}$$

By collecting the known points u^r to the right hand side and the unknown points u^{r+1} to the left hand side of the equation, we have the 2D scalar BPM formulation as

$$\left[2-\rho A(\delta^+ + \delta^- - 2) - hB\right]u_s^{r+1} = \left[2+\rho A(\delta^+ + \delta^- - 2) + hB\right]u_s^r. \tag{5.38}$$

Here, we can see that, solving an unknown set of u_s^{r+1} is equivalent to finding the eigenvector of a tridiagonal matrix. Therefore, we use the so called "Thomas algorithm" and "Transparent Boundary Condition" to implement the algorithm. More details can be found in the references (*Okamoto*, 2006; *Kawano and Kitoh*, 2001;

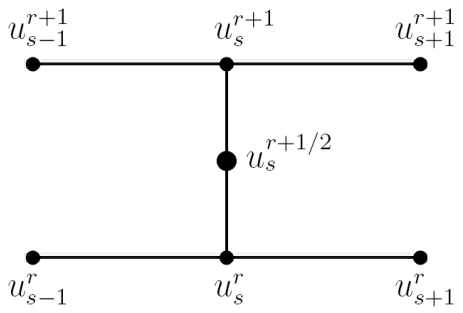

Figure 5.1: Algorithm Molecule for 2D Scalar BPM.

Hadley, 1991, 1992).

5.2.2 3D Scalar FD-BPM and ADI Method

Under the engineering convention, we have the paraxial equation for 3D scalar BPM formulation as

$$2j\beta u_z \;=\; u_{xx} + u_{yy} + \left[k(x,y,z)^2 - \beta^2\right] u. \tag{5.39}$$

To simplify the bulky expression, we introduce 2nd-Order differential operator δ_s^2:

$$\delta_s^2 = \delta_s^+ + \delta_s^- - 2, \tag{5.40}$$

which leads to

$$u_{xx} = \frac{\delta_x^2}{2\Delta x^2}[u_{i,j}^{r+1} + u_{i,j}^{r}], \quad u_{yy} = \frac{\delta_y^2}{2\Delta y^2}[u_{i,j}^{r+1} + u_{i,j}^{r}]. \tag{5.41}$$

Then, Eq.(5.39) becomes

$$\frac{u_{i,j}^{r+1} - u_{i,j}^{r}}{\Delta z} = \frac{1}{2}A_{i,j}^{r+1/2}\left[\frac{\delta_x^2}{\Delta x^2} + \frac{\delta_y^2}{\Delta y^2}\right][u_{i,j}^{r+1} + u_{i,j}^{r}] + \frac{1}{2}B_{i,j}^{r+1/2}\left[u_{i,j}^{r+1} + u_{i,j}^{r}\right]. \tag{5.42}$$

Then, we can separate all the coefficients into two Linear Operators $\hat{L}_x$ and $\hat{L}_y$:

$$\hat{L}_x = \frac{\Delta z}{2} A_{i,j}^{r+1/2} \frac{\delta_x^2}{\Delta x^2} + \frac{\Delta z}{4} B_{i,j}^{r+1/2}, \tag{5.43}$$

$$\hat{L}_y = \frac{\Delta z}{2} A_{i,j}^{r+1/2} \frac{\delta_y^2}{\Delta y^2} + \frac{\Delta z}{4} B_{i,j}^{r+1/2}. \tag{5.44}$$

This is an important step for making the ADI work. The point here is to separate two variables x and y (or differentiation along two directions) into two equally weighted linear operators, so we can later separate them into two equally weighted steps along two directions. Now, let's just plug them into Eq.(5.42), and after some algebra we can express the unknown points with the known points as:

$$(1 - \hat{L}_x - \hat{L}_y) u_{i,j}^{r+1} = (1 + \hat{L}_x + \hat{L}_y) u_{i,j}^{r}. \tag{5.45}$$

Based on this equation, we can already calculate the unknown points $u_{i,j}^{r+1}$ from the known points $u_{i,j}^{r}$, but the calculation mechanism would be a more complicated sparse matrix other than a tridiagonal matrix. For such a sparse matrix, either iterative method or non-iterative method with digital filter is needed (*Mansour et al.*, 1996), which turns out to be slow and noisy in terms of numerical results.

In general, it shows (*Press et al.*, 1992) the eigenvalue problem of tridiagonal matrix is a few order of magnitude faster than other sparse matrix. Therefore, we need to convert 3D scalar BPM formulations somehow into 2D scalar BPM formulations, so we can solve a tridiagonal matrix instead. This leads us to the so called Alternating Direction Implicit(ADI) method, which converts a 3D BPM problem to a two-step 2D problem. The trick is to introduce an extra term with 2nd-order accuracy $\hat{L}_x \hat{L}_y$. Since the BPM formulations with CN-scheme are intrinsically with 2nd-order accuracy, this extra term would maintain the same accuracy. Thus, we have Eq.(5.45) rewritten as

$$(1 - \hat{L}_x - \hat{L}_y + \hat{L}_x \hat{L}_y) u_{i,j}^{r+1} = (1 + \hat{L}_x + \hat{L}_y + \hat{L}_x \hat{L}_y) u_{i,j}^{r}. \tag{5.46}$$

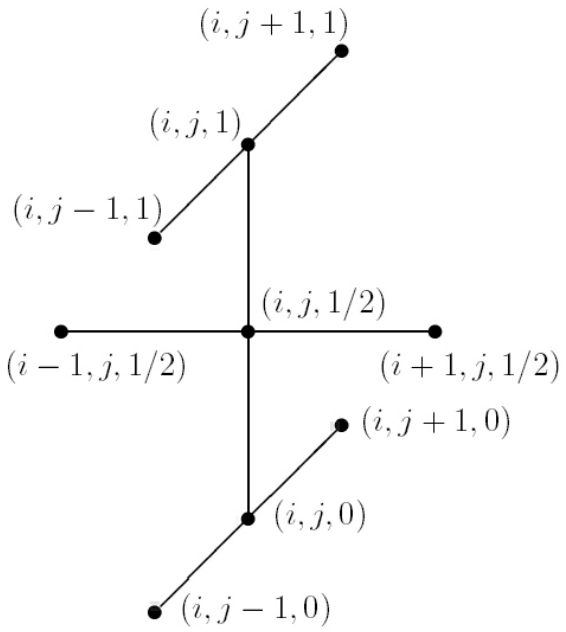

Figure 5.2: Algorithm Molecule for 3D Scalar BPM with ADI Method.

After some algebra, we can have the equation

$$u_{i,j}^{r+1} = \frac{1}{(1-\hat{L}_y)}(1+\hat{L}_x)\frac{1}{(1-\hat{L}_x)}(1+\hat{L}_y)u_{i,j}^{r}. \tag{5.47}$$

Now, we can separate into two steps

$$u_{i,j}^{r+1/2} = \frac{1}{(1-\hat{L}_x)}(1+\hat{L}_y)u_{i,j}^{r}, \tag{5.48}$$

$$u_{i,j}^{r+1} = \frac{1}{(1-\hat{L}_y)}(1+\hat{L}_x)u_{i,j}^{r+1/2}. \tag{5.49}$$

This means we have the Alternating Direction Implicit(ADI) formulation:

$$(1-\hat{L}_x)u_{i,j}^{r+1/2} = (1+\hat{L}_y)u_{i,j}^{r}, \tag{5.50}$$

$$(1-\hat{L}_y)u_{i,j}^{r+1} = (1+\hat{L}_x)u_{i,j}^{r+1/2}. \tag{5.51}$$

The name ADI actually explains how we use this formulation to perform the BPM algorithm:

1. Use the known points along y direction to generate the half-way unknown points along x direction;

2. Use the calculated half-way points along x direction to generate the final unknown points along y direction.

The algorithm molecule is shown in Figure 5.2.

5.2.3 3D Vectorial FD-BPM with ADI method

The full tensor form for 3D vectorial FD-BPM is described by Eq.(5.18) and Eq.(5.19). Since BPM algorithm is transverse-field based, we can first write down the transverse-field based wave equation as:

$$\nabla^2\mathbf{E} + k_0^2 \begin{pmatrix} \epsilon_{xx} & \epsilon_{xy} \\ \epsilon_{yx} & \epsilon_{yy} \end{pmatrix} \mathbf{E} - \nabla\left[\nabla \cdot \mathbf{E}\right] = 0. \tag{5.52}$$

Then, using Gauss's Law in Eq.(5.1d) and SVEA in Eq.(5.27), we can write down the coupled paraxial equations for transverse field $E_{x,y} = u_{x,y}e^{-j\beta z}$ as

$$\frac{\partial}{\partial z}\begin{bmatrix} u_x \\ u_y \end{bmatrix} = \begin{bmatrix} P_{11} & P_{12} \\ P_{21} & P_{22} \end{bmatrix}\begin{bmatrix} u_x \\ u_y \end{bmatrix}, \tag{5.53}$$

where the operators $P_{11}, P_{12}, P_{21}, P_{22}$ are defined as:

$$\begin{aligned}
P_{xx}u_x &= \frac{1}{2j\beta}\left\{\frac{\partial^2}{\partial y^2}u_x + \frac{\omega^2}{c_0^2}(\epsilon_{xx} - \bar{\epsilon})u_x + \frac{\partial}{\partial x}\left[\frac{1}{\epsilon_{zz}}\frac{\partial}{\partial x}(\epsilon_{xx}u_x) + \frac{1}{\epsilon_{zz}}\frac{\partial}{\partial y}(\epsilon_{yx}u_x)\right]\right\} \\
P_{xy}u_y &= \frac{1}{2j\beta}\left\{\frac{\omega^2}{c_0^2}\epsilon_{xy}u_y + \frac{\partial}{\partial x}\left[-\frac{\partial}{\partial y}u_y + \frac{1}{\epsilon_{zz}}\frac{\partial}{\partial x}(\epsilon_{xy}u_y) + \frac{1}{\epsilon_{zz}}\frac{\partial}{\partial y}(\epsilon_{yy}u_y)\right]\right\} \\
P_{yx}u_x &= \frac{1}{2j\beta}\left\{\frac{\omega^2}{c_0^2}\epsilon_{yx}u_x + \frac{\partial}{\partial y}\left[-\frac{\partial}{\partial x}u_x + \frac{1}{\epsilon_{zz}}\frac{\partial}{\partial x}(\epsilon_{xx}u_x) + \frac{1}{\epsilon_{zz}}\frac{\partial}{\partial y}(\epsilon_{yx}u_x)\right]\right\} \\
P_{yy}u_y &= \frac{1}{2j\beta}\left\{\frac{\partial^2}{\partial x^2}u_y + \frac{\omega^2}{c_0^2}(\epsilon_{yy} - \bar{\epsilon})u_y + \frac{\partial}{\partial y}\left[\frac{1}{\epsilon_{zz}}\frac{\partial}{\partial y}(\epsilon_{yy}u_y) + \frac{1}{\epsilon_{zz}}\frac{\partial}{\partial x}(\epsilon_{xy}u_y)\right]\right\}
\end{aligned}$$

To work with ADI method, we need to separate all the coefficient terms into two "equally-weighted" linear operators. For this purpose, we can rewrite the above equation with more operator terms

$$\frac{\partial}{\partial z}\begin{bmatrix} u_x \\ u_y \end{bmatrix} = \begin{bmatrix} P_{11}^{xx} + P_{11}^{yy} + C_{11}^{xy} & P_{12}^{xy} \\ P_{21}^{yx} & P_{22}^{xx} + P_{22}^{yy} + C_{22}^{yx} \end{bmatrix}\begin{bmatrix} u_x \\ u_y \end{bmatrix}, \tag{5.54}$$

where these operator terms are defined as

$$\begin{aligned}
P_{11}^{xx}u_x &= \frac{1}{2j\beta}\left\{\frac{1}{2}\frac{\omega^2}{c_0^2}(\epsilon_{xx}-\bar{\epsilon})u_x + \frac{\partial}{\partial x}\left[\frac{1}{\epsilon_{zz}}\frac{\partial}{\partial x}(\epsilon_{xx}u_x)\right]\right\}, \\
P_{11}^{yy}u_x &= \frac{1}{2j\beta}\left\{\frac{\partial^2}{\partial y^2}u_x + \frac{1}{2}\frac{\omega^2}{c_0^2}(\epsilon_{xx}-\bar{\epsilon})u_x\right\}, \\
C_{11}^{xy}u_x &= \frac{1}{2j\beta}\left\{\frac{\partial}{\partial x}\left[\frac{1}{\epsilon_{zz}}\frac{\partial}{\partial y}(\epsilon_{yx}u_x)\right]\right\}, \\
P_{12}^{xy}u_y &= \frac{1}{2j\beta}\left\{\frac{\omega^2}{c_0^2}\epsilon_{xy}u_y + \frac{\partial}{\partial x}\left[-\frac{\partial}{\partial y}u_y + \frac{1}{\epsilon_{zz}}\frac{\partial}{\partial x}(\epsilon_{xy}u_y) + \frac{1}{\epsilon_{zz}}\frac{\partial}{\partial y}(\epsilon_{yy}u_y)\right]\right\}, \\
P_{22}^{xx}u_y &= \frac{1}{2j\beta}\left\{\frac{\partial^2}{\partial x^2}u_y + \frac{1}{2}\frac{\omega^2}{c_0^2}(\epsilon_{yy}-\bar{\epsilon})u_y\right\}, \\
P_{22}^{yy}u_y &= \frac{1}{2j\beta}\left\{\frac{1}{2}\frac{\omega^2}{c_0^2}(\epsilon_{yy}-\bar{\epsilon})u_y + \frac{\partial}{\partial y}\left[\frac{1}{\epsilon_{zz}}\frac{\partial}{\partial y}(\epsilon_{yy}u_y)\right]\right\}, \\
C_{22}^{yx}u_y &= \frac{1}{2j\beta}\left\{\frac{\partial}{\partial y}\left[\frac{1}{\epsilon_{zz}}\frac{\partial}{\partial x}(\epsilon_{xy}u_y)\right]\right\}, \\
P_{21}^{yx}u_x &= \frac{1}{2j\beta}\left\{\frac{\omega^2}{c_0^2}\epsilon_{yx}u_x + \frac{\partial}{\partial y}\left[-\frac{\partial}{\partial x}u_x + \frac{1}{\epsilon_{zz}}\frac{\partial}{\partial x}(\epsilon_{xx}u_x) + \frac{1}{\epsilon_{zz}}\frac{\partial}{\partial y}(\epsilon_{yx}u_x)\right]\right\}.
\end{aligned}$$

We can see that, the variable-mixed operators C_{11}^{xy} and C_{22}^{xy} have both variable derivatives mixed up, and thus they can not be separated as two equally-weighted terms. Then, it comes to a very important point that, the two terms C_{11}^{xy} and C_{22}^{xy} in this coupled paraxial equation show contradiction with ADI method. Therefore, to keep the same order of accuracy and maintain the non-iterative ADI method, we need to drop these two terms

$$C_{xx} \to 0,\ C_{yy} \to 0. \tag{5.55}$$

It needs to be pointed out that, the off-diagonal terms P_{12}^{xy} and P_{21}^{yx} are also variable-mixed operators, but they are not against ADI method. We will see later that these two variable-mixed operators can be incorporated into the ADI method. Thus, only the diagonal terms with variable-mixed operators are not allowed for ADI method.

When two variable-mixed operator C_{11}^{xy} and C_{22}^{xy} are not dropped, the eigenvalue problem of the sparse matrix for the implicit method can be solved by iterative method, which can not guarantee the convergence and thus is very unstable. Alternatively, a 1st-order accuracy non-iterative method can be used (*Wang et al.*, 2006b), but we have to sacrifice the accuracy since the original accuracy is 2nd-order.

After dropping the diagonal variable-mixed operators C_{11}^{xy} and C_{22}^{xy}, we can define the x-directional linear operator L_x and y-directional linear operator L_y as

$$\hat{L}_x = \frac{\Delta z}{2}\begin{bmatrix} P_{11}^{xx} & 0 \\ P_{21}^{yx} & P_{22}^{xx} \end{bmatrix}, \quad \hat{L}_y = \frac{\Delta z}{2}\begin{bmatrix} P_{11}^{yy} & P_{12}^{xy} \\ 0 & P_{22}^{yy} \end{bmatrix}, \tag{5.56}$$

then the coupled paraxial equation for 3D vectorial BPM is

$$(1 - \hat{L}_x - \hat{L}_y)\hat{u}^{r+1} \;=\; (1 + \hat{L}_x + \hat{L}_y)\hat{u}^{r} \tag{5.57}$$

where $\hat{u}$ is defined as

$$\hat{u} \;\rightarrow\; \begin{bmatrix} u_x \\ u_y \end{bmatrix}. \tag{5.58}$$

We can see that Eq.(5.57) is now in the same form as Eq.(5.45), so we can follow the same procedure for ADI method and convert this 3D problem into two steps:

$$(1 - \hat{L}_y)\hat{u}^{r+1/2} = (1 + \hat{L}_x)\hat{u}^{r}, \tag{5.59}$$

$$(1 - \hat{L}_x)\hat{u}^{r+1} = (1 + \hat{L}_y)\hat{u}^{r+1/2}. \tag{5.60}$$

So the actual procedure could be written down as four consecutive steps:

$$2u_x^{r+1/2} - \Delta z P_{11}^{yy} u_x^{r+1/2} = 2u_x^r + \Delta z P_{11}^{xx} u_x^r + \Delta z P_{12}^{xy} u_y^r, \qquad 1^{st} \text{ step}, \quad (5.61a)$$

$$2u_y^{r+1/2} - \Delta z P_{22}^{yy} u_y^{r+1/2} = 2u_y^r + \Delta z P_{22}^{xx} u_y^r + \Delta z P_{21}^{yx} u_x^{r+1/2}, \qquad 2^{nd} \text{ step}, \quad (5.61b)$$

$$2u_y^{r+1} - \Delta z P_{22}^{xx} u_y^{r+1} = 2u_y^{r+1/2} + \Delta z P_{21}^{yx} u_x^{r+1/2} + \Delta z P_{22}^{yy} u_y^{r+1/2}, \qquad 3^{rd} \text{ step}, \quad (5.61c)$$

$$2u_x^{r+1} - \Delta z P_{11}^{xx} u_x^{r+1} = 2u_x^{r+1/2} + \Delta z P_{11}^{yy} u_x^{r+1/2} + \Delta z P_{12}^{xy} u_y^{r+1}, \qquad 4^{th} \text{ step}. \quad (5.61d)$$

In fact, this is the most generalized and complicated form of transverse-field-based 3D vectorial FD-BPM algorithm that have ever appeared in the literatures. However, this BPM algorithm is considered to be immature because of the two variable-mixed operators C_{11}^{xy} and C_{22}^{xy}.

There are two mature and very popular simplified versions of this 3D vectorial BPM algorithm, but they are limited to the problem without linear birefringence. In other words, we have

$$\epsilon_{xy} \to 0, \quad \epsilon_{yx} \to 0, \quad \epsilon_{xx} = \epsilon_{yy} \to n^2. \qquad (5.62)$$

Then, the troublesome terms C_{11}^{xy} and C_{22}^{yx} are automatically gone, and this becomes the so called "Full Vectorial 3D BPM". If we even drop the cross-coupling terms P_{12}^{xy} and P_{21}^{yx}, it becomes the so called "Semi-Vectorial 3D BPM", and the cross-coupling between the two orthogonal fields only happens in "Full Vectorial 3D BPM" case but not in "Semi-Vectorial 3D BPM" case. However, in both cases, the two linearly polarized orthogonal fields $\mathbf{E}_x$ and $\mathbf{E}_y$ are expected to behave differently. This is essentially due to the geometrical distribution of the refractive index profile. More specifically speaking, these effects are usually produced by the large refractive index jump or the sharp edges between different isotropic regions in the waveguides. Thus, they are generally used to simulate the polarization effect inside the isotropic waveg-

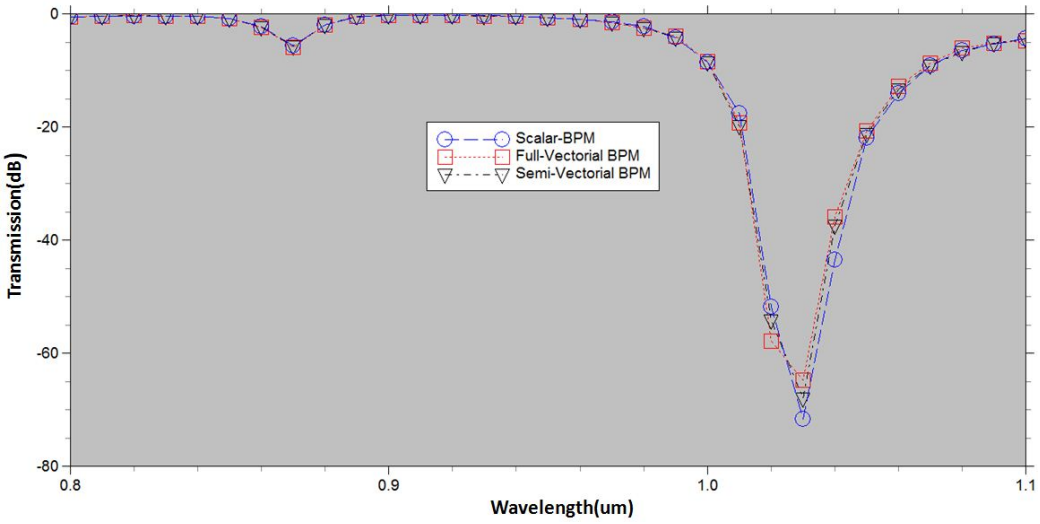

Figure 5.3: Comparing Scalar BPM with Full- and Semi-Vectorial BPM.

uides with large refractive index changes, such as the ones made of semiconductors or nonlinear crystals.

Since these two simplified versions of 3D vectorial BPM are commercially available, we have tested them in comparison with scalar BPM regarding the CCC fibers. In Figure 5.3, for 2 centimeter of a typical CCC fiber structure, we have shown the comparison of the three different algorithms. In terms of functionality, as expected, both of the two algorithms give the same performances as scalar BPM does. It confirms that, in weakly guiding fibers, the guiding-term-based semi-vectorial and full-vectorial BPM have no difference comparing with scalar BPM. In terms of speed, the semi-vectorial is 1.5 times slower than scalar BPM, and full-vectorial is 3.5 times slower. Thus, we can draw the conclusion that, these two BPM algorithms are of no use for CCC problems.

5.3 3D Transverse-Field-Based FD-BPM for Anisotropic C-CC

5.3.1 Transverse-Field Anisotropic Wave Equation

To obtain 3D transverse-field-based FD-BPM for anisotropic CCC fibers, we need to derive the wave equation with anisotropic permittivity, which is given by substituting Eq.(5.13) into Eq.(5.21):

$$\nabla^2\mathbf{E} + k_0^2(\epsilon_s + \tilde{\epsilon})\mathbf{E} - \frac{j\beta}{\epsilon_s}\cdot\nabla\left(\epsilon_5 E_x + \epsilon_4 E_y\right) = 0. \tag{5.63}$$

Substituting Eq.(3.78), Eq.(5.8), $\epsilon_s = n^2$ and $\nabla\sigma \approx 0$ into Eq.(5.63), we have the transverse field wave equation with full anisotropic tensor expressed as

$$\left[\nabla^2 + k_0^2\begin{pmatrix} n^2+\Delta\epsilon_1 & \epsilon_6 \\ \epsilon_6 & n^2+\Delta\epsilon_2 \end{pmatrix}\right]\begin{pmatrix} E_x \\ E_y \end{pmatrix} - j\beta\frac{\sigma\tau}{n^2}\begin{bmatrix} \frac{\partial}{\partial x}\left(-yE_x + xE_y\right) \\ \frac{\partial}{\partial y}\left(-yE_x + xE_y\right) \end{bmatrix} = 0. \tag{5.64}$$

Here comes a very important approximation:

$$\frac{\partial}{\partial x}\left(-yE_x + xE_y\right) = E_y - y\frac{\partial E_x}{\partial x} + x\frac{\partial E_y}{\partial x} \approx E_y, \tag{5.65}$$

$$\frac{\partial}{\partial y}\left(-yE_x + xE_y\right) = -E_x - y\frac{\partial E_x}{\partial y} + x\frac{\partial E_y}{\partial y} \approx -E_x. \tag{5.66}$$

This approximation is more like an assumption, because up to now no proof can be given to its general validity. However, this assumption directly leads to an energy-conserved transverse-field wave equation that can include the torsional birefringence. For convenience and simplicity, we define

$$\eta = \sigma\tau/n^2, \tag{5.67}$$

which is a quantity with the dimension as propagation constant β. Then, by substituting Eq.(5.65), Eq.(5.66) and Eq.(5.67) into Eq.(5.64), we have

$$\left[\nabla^2 + \begin{pmatrix} k_0^2[n^2 + \Delta\epsilon_1] & k_0^2\epsilon_6 - j\beta\eta \\ k_0^2\epsilon_6 + j\beta\eta & k_0^2[n^2 + \Delta\epsilon_2] \end{pmatrix}\right] \begin{pmatrix} E_x \\ E_y \end{pmatrix} = 0. \tag{5.68}$$

This is the form of wave equation we are going to use for anisotropic CCC fibers, where the linear birefringence is included by $\Delta\epsilon_1$, $\Delta\epsilon_2$ and ϵ_6, and the torsional birefringence is included by $\eta = \sigma\tau/n^2$.

We need to point out that, this form of wave equation in Eq.(5.68) is energy conserved. The energy conservation is guaranteed by the 2×2 Hermitian matrix in the parentheses of Eq.(5.68). As known, in order to make the algorithm work, the equation that the algorithm is based on must provide energy conservation. Thus, the energy conservation of Eq.(5.68) guarantees that the BPM algorithm based on this equation can be properly working in terms of numerical simulation.

5.3.2 Self-Developed BPM Algorithm: Implementation

Based on Eq.(5.68), we can implement a BPM algorithm which can handle the weakly-guiding waveguide with rotational linear birefringence and twisted torsional birefringence effect. We name this self-developed BPM algorithm as FISTS (Fiber Simulator with Torsion and Stress).

It is designed to simulate the optical wave propagation in the anisotropic CCC fibers, but it is not limited by it. For example, it can be used to simulate the effect of the stationary distributed linear birefringence in Polarization-Maintaining (PM) fibers. It can also be used to simulate the effect of twisting a normal piece of optical fiber. Hence, the FISTS algorithm can be used widely in fiber optics, such as PM fiber design, fiber sensor design and so on.

Since the formulation with the rotational linear birefringence and twisted tor-

sional birefringence includes the cases with stationary linear birefringence, no linear birefringence, and no twisted torsional birefringence. We will implement the BPM algorithm for the formulation with the rotational linear birefringence and twisted torsional birefringence.

Regarding the rotational linear birefringence, Eq.(3.76) already shows

$$\begin{pmatrix} \Delta\epsilon_1 & \epsilon_6 \\ \epsilon_6 & \Delta\epsilon_2 \end{pmatrix} = \begin{pmatrix} n_0 \cdot dn_l \cdot \cos 2\tau z & n_0 \cdot dn_l \cdot \sin 2\tau z \\ n_0 \cdot dn_l \cdot \sin 2\tau z & -n_0 \cdot dn_l \cdot \cos 2\tau z \end{pmatrix}, \tag{5.69}$$

where dn_l is the refractive index difference between the fast and slow axis of linear birefringence. Hence, the stationary linear birefringence can be obtained by taking $\cos \tau z \to 1$ and $\sin \tau z \to 0$, and no linear birefringence case corresponds to $dn_l = 0$.

The propagation constant β can also be expressed as

$$\beta \;=\; k_0 \cdot \bar{n}, \tag{5.70}$$

where $\bar{n}$ is the effective refractive index, which can be seen as a weighted average value for the refractive index value across the entire cross-section of the fiber or waveguide. Since η is defined as the same dimension as β, we can express η in a similar way:

$$\eta \;=\; k_0 \cdot dn_t, \tag{5.71}$$

where dn_t is a quantity as a refractive index difference similar to dn_l. We will see later that dn_t can be seen as the torsional birefringence.

By substituting Eq.(5.69), Eq.(5.70) and Eq.(5.71) into Eq.(5.68), we can write down the coupled paraxial equations as

$$\frac{\partial}{\partial z}\begin{bmatrix} u_x \\ u_y \end{bmatrix} \;=\; \left(\begin{bmatrix} P_{11}^{xx} & P_{12}^{xy} \\ 0 & P_{22}^{xx} \end{bmatrix} + \begin{bmatrix} P_{11}^{yy} & 0 \\ P_{21}^{yx} & P_{22}^{yy} \end{bmatrix} \right) \begin{bmatrix} u_x \\ u_y \end{bmatrix}, \tag{5.72}$$

where the operators are defined:

$$
\begin{aligned}
P_{11}^{xx}u_x &= \frac{1}{2j\beta}\left\{\nabla_x^2 u_x + \frac{1}{2}k_0^2[n_0^2 + n_0 dn_l \cos 2\tau z]\cdot u_x\right\},\\
P_{11}^{yy}u_x &= \frac{1}{2j\beta}\left\{\nabla_y^2 u_x + \frac{1}{2}k_0^2[n_0^2 + n_0 dn_l \cos 2\tau z]\cdot u_x\right\},\\
P_{12}^{xy}u_y &= \frac{1}{2j\beta}\left\{k_0^2 n_0 dn_l \sin 2\tau z\cdot u_y - jk_0^2\bar{n}dn_t\cdot u_y\right\},\\
P_{22}^{yy}u_y &= \frac{1}{2j\beta}\left\{\nabla_y^2 u_y + \frac{1}{2}k_0^2[n_0^2 - n_0 dn_l \cos 2\tau z]\cdot u_y\right\},\\
P_{22}^{xx}u_y &= \frac{1}{2j\beta}\left\{\nabla_x^2 u_y + \frac{1}{2}k_0^2[n_0^2 - n_0 dn_l \cos 2\tau z]\cdot u_y\right\},\\
P_{21}^{yx}u_x &= \frac{1}{2j\beta}\left\{k_0^2 n_0 dn_l \sin 2\tau z\cdot u_x + jk_0^2\bar{n}dn_t\cdot u_x\right\}.
\end{aligned}
$$

Substituting all these operators into Eq.(5.61), we have the FISTS algorithm.

5.3.3 Self-Developed BPM Algorithm: Verification

Regarding the validity of this self-developed BPM algorithm, we can have a series of verifications. For example, the first thing to verify is to benchmark this algorithm with a simple scalar BPM problem to see if it agrees with a commercially available standard BPM algorithm. We actually did this benchmark and it did show wonderful agreement. However, there might be more than a dozen of verifications like this kind to show. Therefore, to keep the discussion concise, we will only investigate the three most critical questions:

1. Is FISTS' rotational linear birefringence working properly?

2. Is FISTS' twisted torsional birefringence working properly?

3. Is FISTS capable of simulating anisotropic CCC fibers?

We will go through these three questions one by one.

Regarding the 1st question, we can compare the FISTS simulation with some known analytical results. In Snyder and McIntyre's work (*Snyder and McIntyre*,

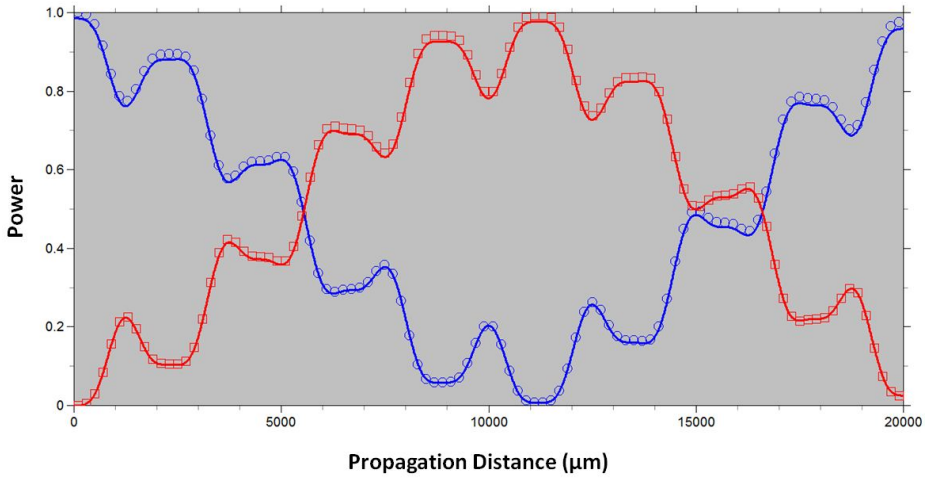

Figure 5.4: Verification of Linear Birefringence in FISTS.

1978), they investigated the evolution of the two orthogonal fields E_x and E_y when rotating linear birefringence presents. Assuming $A(z)$ and $B(z)$ are the envelope functions of fields E_x and E_y in local coordinates, they achieved the following results:

$$A(z) = \left[A_0 \cos(\sqrt{1+X^2}\tau z) + \frac{jXA_0 + B_0}{\sqrt{1+X^2}} \sin(\sqrt{1+X^2}\tau z)\right] e^{-j\bar{\beta}z}, \quad (5.73)$$

$$B(z) = \left[B_0 \cos(\sqrt{1+X^2}\tau z) - \frac{A_0 + jXB_0}{\sqrt{1+X^2}} \sin(\sqrt{1+X^2}\tau z)\right] e^{-j\bar{\beta}z}, \quad (5.74)$$

where we have $A_0 = A(0)$ and $B_0 = B(0)$ and average propagation constant $\bar{\beta}$ and ratio X (has different meaning with our X in Chapter III) are defined as

$$\bar{\beta} = \frac{\beta_x + \beta_y}{2}, \quad (5.75)$$

$$X = \frac{\beta_x - \beta_y}{2\tau}. \quad (5.76)$$

Then, the envelope functions $A_c(z)$ and $B_c(z)$ in the fixed laboratory Cartesian reference frame should take:

$$A_c(z) = A(z)\cos\tau z - B(z)\sin\tau z, \quad (5.77)$$

$$B_c(z) = A(z)\sin\tau z + B(z)\cos\tau z. \quad (5.78)$$

Thus, we can compare the FISTS simulation along z-direction with the equation above. For benchmarking, we take following parameters: wavelength at 1μm, helical pitch at 5mm, linear birefringence $dn_l = 2 \times 10^{-4}$, simulation length at 2cm, and the initial values are $A_0 = 1$ and $B_0 = 0$. Then we plot both the FISTS simulation and analytical calculation in Figure 5.4, where the blue curve is FISTS-simulated power evolution of $A_c(z)$, the blue circle points are analytically calculated power evolution of $A_c(z)$, the red curve is FISTS-simulated power evolution of $B_c(z)$, and the red rectangular points are analytically calculated power evolution of $B_c(z)$. We can see the simulation fits the analytical derivation very well. It means the rotational linear birefringence in FISTS is indeed working properly.

The 2nd question seems to be more complicated and quite involved, but on the contrary, all we need to do is to compare the algorithm formulation with some known analytical derivation results for the case of twisted optical fibers. In Ulrich and Simon's work (*Ulrich and Simon*, 1979), given an optical fiber with only twisted torsional birefringence and no linear birefringence, they found that the two orthogonal polarized modal field amplitude a_x and a_y should follow this set of coupled mode equations:

$$\frac{d}{dz}\begin{bmatrix} a_x \\ a_y \end{bmatrix} = -j\begin{pmatrix} 0 & -j\eta/2 \\ j\eta/2 & 0 \end{pmatrix}\begin{bmatrix} a_x \\ a_y \end{bmatrix}, \tag{5.79}$$

which follows the form of couple mode equations in Eq.(4.2) with $\Delta\beta = 0$ due to no linear birefringence. This set of couple mode equations means that, given the torsional photoelastic constant σ and twist rate τ, the torsional birefringence will induce an optical activity G whose value is half of the value of $\eta = \sigma\tau/n^2$:

$$G = \eta/2. \tag{5.80}$$

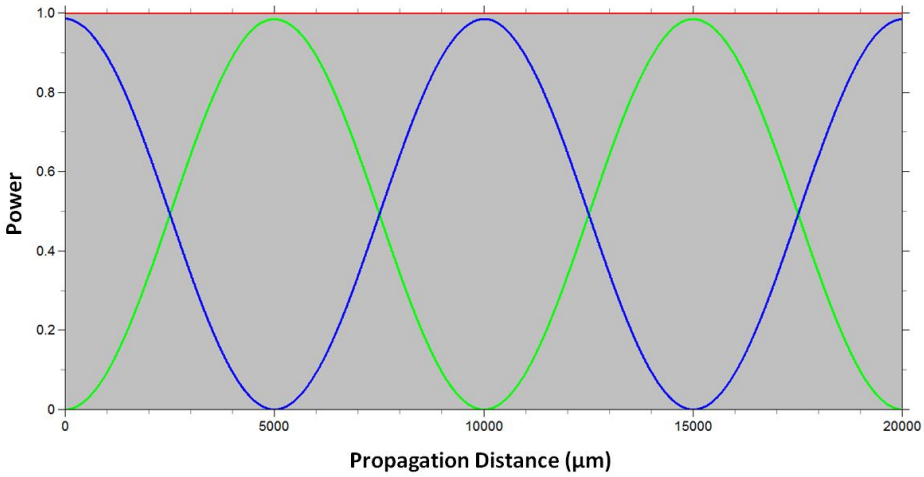

Figure 5.5: Verification of Torsional Birefringence in FISTS.

Now let's see what is happening inside the FISTS algorithm. If we assume u_x and u_y are two modal field amplitudes and there is no linear birefringence $dn_l = 0$, Eq.(5.72) would become

$$\frac{d}{dz}\begin{bmatrix} u_x \\ u_y \end{bmatrix} = -j\begin{pmatrix} 0 & -j\eta/2 \\ j\eta/2 & 0 \end{pmatrix}\begin{bmatrix} u_x \\ u_y \end{bmatrix}. \tag{5.81}$$

By comparing Eq.(5.79) and Eq.(5.81), we can see that, the algorithm formulation in FISTS shows exactly the same coupled mode equations as the analytical results in the reference. To further confirm this argument, we choose following parameters to do the FISTS simulation: wavelength at 1μm, simulation length at 2cm, torsional birefringence $dn_t = 10^{-4}$, no linear birefringence $dn_l = 0$. The propagation is plotted in Figure 5.5: blue and green curves are the evolution for the two orthogonal polarized fields, and the red curve is the total power which shows indeed the energy conservation. It also shows the beating length with these parameters is right about 1cm. From the optics theory, we know that the polarization beating length L_B is

$$L_B = \frac{2\pi}{2G} = \frac{2\pi}{\eta} = \frac{2\pi}{2\pi/\lambda \cdot dn_t} = \frac{\lambda}{dn_t} = \frac{10^{-6}m}{10^{-4}} = 1cm, \tag{5.82}$$

where the factor of 2 comes from the difference between power and amplitude. It shows good agreement. Therefore, the torsional birefringence is working properly as well.

Since FISTS is primarily designed to simulate anisotropic CCC performance, the 3rd question is the most critical question to answer. In fact, we have already given the positive answer in early chapters. In Figure 2.12, the FISTS-simulated transmission spectrum fits the experimental observation very well. We have used FISTS to characterize nearly a dozen of different CCC samples, and most of them give very good fit. We can give a general statement that FISTS works very well to predict the performance of anisotropic CCC fibers.

However, we have to point out a very important point about CCC torsional birefringence. In early chapters, we have argued that the torsional strain in CCC fibers are different from the one induced in twisted fibers. More specifically, the analytical derivation of torsional birefringence is based on the twisted fibers, so the CCC torsional birefringence due to the viscosity is expected to behave in a slightly different way. Thus, in the theoretical modal, we assumed the substitution $x = x\cos\tau z + y\sin\tau z$ and $y = -x\sin\tau z + y\cos\tau z$, and it worked perfectly for the theoretical derivation. But this substitution will lead to energy un-conserved numerical simulation in FIST-S algorithm. Instead, if we assume the substitution $x = x\cos\tau z$ and $y = y\cos\tau z$ in FISTS, then the algorithm maintains energy conserved and provide the current version of FISTS which is working very well to predict CCC performance.

To show that FISTS is the only BPM algorithm that is capable of simulating anisotropic CCC fibers, we compare the FISTS with two other BPM algorithms in Figure 5.6. Indeed, it shows only the FISTS algorithm can predict all the resonances of CCC fibers. The scalar BPM can only predict the scalar resonances marked as red dash lines in Figure 5.6, while the vectorial BPM can predict the scalar resonances and the linear birefringence resonances marked as yellow dash lines. The torsional

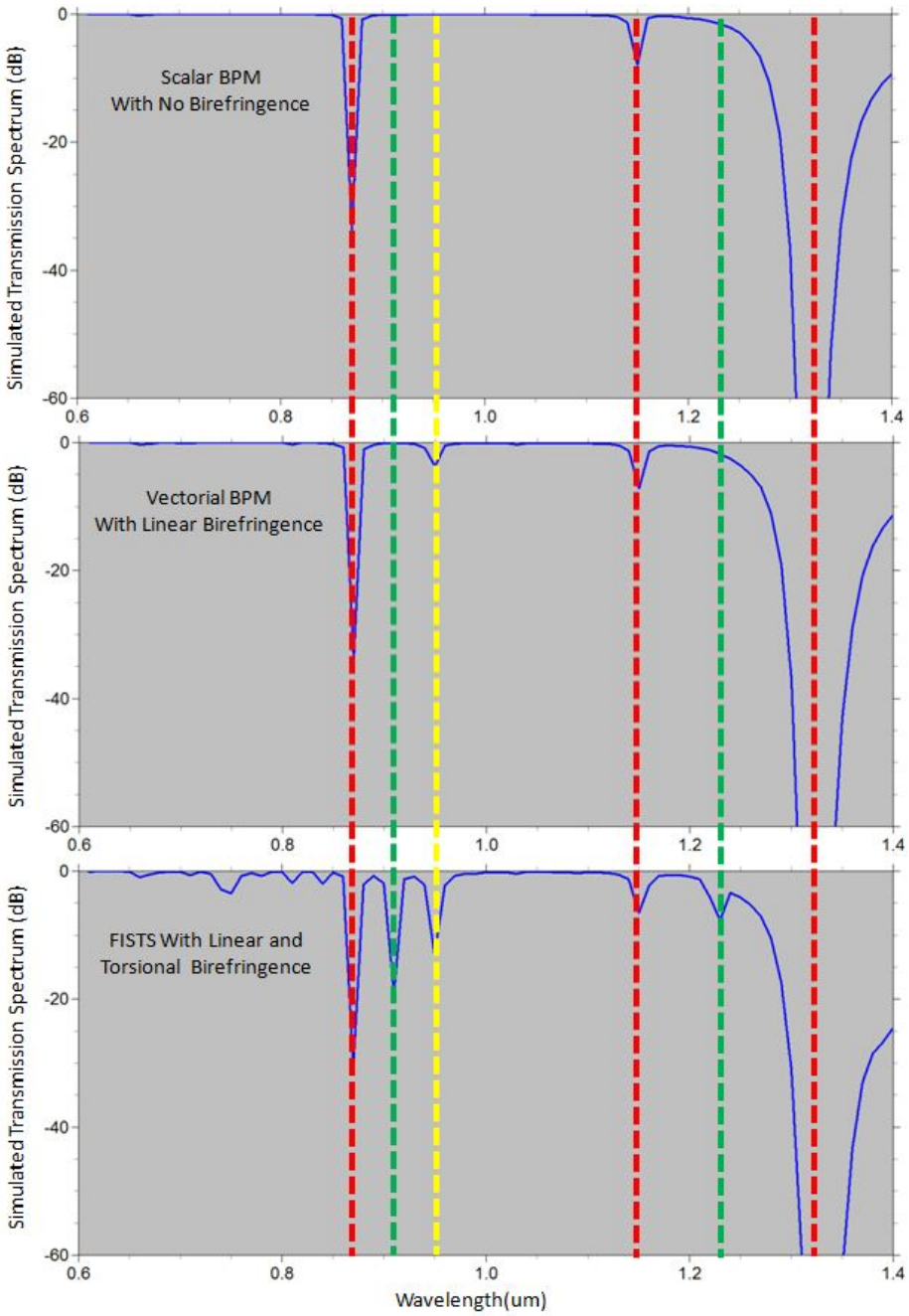

Figure 5.6: Comparison of BPM Algorithm with the Same Parameters for CCC Fiber.

birefringence marked as green dash lines can only be seen with FISTS. In general, to the best of our knowledge, FISTS is the most comprehensive algorithm that has ever be developed for simulating weakly guiding fibers.

5.4 FISTS Program and Other Related Simulation Tools

In this section, we will briefly introduce the computational tools that we have developed to design and characterize the CCC fibers. After all, the CCC fiber is a real-world and practically-made engineering device, which means it requires **fast**, **convenient**, and **accurate** designing tools. We have developed three different designing tools with MATLAB: the analytical tool CATS is **fast** but less accurate, so we use it to find the rough designing point; the numerical tool FISTS is relatively slower but can give **accurate** prediction of the CCC performance, so we use it for rigorous designing; the RATS control a commercial BPM simulator which provides a standard BPM simulation but cannot explain the CCC performance, so we use it as the calibration tool. All three programs are made with **convenient** interface and can be used as Windows executable program without MATLAB environment.

5.4.1 Fiber Simulator with Torsion and Stress (FISTS)

In Figure 5.7, the program interface for FISTS (Fiber Simulator with Torsion and Stress) Version1.8 is shown. It is a MATLAB-made Windows Executable Program, which means it is made with MATLAB, but it can still run without the MATLAB environment. In the program interface, there are 6 executive buttons, 3 functional menus, 4 display windows with 4 "Reset" buttons, and 1 additional advanced setting display window.

Clicking the button "Run" can start a calculation window as in Figure 5.8, and the 2D field evolution and power propagation are separately shown in this window. Clicking the button "Stop" and "Close" can stop the calculation and close this calculation window. Clicking the button "Plot" will open up an "Easyplot" program and plot the power propagation within the calculation window. Sometimes, we need to check the refractive index profile of the fiber structure, so we can click the button "Index" and the 2D plot of refractive index profile of the fiber cross section will be

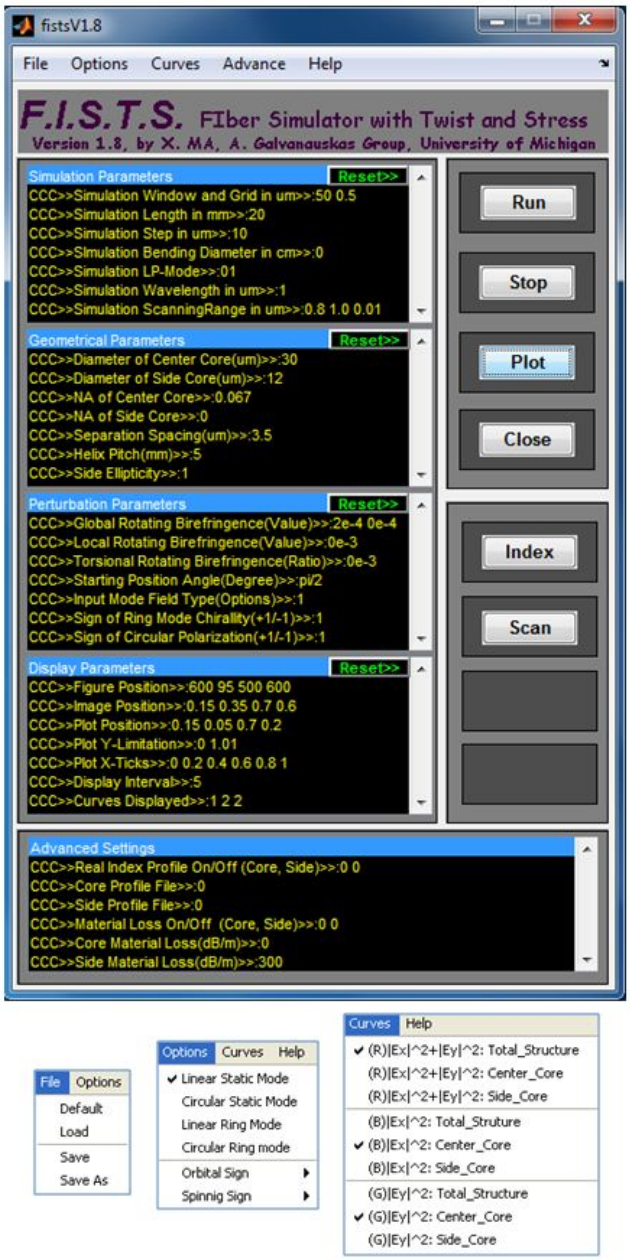

Figure 5.7: Program Interface For FISTS Version1.8.

shown in a popup window. The button "Scan" runs a series of simulations quietly without showing the evolution of the fields and power propagation, and shows the transmission spectrum for a list of wavelength positions by collecting the central core loss at the end of each simulation. For this wavelength scanning functionality, we have also implemented the parallel computing techniques to accelerate the simulation

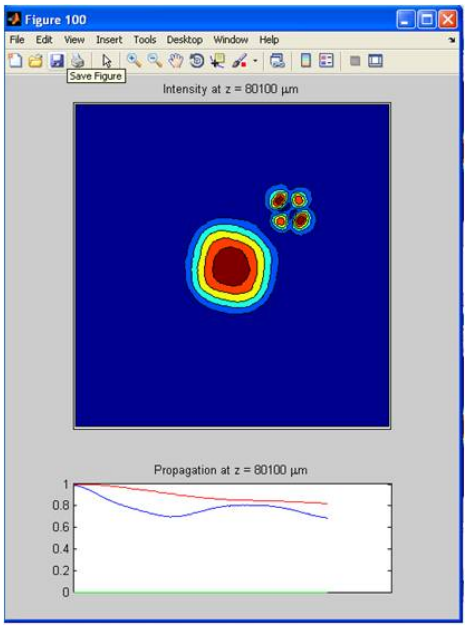

Figure 5.8: FISTS Calculation Window.

speed. Currently, for eight 10cm propagation simulations, we can run all of them in the parallel mode and it only costs 5 minutes in total.

The "File" menu is used to conveniently load and save parameters: "Default" loads the default value from a default parameter file; "Load" opens up an directory window and let user choose the parameter file to load; "Save" saves the current parameter settings to the default parameter file; "Save As" allows user to save the current parameter settings to a separate parameter file for future use. The "Options" menu gives the options to choose either static or helical modes with either linear or circular polarization, and the rotation sign of the orbital angular momentum or spin angular momentum can be selected too. The "Curves" menu gives the options to choose the representation of the red, blue and green curves in the calculation window, which is shown in Figure 5.8. For this particular case, the red curve represents the total power flow for both polarizations adding up "(R)|Ex|^2+|Ey|^2: Total_Structure", the blue curve represents the power flow in the central core with only one linear polarization component "(R)|Ex|^2: Center_Core", and the green curve represents the power flow

in the central core with another polarization "(R)|Ey|^2: Center_Core". Because the field we launch is only Ex component, and all birefringence terms have been deactivated for the isotropic case, the green curve always stay zero for this particular case. Due to the side core loss, we can see the red curve (total power flow) is declining. The blue curve is declining while oscillating due to the coupling with the side core.

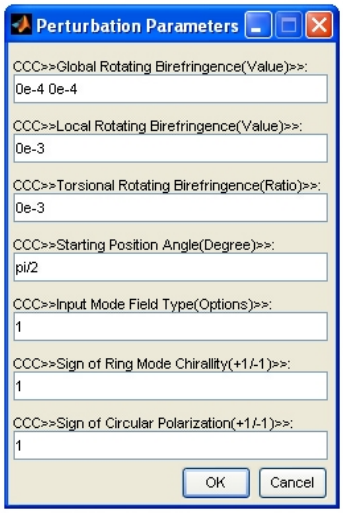

Figure 5.9: FISTS Pop-up Input Window.

Each display window contains 7 different input parameters, and clicking the "Reset" button besides the window will pop up the input window. For instance, the "Perturbation Parameters" pop-up input window is shown in Figure 5.9. This particular input window contains the most distinctive parameters for FISTS — the anisotropic birefringence in the CCC fibers. In Figure 5.9, "Global Rotating Birefringence" refers to the linear birefringence and torsional birefringence throughout the entire cross section of the structure. In fact, we currently don't see any global birefringence in CCC fiber, which we can intensionally generate by adding stress rods in the fiber cladding in the future. The "Local Rotating Birefringence" refers to the linear birefringence in the strongly distributed local area between two cores, and "Torsional Rotating Birefringence" refers to the torsional birefringence in the same area. In Figure 5.10, the referred "Local" area is plotted as an ellipse in the cladding located between two

cores, and the refractive index change along one polarization (e.g. Δn for E_x) is plotted. From the comparison of linear and torsional birefringence in the Figure 5.10, we can see the linear birefringence is oscillating at twice of the side core helix period, which is consistent with the result in Eq.(3.76), and the torsional birefringence is oscillating at the same period as helical period, which is consistent with the result in Eq.(3.82). This could intuitively explain how the FISTS generates all the QPM resonances: the linear and torsional birefringence oscillate periodically and generate the "sidebands". These sidebands are the equally separated QPM resonances in the transmission spectrum.

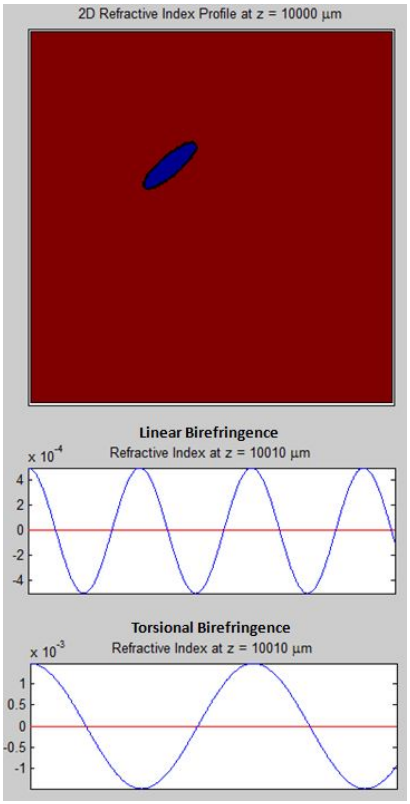

Figure 5.10: The Local Birefringence in FISTS.

Figure 5.10 is actually a snapshot of a movie, where the evolution of the cross-section refractive-index profile along the CCC fiber is shown dynamically. In fact, FISTS is capable of simulating any arbitrary cross-section profile for scalar refractive index, linear birefringence and torsional birefringence. For example, FISTS can do:

more side cores than just one side core, arbitrary refractive-index profile in one core, refractive-index rings on the edge of the cores, refractive-index dunes at the center of the core, and so on... Due to the limitation of the thesis volume, we cannot demonstrate all of them.

FISTS can also work under a batch mode. In such a batch mode, different sets of parameters can be written down one after one in a batch file. Then, the FISTS would run each set of parameters one by one. After the simulation of each set of parameters is done, the FISTS will automatically send email notification with simulation results attached. With this advanced feature, we can let the computer run for several days without intermittence, so we can achieve the most efficient way for optimizing the designing work of CCC fibers.

5.4.2 CCC Analytical Tool for Step-index (CATS)

In Figure 5.11, the program interface for CATS (CCC Analytical Tools for Step-index) Version7.0 is shown. It is also a MATLAB made Windows Executable Program. As its name, the CATS is an analytical tool, and all the calculations within this program are based on analytical methods for optical fibers, which means it is limited to the step-index optical fibers. Thus, it can not be used for the practically made CCC fibers with arbitrary refractive index profile. But, since the analytical calculations are very fast and usually can be done in seconds, we use CATS for rough searching towards the promising design region. As a matter of fact, at the time when FISTS had not been developed, we actually used CATS to design a few batches of effective single-mode CCC fibers, which turned out to give very good performances. Therefore, CATS is an important designing tool as useful as FISTS.

There are 6 executable buttons in total:

1. The executive button “Search” displays the existing modes in “Central Existing Modes” and “Side Existing Modes” frames. When “Search”

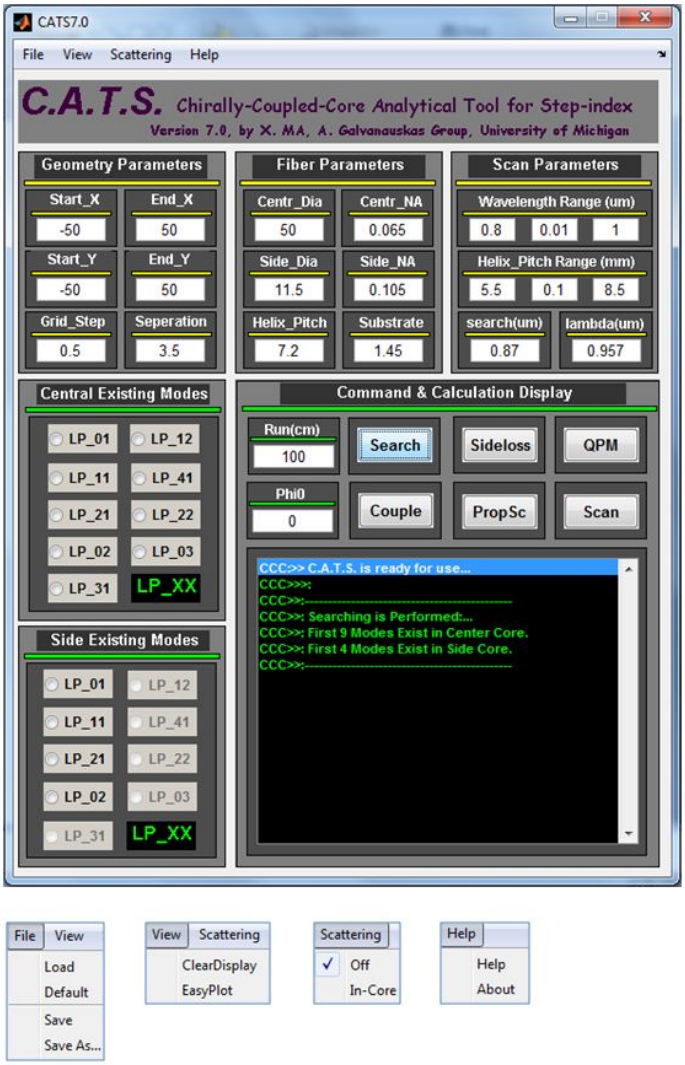

Figure 5.11: Program Interface For CATS Version7.0.

button is pressed down, the modes that exist in the fiber cores would be highlighted and ready to be chosen.

2. The "Sideloss" displays the modal loss of side mode which has been chosen in the "Side Existing Modes" frame. The 2D plot of the chosen side mode will be calculated based on the analytical formula for bent step-index optical fiber (*Marcuse*, 1975).

3. The "QPM" button displays two windows: one is the dispersion curves (modal effective refractive index as a function of wavelength in a 2D plot)

for both central core and side core, and the other is the QPM conditions (QPM resonances in a 2D plot with helical pitch as vertical axis and wavelength as horizontal axis) for the pair of coupling modes chosen in "Central Existing Modes" and "Side Existing Modes" frames.

4. The "Couple" button displays the coupling coefficients $\kappa_{pq}(p, q = a, b)$ in the output window beneath the executive buttons, and also shows the 1D and 2D modal profile of the two coupled modes.

5. The "PropSc" button stands for "propagation scan", and it will show the power flow while the two modes propagating and coupling along the CCC fiber.

6. The "Scan" button displays a wavelength scan regarding the performance of CCC fibers.

In Figure 5.12, the 2D plots calculated by CATS are shown together:

1. In "Figure 111", the horizontal axis is the distance in μm, and the vertical axis is the normalized amplitude. In "Figure 222", both the horizontal axis and the vertical axis are the distance in μm. "Figure 111" is the 1D view of the two coupled modes, while "Figure 222" is the 2D view of the two coupled modes. We can see that the two modes both penetrate into each other's core and the perturbation region between the two cores, which gives modal overlaps and interactions for this two-mode coupling.

2. "Figure 333" is the dispersion curves for the two coupled modes, where the horizontal axis is wavelength in μm and the vertical axis is the effective modal refractive index. The black curve is for the cladding refractive index value, and the blue curve is for the larger diameter central core mode The green and red curves are for the uncorrected and corrected side core mode respectively. Due to the side core helical path, the effective modal refractive index of the side core mode is lifted by a factor of $\sqrt{1 + K^2R^2}$, which

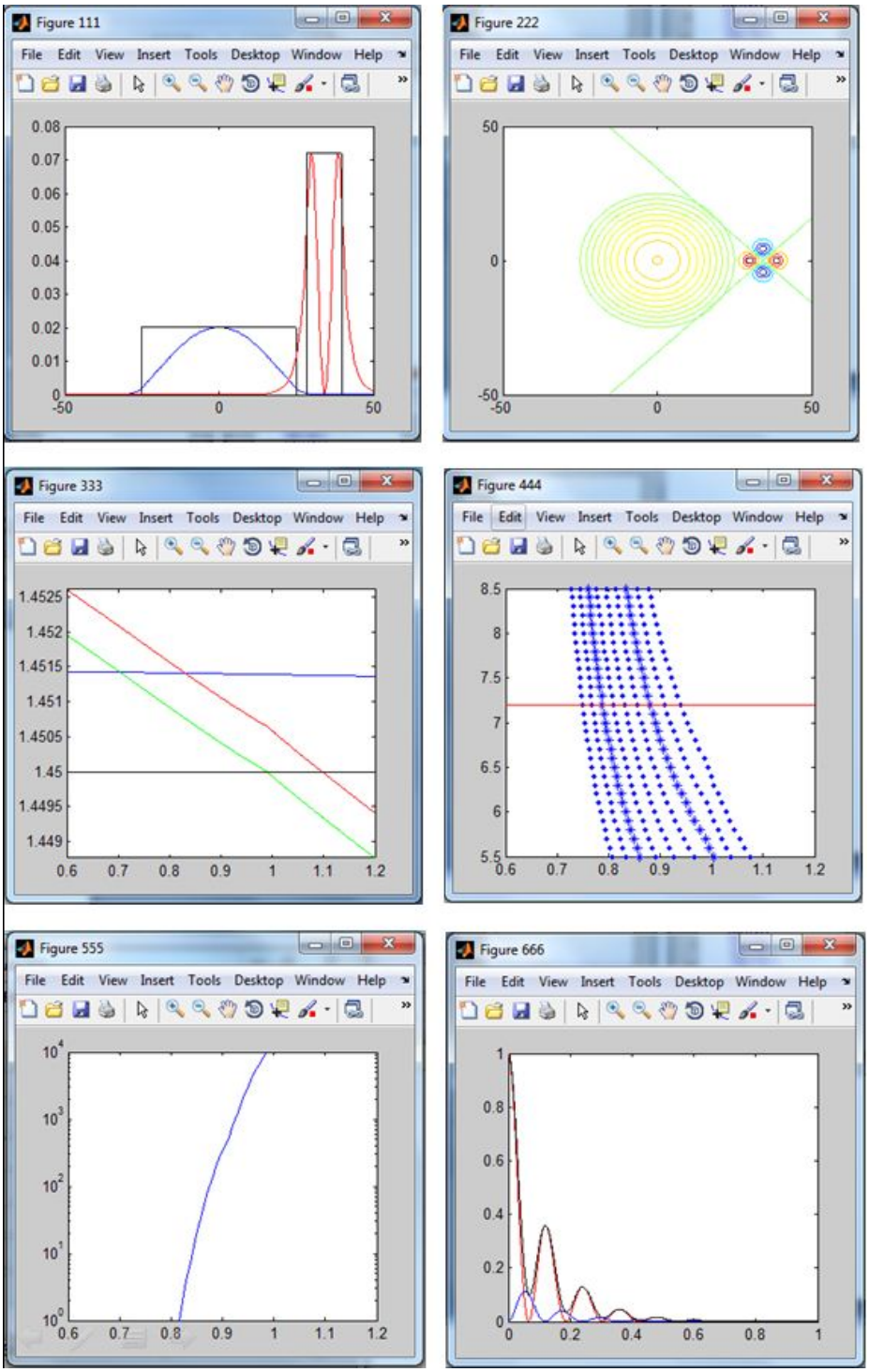

Figure 5.12: CATS Display Windows.

has been proven in early chapters. We can also notice that, the effective refractive index of side core mode crosses cladding refractive index 1.45 at around 1μm, and starts to be below 1.45 beyond 1μm. According to waveguide theory, only the modes with the effective refractive index larger than cladding refractive index 1.45 can be guided. Thus, these modes are called as "leaky modes". In fact, to use side core leaky mode is the reason why CCC fibers can introduced more than hundreds of dB/m side modal loss, because the bending loss usually cannot provide so large value.

3. "Figure 444" is the QPM conditions for the two coupled modes, where the horizontal axis is wavelength in μm and the vertical axis is the helical period in millimeter. The blue dotted curves are the QPM resonances. Since the red horizontal line is one value of the helical period, the cross points between the resonance curves and this red horizontal line are the QPM resonances for this particular helical period. We can see that the resonance position will move towards the shorter wavelength when the helical period gets longer, which is one of the means we can use to finely adjust the design.

4. "Figure 555" is the modal loss of the side core, where the horizontal axis is the wavelength in μm and the vertical axis is the side modal loss in dB/m. Knowing the results in "Figure 444" and "Figure 555', we can roughly design an effective single-mode CCC fiber based on the analysis and conclusion in Chapter IV.

5. "Figure 666" is the power flow for the CCC fiber regarding the propagation and the coupling between the two coupled modes, which is similar to the calculation in Figure 4.1. The horizontal axis is the propagation distance in meter, and the vertical axis is the normalized amplitude.

5.4.3 RSoft-Beamprop Active Test and Scan (RATS)

RSoft-Beamprop is a commercially available BPM program. It has been confirmed that RSoft-Beamprop cannot explain the performance the CCC fiber due to its lack of rotating linear birefringence and torsional birefringence. However, since it is broadly recognized as the most mature and trustable commercial simulator for BPM simulations, we can use it to calibrate our FISTS program. In Figure 5.13, the program interface for RATS (RSoft-Beamprop Active Test and Scan) Version1.5 is shown. For our purpose, we can gain more flexibility and convenience with RATS than with RSoft-Beamprop's own program interface.

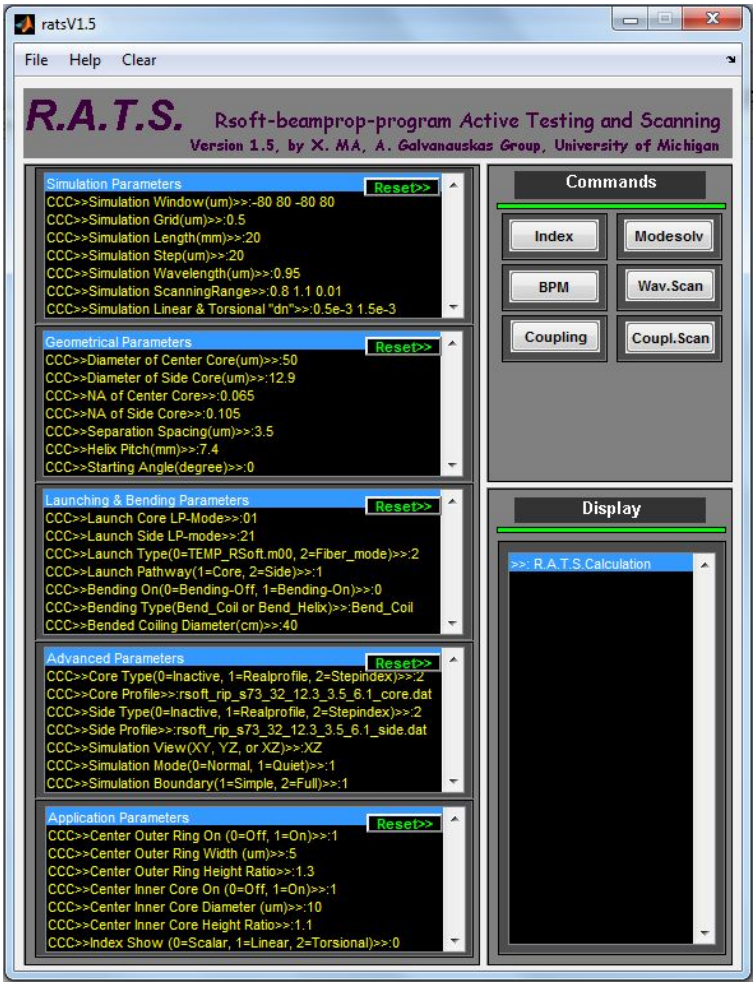

Figure 5.13: Program Interface For RATS Version1.5.

CHAPTER VI

Conclusion

In this final chapter of the entire dissertation, we are going to talk about the potential applications and the conclusions of CCC fibers.

The large-core-size effective single-mode CCC fiber, which is discussed with greater details in the previous chapters, is our primary application that has been successfully demonstrated in experiments. However, there are several other applications that we are currently pursuing but haven't demonstrated yet. Thus, we are going to briefly introduce these applications just for the purpose of demonstrating the idea and the concepts.

Due to the innovative nature of PhD thesis work, it is necessary to point out the innovations of this thesis comparing with up-to-date contemporary works. Several highlight points are discussed in terms of their academic contributions.

After that, a short final summary is given to illustrate the personal opinion towards the overall significance of CCC fibers.

6.1 Potential Applications of CCC Fiber

6.1.1 SRS Suppression with CCC Fibers

It is well known that the Stimulated Raman Scattering(SRS) is one of the major limiting factors for high power fiber laser, especially for the high energy pulsed laser in quasi-CW domain, and this type of laser is most needed for industry applications such as material processing, so the suppression of SRS is strongly urged in making this kind of industrial fiber lasers.

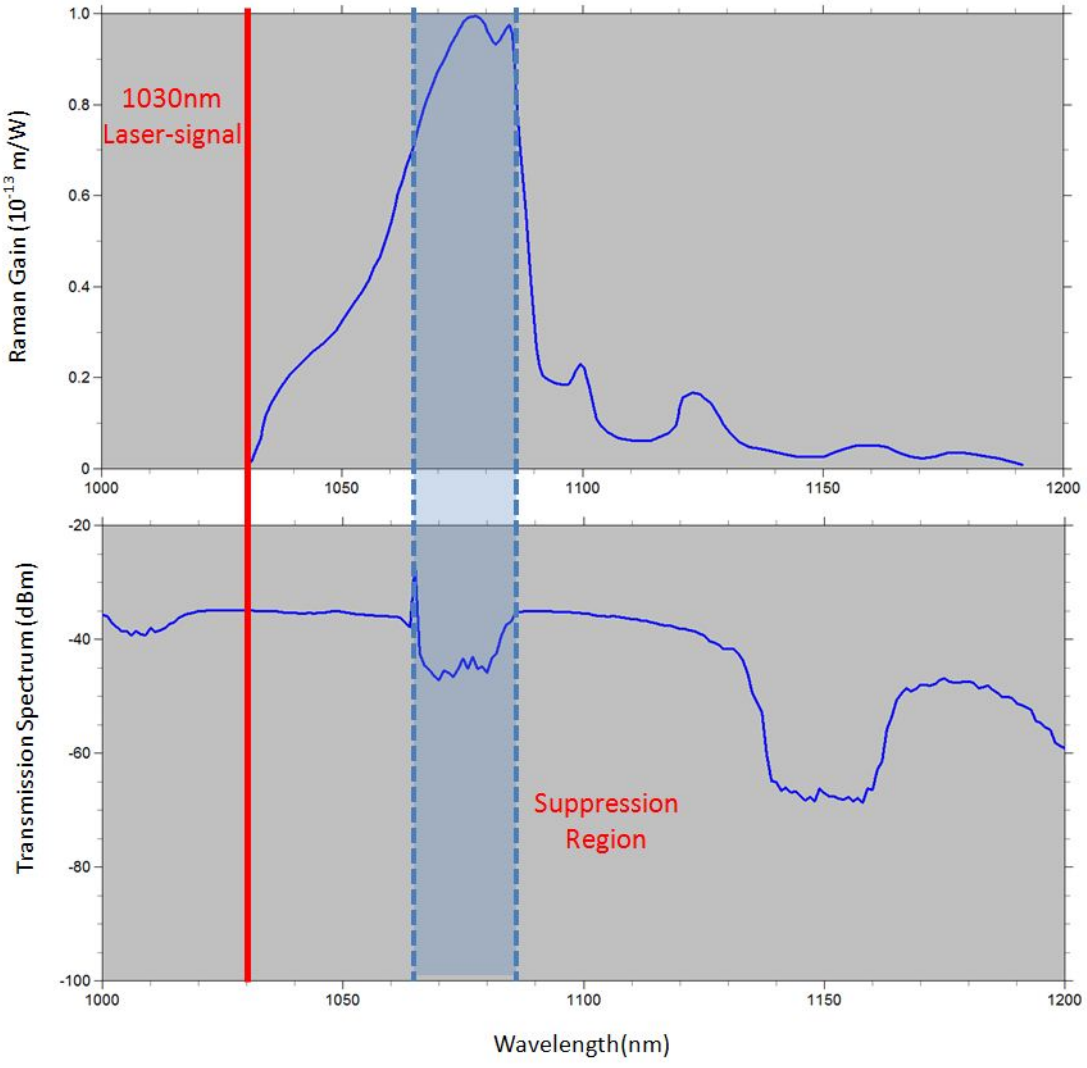

Figure 6.1: Suppression of Stimulated Raman Scattering in CCC Fibers.

In Figure 6.1, the suppression of SRS in a particular design of CCC fiber is shown. In the upper part of Figure 6.1, it shows the stokes Raman gain of fused silica for laser signal at 1030nm. In the lower part of Figure 6.1, it is the transmission spectrum of a particular design of passive CCC fiber. We can clearly see that the 10dB/m suppression would overlap with the peak of stokes Raman gain spectrum, so the stokes Raman gain is suppressed. We are currently working on demonstrating the SRS suppression.

6.1.2 Wavelength Selection of Yb-Doped Fiber Laser

In principle, we can design the CCC fiber to suppress any particularly chosen wavelength range, therefore, we can achieve wavelength selection for Yb-doped fiber laser or laser amplifier. Generally speaking, Yb-doped fiber laser prefers lasing around the range from 1030nm to 1070nm, but it is hard to control the lasing wavelength precisely without adding an active component inside the laser cavity such as a band-pass-filter. A free running Yb-doping fiber laser can lase at any wavelength between 1030nm and 1070nm depending on specific configuration of the laser cavity. With CCC fiber, by engineering the suppressed wavelength range, we can demand the Yb-doped CCC fibers only lase at one fixed wavelength. This will provide a more stable and intrinsic way to control the wavelength of Yb-doped fiber laser or laser amplifier.

It is well know that building a 980nm laser with Yb-doped fiber laser is very challenging. Around 980nm, due to the large absorption cross-section around this wavelength, the lasing is usually quite difficult to compete with the other lasing wavelength. However, if we can suppress other wavelength and provide the best scenario for 980nm to lase, then 980nm lasing wavelength might become superior to other lasing wavelength. This would provide a fundamentally easy way to achieve the 980nm Yb-doped fiber laser.

6.1.3 SBS Suppression with CCC Fibers

It is also well known that Stimulated Brillouin Scattering(SBS) is another major limiting factor for fiber laser, especially for CW laser with narrow linewidth signal. In fact, SBS is currently the exact reason preventing the current narrow linewidth fiber laser to reach 1000 Watts, to the best of my knowledge. Therefore, suppression of SBS is strongly needed for fiber laser community. Up to now, only a few ideas have been proposed to suppress the SBS, and one of them is the circular polarization dichroism. The idea is based on the fact that SBS only generates counter-propagating reflectively scattered light by the grating effect of Brillouin scattering. The reflection of circularly polarized optical wave always carries the opposite sign of circular polarization compared to the originally propagating optical wave. Therefore, if we have the circular polarization dichroism in the fiber which would prohibit the counter-propagating reflectively scattered light to propagate, we can essentially suppress the SBS from being generated inside the fiber.

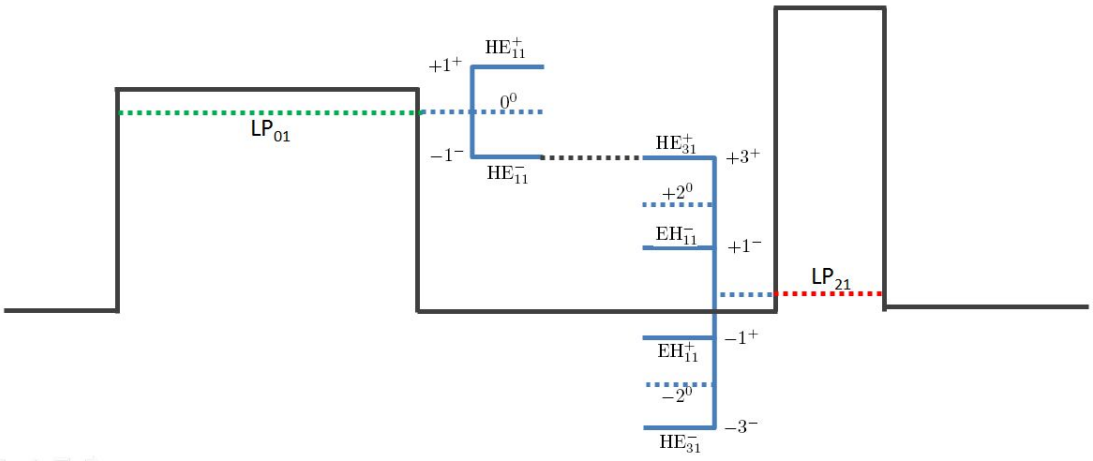

Figure 6.2: Circular Polarization Dichroism of CCC Fibers.

In Figure 6.2, the circular polarization dichroism of CCC fibers is demonstrated. The black profile in the plot is the refractive profile of central core (on the left) and the side core (on the right) separated by a distance as in CCC fibers. We can design a CCC fiber in such a way that the central core fundamental mode and side core LP_{21}

mode have the relationship shown in Figure 6.2. Then, one circular polarization for the fundamental mode in central core will be constantly coupled into the side core lossy LP_{21} mode, which means this circular polarization for fundamental mode in the central core will get lossy and eventually get suppressed.

6.1.4 Laser Beams with Optical Angular Momentum

We have experimentally demonstrated the generation of optical beam with optical angular momentum out of the side core and measured the quantum number of its orbital angular momentum in Chapter II. In principle, we can design the CCC fibers to be more efficient and convenient to generate such optical beams. Then, we can find numerous application in scientific community, including particle trapping and manipulation [8, 9], quantum communication [10] and quantum computing and information encoding in multi-dimensional quantum space [11]. More details can be found in references.

6.2 Up-to-date Innovation and Contemporary Comparison

6.2.1 Another Degree of Freedom in Optical Fibers

The most profound innovation of CCC fiber is to introduce another degree of freedom for controlling the modal properties, which is the optical angular momentum of the light in the optical fibers. There are two other fiber devices that contain the core with helical rotation:

1. Helical-core fibers (*Wang et al.*, 2006a);
2. Chiral fiber grating (*Kopp et al.*, 2004).

The helical-core fiber has just one helical core in the cladding. Since there is no coupling system, this fiber is simply mimicking the tightly coiled traditional LMA fibers. Therefore, no control of optical angular momentum is introduced.

The chiral fiber grating is to rotate an elliptical core or rectangular core in a very short period — a few μm. In fact, we can use the theory developed for CCC fiber in this thesis to understand the working mechanism of chiral fiber gratings. Instead of coupling the light from a central round core to a side round core in CCC fibers, the chiral fiber grating couples the light from elliptical or rectangular core to the cladding modes. Since the elliptical core or rectangular core is polarization sensitive, they can achieve the control of optical spin angular momentum, but there is no optical orbital angular momentum effect. In comparison, CCC fibers can control both the spin and the orbital angular momentum.

6.2.2 Effective Single-Mode Operation in Fiber Lasers

Effective single-mode operation in fiber lasers is currently the primary application of CCC fibers. Since large-mode-area effective single-mode fibers are so crucial for developing high power fiber lasers, there are quite a few different approaches including:

1. Helical-core fibers (*Wang et al.*, 2006a);
2. Gain-guiding fibers (*Xie et al.*, 2008);
3. Photonic-crystal fibers (*Baumgartl et al.*, 2011);
4. Leaky-channel fibers (*Dong et al.*, 2009).

Regarding the helical-core fiber, as has been pointed out, it is simply mimicking the tightly coiled traditional LMA fiber, so the effective single-mode operation of this fiber wouldn't exceed the performance of traditional LMA fibers.

Regarding the gain-guiding fiber, the core size can reach more than 100μm, but it can not be bent whatsoever. To keep it straight in the experiment setup, the length of the fiber has to be quite short. Therefore, the laser setups with gain-guiding fibers are practically solid-state lasers other than fiber lasers.

Regarding the photonic-crystal fibers, when the core size reaches more than 50μm, they become the so called "photonic-crystal rods", which can not be bent as well. Similar to gain-guiding fibers, the laser setup with photonic-crystal rods is more like solid-state laser and doesn't seem to preserve the advantage of fiber laser in the first place.

Regarding the leaky-channel fibers, samples with more than 100μm core size have been reported. However, up to now and to the best of our knowledge, no direct evidence of effectively single-mode operation has been demonstrated.

6.2.3 Derivation of Eigenmodes in CCC Structure

To the best of my knowledge, this is the first theoretical description of an optical waveguide obtained through transformational-optics approach by developing Maxwell equation-based theory in a curvilinear coordinate system.

6.2.4 Core-Size Scalability of CCC Design

In Chapter 4 we presented a simple two-mode interaction model that we used to evaluate the ultimate core-size scalability for single-mode operation. Based on this simplified model we argued that up to 40dB/m HOM suppression can be achieved for CCC core sizes of 100μm. In reality, scaling of CCC core is less straightforward, since in CCC structures modes can interact not only in pairs but also can interact in groups. This can create certain bottlenecks for power flow from central-core HOM into the "lossy" side core, which can effectively "quench" HOM suppression. We have observed such bottlenecks both numerically and theoretically, using multiple-mode interaction models. Our latest theoretical and design results show, that it is possible to overcome these bottlenecks and we recently designed CCC fibers with core sizes exceeding 50um with a predicted excellent HOM-suppressing performance (well above the HOM-suppression requirement for effectively single mode performance). However, due to the complicated nature of multiple-mode interactions in CCC fibers it is not straightforward to formulate a general accurate core-size scalability description.

6.2.5 Novel BPM Algorithm for CCC Simulation

The FISTS algorithm represents one of the most original technical contributions of this thesis work. FISTS has passed all the benchmarking for torsional birefringence in comparison with well-known analytical results (comparison with an existing analytical theory of optics of twisted optical fibers). To the best of my knowledge, this makes it the only available numerical methods to simulate weakly guiding optical fibers with torsional (twist-induced) birefringence.

6.3 Final Summary

This thesis is mainly about a new type of optical fiber that we have designed and fabricated. We name it as "Chirally-Coupled-Cores(CCC) Fiber". The experimental observations, theoretical analysis and numerical simulations are all consistently indicating that, the eigenmodes of optical field interacting and propagating in such fibers are the ones carrying spin and orbital angular momentums.

From the fundamental physics point of view, it goes profoundly to the new symmetry that we have introduced to CCC fibers. The degeneracy breaking for the modes with the same phase velocity but different optical angular momentum would enable a fundamentally new degree of freedom to control the optical light in optical fibers. It would be interesting for the scientific community to know the potential to use CCC fibers to manipulate the angular momentum of optical light just like the manipulation of atoms' in quantum physics. It could also provide advance scientific understanding toward angular momentum of optical light.

From the engineering point of view, it goes broadly to quite a few strongly-urged and novel applications described in the early sections of this chapter, which all come from the new degree of freedom of controlling the modal properties. Considering the fact that the CCC fibers are relatively easy to make (we have fabricated hundreds of meters of such fibers with our commercial manufactures), we believe they would be quite useful in all kind of areas ranging from "every-day" engineering devices to fundamental-scientific-study tools.

Therefore, by combining such a fundamental physics topic with such a broadly-used engineering device, we believe our work would be quite a contribution to both scientific and engineering community.

BIBLIOGRAPHY

BIBLIOGRAPHY

Allen, L., M. W. Beijersbergen, R. J. C. Spreeuw, and W. J. P. (1992), Mechanical Detection and Measurement of the Angular Momentum of Light, *Phys. Rev.*, *45*, 8185.

Allen, L., S. M. Barnett, and M. J. Padgett (2003), *Optical Angular Momentum*, I.O.P., London, UK.

Baumgartl, M., F. Jansen, F. Stutzki, C. Jauregui, B. Ortac, J. Limpert, and A. Tunnermann (2011), High average and peak power femtosecond large-pitch photonic-crystal-fiber laser, *Opt. Lett.*, *36*, 244.

Beth, R. A. (1936), Mechanical Detection and Measurement of the Angular Momentum of Light, *Phys. Rev.*, *50*, 115.

Borisenko, A. I., I. E. Tarapov, and R. A. Silverman (1979), *Vector and Tensor Analysis with Applications*, Dover Publications.

Dienerowitz, M., M. Mazilu, P. J. Reece, T. F. Krauss, and K. Dholakia (2008), Optical vortex trap for resonant confinement of metal nanoparticles, *Opt. Express*, *16*, 4991.

Dong, L., T.-w. Wu, H. A. McKay, L. Fu, J. Li, and H. G. Winful (2009), All-Glass Large-Core Leakage Channel Fibers, *IEEE J. Quantum. Electron.*, *15*, 47.

Feit, M. D., and J. A. Fleck, Jr. (1980), Compuration of mode eigenfunctions in graded-index opitcal fibers by the propagating beam method, *Appl. Opt.*, *19*, 2240.

Gahagan, T., and G. A. Swartzlander, Jr. (1996), Optical vortex trapping of particles, *Opt. Lett.*, *21*, 827.

Gibson, G., J. Courtial, M. Padgett, M. Vasnetsov, V. Pas'ko, S. Barnett, and S. Franke-Arnold (2004), Free-space information transfer using light beams carrying orbital angular momentum, *Opt. Express*, *12*, 5448.

Gloge, D. (1971), Weakly Guiding Fibers, *Appl. Optics*, *10*, 2252.

Hadley, G. R. (1991), Transparent boundary condition for beam propagation, *Opt. Lett.*, *16*, 624.

Hadley, G. R. (1992), Transparent Boundary Condition for the Beam Propagating Method, *IEEE J. Quantum. Electron.*, *28*, 363.

Hall, J. L. (2006), Nobel Lecture: Defining and measuring optical frequencies, *Rev. Mod. Phys*, *110*, 1279.

Huang, W.-P. (1994), Coupled-mode theory for optical waveguides: an overview, *J. Opt. Soc. Am. A*, *11*, 963.

Kao, C. K. (2010), Nobel Lecture: Sand from centuries past: Send future voices fast, *Rev. Mod. Phys*, *82*, 2299.

Kawano, K., and T. Kitoh (2001), *Introduction to Optical Waveguide Analysis*, Wiley, NJ, US.

Knight, J. C., J. Broeng, T. A. Birks, and P. S. J. Russell (1998), Photonic Band Gap Guidance in Optical Fibers, *Science*, *282*, 1476.

Kopp, V. I., V. M. Churikov, J. Singer, N. Chao, D. Neugroschl, , and A. Z. Genack (2004), Chiral Fiber Gratings, *Science*, *305*, 74.

Li, M.-J., X. Chen, and N. D. A. (2004), Effects of residual stress on polarization mode dispersion of fibers made with different types of spinning, *Opt. Lett.*, *29*, 448.

Mansour, I., A.-D. Capobianco, and C. Rosa (1996), Noniterative Dover Publications Vectorial Beam Propagation Method with a Smoothing Digital Filter, *J. Lightwave Technol.*, *14*, 908.

Marcuse, D. (1975), Curvature loss formula for optical fibers, *J. Opt. Soc. Am.*, *66*, 216.

Marrucci, L., C. Manzo, and D. Paparo (2006), Optical Spin-to-Orbital Angular Momentum Conversion in Inhomogeneous Anisotropic Media, *Phys. Rev. Lett.*, *96*, 163,905.

Molina-Terriza, G., J. P. Torres, and L. Torner (2007), Twisted photons, *Nature Physics*, *3*, 305.

Nicholson, J. W., A. D. Yablon, S. Ramachandran, and S. Ghalmi (2008), Spatially and spectrally resolved imaging of modal content in large-mode-area fibers, *Opt. Express*, *16*, 7233.

Nicolet, A., F. Zolla, and S. Guenneau (2004), Modelling of twisted optical waveguides with edge elements, *Eur. Phys. J. Appl. Phys.*, *28*, 153.

Okamoto, K. (2006), *Fundamentals of Optical Waveguides*, Academic Press, MA, US.

Pietralunga, S. M., M. Ferrario, M. Tacca, and M. Martinelli (2006), Local Birefringence in Unidirectionally Spun Fibers, *J. Lightwave Technol.*, *24*, 4030.

Press, W. H., B. P. Flannery, S. A. Teukolsky, and W. T. Vetterling (1992), *Numerical Recipes in C: The Art of Scientific Computing*, Cambridge, NY, US.

Scarmozzino, R., and R. M. Osgood, Jr. (1990), Comparison of finite-difference and Fourier-transform solutions of the parabolic wave equation with emphasis on integrated-optics applications, *J. Opt. Soc. Am. A*, *8*, 724.

Scarmozzino, R., A. Gopinath, R. Pregla, and S. Helfert (2000), Numerical Techniques for Modeling Guided-Wave Photonic Devices, *IEEE J. Sel. Top. Quantum Electron.*, *6*, 150.

Snyder, A. W., and P. McIntyre (1978), Light propagation in twisted anisotropic media: Application to photoreceptors, *J. Opt. Soc. Am.,*, *68*, 149.

Tai, H., and R. Rogowski (2002), Optical anisotropy induced by torsion and bending in an optical fiber, *Optical Fiber Technology*, *8*, 162.

Timoshenko, S. (1970), *Theory of Elasticity*, McGraw-Hill, NY, US.

Ulrich, R., and A. Simon (1979), Polarization optics of twisted single-mode fibers, *Appl. Optics*, *18*, 2241.

Wang, P., L. J. Cooper, J. K. Sahu, and W. A. Clarkson (2006a), Efficient single-mode operation of a cladding pumped ytterbium-doped helical-core fiber laser, *Opt. Lett.*, *31*, 226.

Wang, Q., G. Farrell, and Y. Semenova (2006b), Modeling liquid-crystal devices with the three-dimensional full-vector beam propagation method, *J. Opt. Soc. Am. A*, *23*, 2014.

Xie, W., C. Xiong, X. Wang, Z. Wang, and Y. Liu (2008), Single-Mode Parabolic Gain-Guiding Optical Fiber with Core Diameter up to 200um, *Int J Infrared Milli Waves*, *29*, 406.

Yablon, A. D. (2004), Optical and Mechanical Effects of Frozen-in Stresses and Strains in Optical Fibers, *IEEE J. Sel. Top. Quantum Electron.*, *10*, 300.

Yariv, A., and P. Yeh (2003), *Optical Waves in Crystals*, Wiley, NJ, US.